Durham E-Theses

Forced response prediction for industrial gas turbine blades

Moffatt, Stuart

How to cite:

Moffatt, Stuart (2006) *Forced response prediction for industrial gas turbine blades*, Durham theses, Durham University. Available at Durham E-Theses Online: http://etheses.dur.ac.uk/2692/

Use policy

The full-text may be used and/or reproduced, and given to third parties in any format or medium, without prior permission or charge, for personal research or study, educational, or not-for-profit purposes provided that:

- a full bibliographic reference is made to the original source
- a link is made to the metadata record in Durham E-Theses
- the full-text is not changed in any way

The full-text must not be sold in any format or medium without the formal permission of the copyright holders.

Please consult the full Durham E-Theses policy for further details.

Academic Support Office, Durham University, University Office, Old Elvet, Durham DH1 3HP
e-mail: e-theses.admin@dur.ac.uk Tel: +44 0191 334 6107
http://etheses.dur.ac.uk

Forced Response Prediction for Industrial Gas Turbine Blades

Stuart Moffatt

The copyright of this thesis rests with the author or the university to which it was submitted. No quotation from it, or information derived from it may be published without the prior written consent of the author or university, and any information derived from it should be acknowledged.

A Thesis presented for the degree of
Doctor of Philosophy

School of Engineering
University of Durham
Durham, UK
November 2006

12 DEC 2006

Forced Response Prediction for Industrial Gas Turbine Blades

Stuart Moffatt

Abstract

A highly efficient aeromechanical forced response system is developed for predicting resonant forced vibration of turbomachinery blades with the capabilities of fully 3-D non-linear unsteady aerodynamics, 3-D finite element modal analysis and blade root friction modelling.

The complete analysis is performed in the frequency domain using the non-linear harmonic method, giving reliable predictions in a fast turnaround time. A robust CFD-FE mesh interface has been produced to cope with differences in mesh geometries, and high mode shape gradients. A new energy method is presented, offering an alternative to the modal equation, providing forced response solutions using arbitrary mode shape scales. The system is demonstrated with detailed a study of the NASA Rotor 67 aero engine fan rotor. Validation of the forced response system is carried out by comparing predicted resonant responses with test data for a 3-stage transonic Siemens industrial compressor.

Two fully-coupled forced response methods were developed to simultaneously solve the flow and structural equations within the fluid solver. A novel closed-loop resonance tracking scheme was implemented to overcome the resonant frequency shift in the coupled solutions caused by an added mass effect. An investigation into flow-structure coupling effects shows that the decoupled method can accurately predict resonant vibration with a single solution at the blade natural frequency.

Blade root-slot friction damping is predicted using a modal frequency-domain approach by applying linearised contact properties to a finite element model, deriving contact properties from an advanced semi-analytical microslip model. An assessment of Coulomb and microslip approaches shows that only the microslip model is suitable for predicting root friction damping.

Declaration

The work in this thesis is based on research carried out in the Thermo-fluid Dynamics Group, School of Engineering, University of Durham, Durham, UK. No part of this thesis has been submitted elsewhere for any other degree or qualification and it all my own work unless referenced to the contrary in the text.

Copyright © 2006 by Stuart Moffatt.

"The copyright of this thesis rests with the author. No quotation from it should be published in any format, including electronic and the internet, without the author's prior written consent. All information derived from this thesis must be acknowledged accordingly".

Acknowledgements

I would like to thank Prof. Li He for his continual support during the course of this project and for sharing his extensive knowledge. His guidance and contagious enthusiasm for the subject have been greatly appreciated.

The non-linear harmonic method has been developed at Durham University by Prof. Li He, Dr. Wei Ning, Dr. Tie Chen and Dr. Parthasarathy Vasanthakumar under sponsorship from Alstom UK.

I would also like to thank Dr. Haidong Li, Prof. Grant Steven and Dr. Jon Trevelyan from the School of Engineering, Durham University, for their advice and technical support.

This work has been done in close cooperation with Siemens, Lincoln. Many thanks to Mr. Roger Wells, Dr. Wei Ning and Dr. Yansheng Li for their help and support.

This research was sponsored by the European Union Framework V R&D project "Development of Innovative Techniques for Compressor Aeromechanical Design (DIT-CAD)", contract number ENK5-CT-2000-00086.

This document has been produced in LaTeXusing a template created by M. Imran. Many thanks to my brother Iain for the crash course and the (extended) loan of the manuals.

Contents

List of Figures

List of Tables

Chapter 1

Introduction

1.1 Motivation

It is becoming widely accepted that forced response analysis must be integrated into the design phase of all modern turbomachinery blades in aero-engine, industrial and marine applications. Fluid flow through turbomachinery is inherently unsteady, where strong periodic flow disturbances can cause high levels of blade vibration for certain unavoidable resonant conditions. Flow-induced vibration has long been recognised as the primary source of High Cycle Fatigue (HCF) blade failure a problem regularly experienced throughout the gas turbine industry. The scale of the problem is demonstrated by Kielb [1], who highlights that fluid-structure interaction problems continuously arise during the development of each new machine, with every jet engine development program experiencing 2.5 serious HCF problems on average. Fransson [2] mentions that problems which are not discovered during development are responsible for over 25% of all engine distress cases, accounting for almost 30% of total development costs. Putting these costs into perspective, Wisler [3] states that total development costs for an aero-engine can exceed $1 billion, with the development of an aero-derivative engine costing up to $400 million. Additionally, Kielb [4] indicates that HCF-related development and field usage costs incurred by the US military could exceed $2 billion over the 20 years leading up to 2020.

The driving force to eliminate vibration problems is high for all turbomachinery applications. Aero-engines are subject to stringent weight and size limitations and

operate at a wide range of operating conditions, making them highly susceptible to HCF problems – particularly for military jet engines. The process of achieving airworthiness certification requires very vigorous testing, ensuring that most HCF problems are uncovered during the development stage before potential failures can arise in service. However, catastrophic engine failure with loss of life is not unknown in civil and defence aerospace. Industrial and marine turbomachinery is subject to less stringent safety regulations and weight and size limitations, allowing more conservative designs to be adopted. These machines generally operate within a less-demanding operating range, with some exceptions such as industrial pumps, which can operate at off-design conditions for long periods of time. However, no turbomachines are immune to blade vibration problems and the expense of a plant shut-down can be very high, creating losses of up to £1 million per day in the case of the shut down of an electrical power generation plant. Development budgets of industrial turbomachines are normally much smaller than those of aero-engines, and the expense of remedial redesign action following the discovery of a blade vibration problem during testing can significantly increase the total development cost of a new machine.

The occurrence of HCF problems is expected to increase in the future with current trends in modern blade designs. In search of improved efficiency and reduced engine size and weight, commercial pressures are demanding higher blade loading and closer axial spacing, making modern blades more prone to high vibration levels. Conventional design methodologies based on empirical design rules can not confidently predict vibration levels and the assessment of aeromechanical performance is achieved through rigorous engine testing. Analytical prediction methods are generally too costly for routine design use and are currently limited to the larger aero-engine manufacturers. With increasing demands on aeromechanical performance and without an early predictive capability, manufacturers run the risk of moving towards a passive 'repair philosophy', using an iterative method of eliminating HCF problems in new projects by redesigning blades based on engine test results. In order to reduce lead times and development costs of new projects using modern blade designs, there is a great need for a fast and reliable design tool for the prediction of

flow-induced vibration levels. Such capabilities will allow blade designers to assess vibration performance early in the design stage and eliminate potential HCF failures before the first test is performed.

The work presented in this thesis involves the development and assessment of aeromechanical forced response analysis methodologies based on finite element analysis and computational fluid dynamics for the calculation of resonant blade vibration levels. The methodologies are intended for routine design use with the capability of accurately assessing resonant stress levels and predicting blade fatigue life with minimal computational costs.

1.2 Background to the Physical System

1.2.1 Turbomachinery Configurations

A turbomachine is a rotating device for the purpose of either extracting energy from a continuously flowing working fluid (turbine) or applying energy to the fluid (compressor). Energy transfer in a turbine or compressor is made by respectively decreasing or increasing the pressure of the fluid by the dynamic action of moving blades. The common elements of most turbomachines are a) a rotor, containing blades, buckets or an impellor to decelerate or accelerate the flow; b) a shaft to transfer mechanical power to or from the rotor; c) a casing to direct the fluid around rotor; and d) stator blades in the form of inlet guide vanes or downstream blades to control flow swirl around the annulus. Turbomachines are categorised by the orientation of the flow path: axial flow machines employ flow wholly or partially parallel to the axis of the rotor; radial or centrifugal machines involve a flow path mainly normal to the axis of rotation; and mixed flow machines contain significant amounts of radial and axial flow components. Flow can be compressible or incompressible and is not always enclosed within a casing, for example in the case of some fans, wind turbines and tidal turbines.

Gas turbines are a common configuration of turbomachinery, which combine a compressor and a turbine with the addition of heat to the fluid (normally air) in order to generate shaft power or thrust. Incoming air is compressed and fed into a

combustion chamber, where fuel is injected and burned. The resulting combustion gases pass through a turbine to drive the compressor and the remaining high energy exhaust gases are used to provide useful power in the form of thrust or shaft power from a secondary power turbine. Axial turbomachines are most commonly used in aero-engine, industrial and marine gas turbine applications, mainly due to the higher efficiency over their radial counterparts. Axial machines have relatively thin blades and high aerodynamic loads and are more prone to aeroelastic problems than radial machines, which have fairly sturdy impellors. Axial turbomachines usually comprise of several stages in order to achieve the necessary pressure ratios, which can be up to around 20 stages for compressors and 5 stages for turbines, with each stage comprising of one stator and one rotor bladerow. Whilst the analytical methodologies described in this thesis can theoretically be applied to most turbomachinery configurations, the work contained herein focuses on air-breathing axial gas turbines.

1.2.2 Aeroelastic Phenomena

Aeroelasticity is concerned with the static or dynamic interaction between the deformation of an elastic body and behaviour of a surrounding fluid. The study of aeroelasticity is best described by Collar's triangle of forces (Figure 1.1), showing the various levels of interaction between the fluid and structure. The interaction of elastic and inertial forces is involved purely with mechanical vibration without the influence of the surrounding fluid. The interaction between aerodynamic forces and the inertia of a structure represents a rigid body subject to a fluid flow and is typical of the type of problem encountered in aircraft stability and control applications. The interaction of fluid forces with the elastic deformation of a structure neglects structural acceleration and is considered to be a static problem. Static aeroelasticity is experienced by turbomachinery blades, where the steady-state fluid loads of the mean flow result in the static deformation of the blades, varying the aerofoil geometry. Combined with the effects of centrifugal and temperature loading, the static deformation is known as blade untwist and small variations in blade shape can have a significant impact on machine performance. The analysis of sta-

tic blade deformation is very important in turbomachinery design, where the blade must be manufactured to a certain profile, accounting for untwist to ensure that the blade conforms to the correct geometry under normal operating conditions. Dynamic aeroelasticity provides the focus of the work within this thesis and relates to flow-induced vibration problems, combining the effects of aerodynamic, inertial and elastic forces. Dynamic aeroelastic analysis in turbomachinery poses a challenging problem due to the complex interaction between high-speed fluid flow and the dynamic response of the blade structure. Whilst many forms of dynamic aeroelastic behaviour exist throughout a range of engineering sectors, two of the most important dynamic aeroelastic phenomena in turbomachinery applications are forced response and flutter. This thesis primarily deals with the analysis of forced response, but as discussed later, the methodologies can also be applied to flutter prediction.

Forced Response

Aeroelastic forced vibration is caused by periodic flow disturbances passing through the blade passages, resulting in an unsteady pressure field acting on the blade surfaces. The aerodynamic excitation forces are primarily due to circumferential variations in the flow, normally caused by blades passing through the wakes of upstream blades, potential interaction from upstream or downstream blades, non-uniform inlet flow or from fluctuations in the back pressure. Resonant vibration occurs when the frequency of the incoming flow disturbances matches a blade mode natural frequency, which can lead to excessive blade stress amplitudes and eventual HCF failure. The frequency of the flow disturbances in such synchronous excitation is normally proportional to the speed of the rotor, denoted by the engine order (EO), giving the integer number of disturbances experienced during one complete rotor revolution. For example, a bladerow consisting of 32 blades will impart 32 EO wake disturbance on the downstream bladerow, where the downstream rotor will experience an excitation frequency equal to 32 times the frequency of rotation. The inlet distortion of an aero fan subject to a cross wind will result in a 1 EO excitation at the frequency of rotation.

An important tool for visualising when the flow disturbances cause resonant

vibration is the Campbell diagram shown in Figure 1.2. This example maps the frequencies and engine speeds of a large aero fan, showing where resonance is encountered from the individual engine orders. Such resonant conditions are named crossing points, indicating where the frequency of a given EO coincides with a blade natural frequency. It can be seen that the modal frequencies increase with engine speed, which is due to centrifugal stiffening of the blade. Centrifugal stiffening occurs when the blade is deformed out the plane of rotation or in the circumferential direction. For a rotating beam, where the centre of gravity (CG) of each section is radially aligned, the radial centrifugal load will be reacted by a purely radial shear. However, when the blade is deformed and the sections are deflected away from the radial alignment, the blade shear reaction to the centrifugal load will provide a component acting to re-align the section CG's. This restoring force provides a stiffening effect, thus increasing the frequencies of vibratory modes with engine speed.

The Campbell diagram can either be obtained analytically from a finite element analysis (FEA) or experimentally in a rotating engine test using strain gauges placed on the blades. In blade design, the Campbell diagram is used to place natural frequencies either above the maximum engine speed or below the normal operating range with the aim of avoiding continuous resonant excitation during operation. However, crossing points at speeds below the operating range are always encountered during the start-up and shut down of each operational cycle, resulting in resonant vibration contributing to HCF. Since resonance in turbomachines can not be avoided, the vibration levels at all encountered crossing points must be evaluated to determine the risk of fatigue failure during the service life of the machine.

Aeroelastic forced response prediction poses a challenging problem due to the complex interaction between the fluid flow and blade structure. As illustrated in Figure 1.3, blade vibration is caused by incoming flow disturbances creating a periodic pressure distribution over the blade surface. Consequently, the vibration of the blade within the surrounding fluid induces a local unsteady pressure field in the fluid around the blade surfaces. In forced response cases, the motion of the blade through the vibration-induced pressure field results in energy dissipation to the fluid, creating an aerodynamic damping effect. Combined with any mechanical

damping present in the system, the total damping forces limit the amplitude of vibration. Due to the high level of computation required by unsteady computational fluid dynamic flow solvers, routine forced vibration analysis remains prohibitively expensive for most manufacturers. Instead, designers rely on empirical design rules and full-scale engine tests to evaluate vibration performance.

Designers have a number of options to reduce resonant vibration levels in the eventuality that a particular crossing point creates a HCF risk. This can be done either by moving the synchronous vibration frequency, reducing the aerodynamic forcing function or incorporating friction dampers into the blading. Varying the frequency of the crossing point can be done by either modifying the blade natural frequency or by varying the blade count to change the forcing EO. A shift in natural frequency can be achieved by varying the blade shape, changing parameters such as thickness versus span, aspect ratio, taper, solidity and radius ratio. A drastic method of increasing frequencies is the addition of a tip or part-span shroud to stiffen the blades, usually with a secondary friction damping effect. Moving synchronous frequencies outside the operating range is not always possible, particularly for aero-engines, which operate within a wide range of speeds and conditions. An additional point of interest regarding geometry change is that the resulting variation in modeshape may have a significant effect on both the sensitivity of the mode to a particular forcing function and the aerodynamic damping of that mode. This is due to the positioning of the force distribution in relation to areas of high motion of the modeshape.

The strength of the aerodynamic forcing function is strongly influenced by the axial spacing between adjacent bladerows and the strength of upstream wakes can generally be reduced by increasing the axial spacing. However, this action contradicts the aims of modern designs which aim to minimise spacing to reduce engine weight.

Flutter

Unlike forced response where blade excitation is provided by incoming flow disturbances, flutter is a self-excited phenomenon and is not caused by incoming external

disturbances. Flutter occurs, when small levels of blade vibration are amplified by the vibration-induced pressures giving rise to further blade excitation. Flutter analysis can be considered in a similar manner to aerodynamic damping in forced response problems, where the blade motion through the local induced pressure field results in an energy transfer between the fluid and structure. The fundamental difference is that flutter causes the addition of energy to the blade instead of energy dissipation. Flutter can therefore be considered as negative aerodynamic damping. As the self-exciting aerodynamic forces increase with blade motion, flutter can quickly lead to escalating vibration levels causing fatigue failure within a short space of time.

In flutter analysis, blade designers are interested in the flutter stability of the system, determined by the direction of energy transfer between the blade and the fluid. The system is stable when the vibration-induced pressures result in energy dissipation (positive aerodynamic damping) and a decay of vibration amplitude. Flutter instability occurs with energy application to the blade from the fluid, indicated by a negative damping value. It can be argued that a system is stable with small flutter forces, providing that sufficient mechanical damping is present to balance the destabilising fluid work. Under this condition, equilibrium will be achieved and the blade will vibrate with a finite amplitude.

Flutter is predominantly seen in fans, front compressor blades and low pressure turbine blades, and usually occurs above a critical flow velocity or when a high incidence angle causes large flow separation. Since the 1940's when flutter was first encountered in turbomachinery, the most important design parameters safeguarding against flutter have been the reduced frequency and the incidence angle. The reduced frequency is a non-dimensional parameter relating flow velocity with vibration frequency by comparing the period of one vibratory cycle with the time taken for a fluid particle to travel a representative distance (i.e. chord length). The angle of incidence is concerned with the degree of fluid loading on the blade, where flow separation occurs at high values. In practice, the reduced frequency and the incidence angle can only be used as a rough guide to indicate flutter stability since many other critical factors often come into play, for example modeshape, nodal diameter

pattern, and operating conditions such as pressure ratio and flow.

Flutter in turbomachinery applications is categorised into different areas, each showing different characteristics and physical reasoning. The most important flutter regions in a compressor are indicated on the performance map shown in Figure 1.4. This figure also briefly introduces the main physical mechanisms behind stall, supersonic and choke flutter. The details of various flutter are mechanisms beyond the scope of this thesis and more in-depth descriptions are provided by Marshall [5] and Fransson [6]. Ideally, flutter boundaries are placed at locations on the compressor map that can not be reached during normal operation, a technique commonly called "stall protection". Most modern engines have a relatively large stall margin, leaving a sufficient margin to account for engine-to-engine variations, altitude effects, transient operation and engine deterioration.

1.2.3 Vibration Characteristics

In turbomachinery applications, the vibration characteristics of a structure are largely independent of the aerodynamic loads and are generally determined from the mass and stiffness properties of the blade, together with any mechanical damping. This simplification is primarily due to the high density of blades compared to the surrounding fluid, represented by the mass ratio. The mass ratio is defined as the ratio of the mass per unit span of the structure divided by the mass per unit span of a cylinder circumscribing the leading and training edges. Unlike the aeroelastic analysis of aerofoils of lower density such as aircraft wings and helicopter blades, forced response and flutter of turbomachinery blades usually involves the vibration of a single mode, with very little mode interaction and a minimal variation in modeshapes and natural frequencies by aerodynamic loading.

Unshrouded blades

Unshrouded blades, with their slender aerofoils, exhibit similar vibration characteristics to beams and plates, particularly for low-order modes. Beam-type modes give rise to flapwise, edgewise and torsional modes, but without chordwise bending. The blade root can influence aerofoil modeshapes, particularly the constraints at

the root / disk interface which effectively determine the stiffness of the lower part of the blade. Unshrouded blades without under-platform dampers require a rigid disk to avoid mechanical inter-blade coupling between blades, with coupling considered to be only provided by aerodynamic loading. The mechanically independent nature of such blades greatly eases vibration analysis, usually allowing aeroelastic calculations to be performed using a single blade analysis without the influence of structural nonlinearities or disk dynamics.

Disc flexibility

The flexibility of the disk itself can have a significant effect on the overall characteristics of the blades. A relatively rigid disk, such as used in a fan assembly, will provide little influence on the individual blades, which will tend to vibrate in their individual mode shapes. However, a flexible bladed disk assembly will include the characteristics of the individual blades and the disk itself. Disk vibration is characterised by nodal diameter modes, usually consisting of double modes. These modes arise from the circular symmetry, where two consecutive modes possess the same natural frequency with different orientations of modeshape. These modes occur in axial, radial and tangential directions. Disk vibration is characterised by groups of nodal diameters, where each group is associated with a nodal circle. As the mode number and natural frequency increase, the number of nodal circles increases. Without the effect of additional friction dampers, the strong mechanical coupling between the flexible disk and the blades effectively combines the assembly into one structure, combining the natural frequencies of the blades and disk. For a disk-dominated mode, the individual blade will vibrate in a mode with a significant degree of general plane motion.

Shrouded blades

Shrouded blades offer greater rigidity with the mechanical coupling of adjacent blades, resulting in significant disk vibration characteristics. The interlocking shrouds provide a significant degree of friction damping and can be optimised for the desired damping performance. However, the non-linear damping behaviour of friction

damping creates difficulty in the aeroelastic analysis of shrouded blades.

The structural analysis of blade static and dynamic vibrational behaviour is generally finite element based. Cantilevered blades with rigid disks are often modelled individually, neglecting disk dynamics and assuming that all blades are identical. Analysis of flexible disk and shrouded assemblies take advantage of the cyclic symmetry, allowing the structure to be modelled as a segment with cyclic symmetric boundary conditions and reducing computational effort. Other approaches model the entire bladed disk and can include the effects of structural non-linearities and variation in the properties of individual blades, but at the expense of high computational effort. It has also been known to use multi-stage models to capture the mechanically coupling between stages.

Mistuning

A structural characteristic that can have a significant impact on the aeroelastic performance of blades is mistuning. Blade mistuning arises when the cyclic symmetry is broken by small geometric and structural variations in individual blades, resulting from manufacturing processes or wear in service, causing a significant variation in the aeroelastic performance of a system. Flutter stability has been reported to be improved with blade mistuning, backed up by experimental and numerical evidence. However, mistuning generally has a detrimental effect on forced vibration behaviour with the effect of amplifying the vibration levels of certain blades. Whereas a tuned bladed disk assembly will show a single nodal diameter modeshape at a single frequency, a mistuned assembly can simultaneously contain components of several nodal diameters with slight variations in blade modeshapes and natural frequencies. Therefore, the frequency response curve of a mistuned assembly will show a number of resonant peaks around a particular crossing point, increasing the chance of being excited by another excitation order. Hence, amplification in forced response can be caused by secondary resonance from a disturbance of another excitation orders or due to the variation in blade modeshape causing higher sensitivity to aerodynamic forces. Forced vibration amplitudes of mistuned blades can be 100% higher than vibration levels predicted for tuned blades (Ewins [7]). This so-called stress ampli-

fication effect is caused by highly-localised bladed disc modeshapes amplifying the responses of a small number of blades. The sensitivity of bladed disks to mistuning has been found to be dependant on a number of parameters, including the amount of interblade coupling present in the system and the densities in natural frequencies of adjacent mistuned blades.

1.2.4 Unsteady Flow in Turbomachinery

Fluid passing through turbomachinery experiences strong time-dependant disturbances due to the complex nature of high-speed flow and the relative motion of adjacent bladerows. Flow through a blade passage is subject to potential and convective disturbances propagating from upstream sources, potential fields from downstream bladerows and local vibration-induced pressures from the motion of the blades themselves.

Bladerow Interaction

Bladerow interaction between relatively moving bladerows occurs due to the propagation of wakes from upstream blades and the potential interaction between adjacent rows. Due to the high numbers of blades found in turbomachinery bladerows, bladerow interaction normally involves high-frequency excitation of the higher-order modes. In the case of a compressor wake, the wake produced by a blade is primarily a reduction in the flow velocity. Therefore, a downstream blade passing through the wake experiences a sharp perturbation in flow velocity due to the deficit in wake velocity. In the case of a turbine blade wake, the velocity deficit in the wake is seen by the passing blade primarily as a perturbation in the flow velocity but without a significant change in the flow angle. In the past, wakes were determined by experimental measurements, yielding actual wake data or empirical correlations, but modern methods often rely on steady CFD calculations.

Unlike blade wakes, potential disturbances have the capability to propagate upstream and interfere with convective disturbances and potential reflections. Potential interaction involves the propagation of a potential field created by an aerofoil, which can travel both upstream and downstream in axially subsonic flow. Bladerow

interaction can also involve the upstream propagation of shock disturbances, which can cause strong shock excitation of upstream blades. In a transonic stage, a shock can become detached from the blade passages, resulting in a leading edge shock that can propagate upstream to reach the neighbouring bladerow. This type of shock excitation has been known to create problems with the guide vanes of military fans. In addition to leading-edge shock propagation, the trailing edge shocks of high-speed vaneless HP turbine blades have been reported by Kielb [1], to reach the leading edge of the LP turbine blades. The effects of potential and wake interaction are not independent and the presence of the two disturbances can cause interference, either amplifying or cancelling the effects of one-another.

Inlet Distortion

Another major source of blade excitation is inlet distortion, which describes disturbances approaching the first stage due to circumferential non-uniformities in the inlet flow. Inlet distortion is often encountered in aero fans and is seen in first stages of compressors and high-pressure turbines. Unlike bladerow interaction, inlet distortion usually provides a low EO excitation, affecting only the low-order modes intersecting the first few engine orders.

Inlet distortion can be a significant problem for aero fans which often have non-symmetric inlets and can operate with a non-zero angle of attack. Significantly high angles of attack can result from high cross-winds and aircraft manoeuvres, including take-off. Such conditions can cause a large region of flow separation at the inlet, leading to substantial excitation of the fan. Inlet distortion is a particular problem for military jet engines, which can have highly non-symmetric inlets and undertake high agility manoeuvres. Land and marine-based compressors are subject to inlet distortion from the non-uniformity of inlet ducts and the inclusion of struts in the inlet. Gas turbine HP stages are subject to excitation from inlet temperature distortions, provided by the hot streaks exiting the combustor cans. Due to the relatively high number of combustor cans, temperature distortion provides an excitation EO typically between 10 and 20. Inlet distortion can also be experienced by steam turbines under partial flow conditions.

1.2.5 Friction Damping

Background to Friction Modelling

Solid surfaces are inherently rough on a microscopic scale, causing the actual area of contact between two solids to be much smaller than the apparent area of contact. It is described by Bowden and Tabor [8] that "Putting two solids together is rather like turning Switzerland upside down and standing it on Austria - the area of intimate contact will be small". When two macroscopically flat surfaces with microscopic roughness are put in contact under a normal force, the load is transmitted through a number of asperities of varying shape, size and height, as illustrated in Figure 1.5. Local contact pressures are much greater than the average nominal pressure, giving elastic or plastic deformation at the asperity junctions.

When the contact surfaces are subject to a relative tangential displacement, the contact stress in each asperity is further increased until the elastic limit is reached and the plastic flow of the asperity junction occurs. At this point, the asperity is said to reach the transition from stick to slip. The result is a tangential force opposing the motion, which increases with displacement until the yield stress is reached, after which, the force remains constant as the asperity flows plastically. The resulting effect is a tangential force opposing the direction of motion, which increases with displacement up to a maximum value when the asperity reaches the stick-slip transition. Since asperities vary in size, height and loading, each individual asperity reaches plastic yield at different points on the loading cycle. Whereas highly-loaded asperities can each yield with normal loading alone and slip with any given tangential displacement, lightly-loaded asperities withstand a degree of elastic deformation before slip. Under very small tangential displacements, lightly-loaded asperities may not reach yield and will remain stuck. Friction forces are considered to be the combined tangential forces of all individual asperity junctions acting over the entire contact surface, where all asperities are subject to individual loading conditions at various states in the stick-slip transition.

Due to the highly complex geometries of engineering surfaces at microscopic level and the random nature of individual asperity properties, friction models simplify

the underlying asperity mechanics to varying extents. Three friction models are considered in this thesis: two macroslip friction models, which account only for the net effects of two contacting surfaces; and a microslip friction approach, which calculates the net effects based on the contributions of individual asperities.

Friction Damping in Turbomachinery

The sources of damping in turbomachinery blades are from vibration-induced fluid pressures, friction at the blade root attachment, hysteretic material damping or any additional friction dampers. Whilst damping data for root friction and hysteretic damping is scarce, Kielb [9] provides a brief comparison for blades without additional friction dampers. He states that aerodynamic damping usually dominates for the 1st bending, 1st torsion and 2nd torsion modes and that root friction normally dominates for the 2nd and 3rd bending modes, whilst hysteretic damping is negligible. Where additional friction dampers are used, Kielb states that well-designed platform dampers can produce a critical damping ratio above 2%.

Friction damping occurs in regions of relative motion between contacting surfaces in blade attachments or at the contact interface of friction dampers. The most common type of damper is the platform damper, which usually takes the form of a wedge-shaped piece of metal. Platform dampers can either rest against two adjacent blades (blade-blade damper) or be placed between each individual blade and the disk (blade-ground dampers). Blade-blade dampers utilise the relative movement between adjacent blades, causing a sliding motion between the contact points of the damper and each blade. The friction force is strongly dependant on the inter-blade phase angle (IBPA) of the blade movement and causes a degree of mechanical coupling between each blade. Blade-ground dampers are attached to the disk, with frictional forces caused by the blade motion in relation to the disk without interaction between neighbouring blades. Platform dampers are used on most high-pressure turbine blades and some fan, compressor and low pressure turbine blades. Some gas turbine manufacturers make it mandatory to include platform dampers on all high-pressure turbine blades to allow for low-order blade excitation from flow non-uniformities created with the ageing of the machines, such as partial vane burnout.

Other methods of providing friction damping incorporate tip shrouds, part-span shrouds or split-ring dampers. Shrouds normally have the primary intention of increasing the natural frequencies of high aspect ratio blades, such as aero fan blades and LP turbine stages. The nature of the interlocking shrouds can provide useful levels of friction damping and damping performance is becoming an integral part of shroud design. Split-ring dampers in the form of metal rings can be used between blisk stages for the damping of the low nodal diameter nodes.

1.3 Research Objectives

The objective of the project is to develop effective methodologies to integrate the non-linear harmonic aerodynamic method with structural dynamics for blade forced response predictions. The intention of the research is to provide a complete aeromechanical analysis tool capable of providing routine resonant forced response calculations for turbomachinery blade designers under the commercial restraints of solution times and computing resources. Various coupling strategies are to be implemented for the purpose of evaluating the capabilities of decoupled and fully-coupled methods to capture important flow-structure coupling effects. In addition, the effects of friction damping within 'fir tree'-type blade root attachments is to be investigated, with the development of a friction analysis method and a study on the overall sensitivity of the aeroelastic system to friction.

The non-linear harmonic method has been developed by the University of Durham, providing an efficient frequency-domain unsteady flow solution, capable of dealing with significant flow non-linearities. The method has been previously validated for both rotor-stator interaction and oscillating blade cases. Further validation of the fluid solver has been done in parallel with this project by members and industrial partners of the University.

The basic strategy for the blade structural dynamics is to take a standard commercial finite element (FE) package as the baseline analysis method to produce detailed mode shapes and natural frequencies for all the blade vibration modes of interest. The FE package used is Ansys 7.1, a standard code commonly used by

turbomachinery designers. The modal reduction technique will be used to decouple the structural equations, reducing the forced response calculation to a single degree-of-freedom (DoF) for each mode of interest. The forced response calculation for each mode of interest is performed in modal space based on the CFD mesh.

An FE-CFD mesh interface is to be developed for the interpolation of mode shape data onto the CFD mesh. The interface must accurately interpolate mode-shapes from an unstructured FE mesh to a structured CFD mesh and be capable of dealing with a variety of element types and shapes. The interface must prove to be sufficiently robust in order to deal with the complexities of industrial use, such as high modeshape gradients with low density meshes and slight variations in geometry between meshes.

The interaction between fluid and structure will be performed in the frequency domain for compatibility with the flow solver. A separate analysis is conducted for each mode of interest at the operating points given by the respective crossing points of the Campbell diagram. Two distinct coupling philosophies are to be implemented:

- Decoupled approach. Fluid and structure are calculated separately, forming an open-loop system with minimal interaction. Two separate executions of the fluid calculations provide the aerodynamic excitation and damping terms, which are subsequently used to solve the decoupled forced response equation.

- Fully-coupled approach. Fluid and structure are integrated simultaneously within the CFD code, forming a closed loop system with tight coupling between the aerodynamic forces and structural response.

The blade root friction damping analysis is to be carried out using an FE model of the blade and the methodology must be compatible with the frequency-domain aeroelastic calculations to provide friction damping predictions with minimal user effort and computational time. The approach is to linearise the friction contact and allow the highly-efficient modal reduction approach to be exploited. Both Elastic Coulomb friction and microslip friction are to be considered and an evaluation of the sensitivity of damping predictions to the fidelity of contact modelling will be carried out.

The NASA Rotor 67 transonic fan rotor will be used as the primary test case during the development of the methodologies due to the relative simplicity of the case and the availability of published data. This case will be used to demonstrate the application of the forced response systems and provide a basis for further investigations into fluid-structure interaction.

Validation of the forced response system is carried out on the last stage rotor of a Siemens three-stage industrial transonic compressor. Initial verification on the accuracy of the forced vibration predictions will be checked against strain gauge data obtained from full-scale rotating compressor tests, provided by Siemens. This case is to be used for the analysis of root friction damping, where damping predictions will be compared with damping measurements from test data.

1.4 Overview of Thesis

This thesis is divided into eight chapters, including this introductory chapter. The literature review is given in Chapter 2, starting with a fairly comprehensive overview of CFD developments and leading to an overview of structural modelling techniques with an emphasis on FE analysis. A description of FE-CFD coupling methodologies then follows, and the chapter concludes after a review of friction modelling in turbomachinery applications.

Chapter 3 introduces the computational models and methods employed, starting with a summary of the non-linear harmonic method used in the fluid calculations, followed by a overview of the finite element method and a detailed description of the modal method further developed in this thesis. An overview of the current Coulomb and microslip friction models is given with an explanation of how such models can be implemented into the aeroelastic analysis.

Chapter 4 provides a detailed explanation of the decoupled forced response system and the major components, in particular, the FE-CFD mesh interface, and the modal reduction theory used in the aerodynamic forcing, damping and forced response solution. Additionally, a new energy method of forced response solution is presented. A demonstration and validation of the decoupled forced response system

and system components is provided in Chapter 5, using case studies of the NASA Rotor 67 transonic aero fan and a Siemens 3-stage transonic test compressor.

Two fully coupled forced response methods are presented in Chapter 6, based on a frequency-domain and a hybrid frequency-time domain approach, leading to an evaluation against the decoupled method, the implementation of a closed loop resonance tracking scheme and an investigation into the convergence behaviour of the coupled solution. Significant fluid-structure coupling effects were found in the coupled solution due to a fluid added mass effect, which is further investigated in Chapter 7, based on a variation of the decoupled method. An investigation into the sources of resonant frequency shift in both decoupled and fully-coupled methods is performed, leading to a study of sensitivity of a solution to frequency shift. The chapter concludes with an evaluation of the use of decoupled and fully-coupled methods for forced response prediction.

Chapter 8 describes a method for predicting blade root friction damping in the frequency domain based on an advanced microslip friction model, to provide the highest degree of compatibility with the aeroelastic forced response system. Implementation of Coulomb and microslip models into ANSYS are described, and an evaluation of the suitability of such friction models for predicting root friction damping is given. Initial validation of the friction damping predictions is given for the Siemens test compressor.

The thesis concludes with Chapter 9, summarising the conclusions and providing recommendations for future research.

1.5 Figures

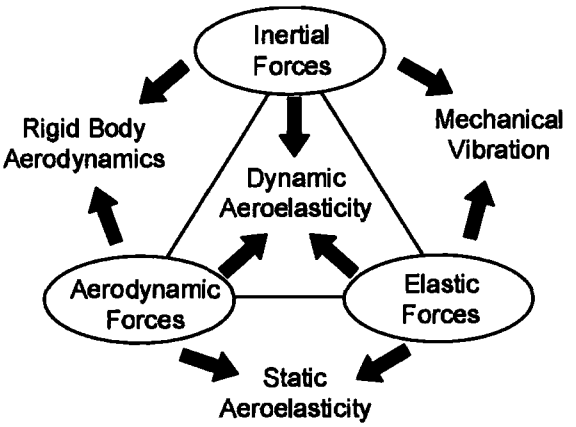

Figure 1.1: Collar's triangle of aeroelastic forces

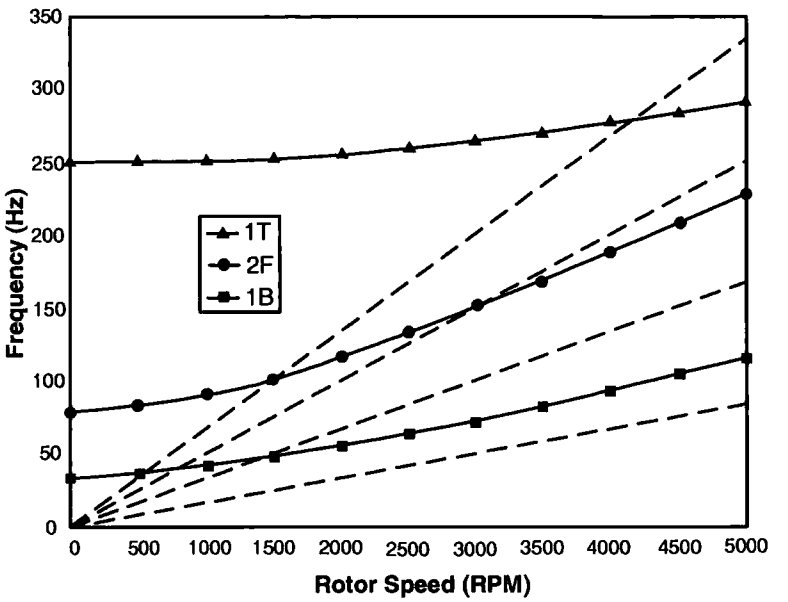

Figure 1.2: Campbell diagram for a typical turbojet fan rotor

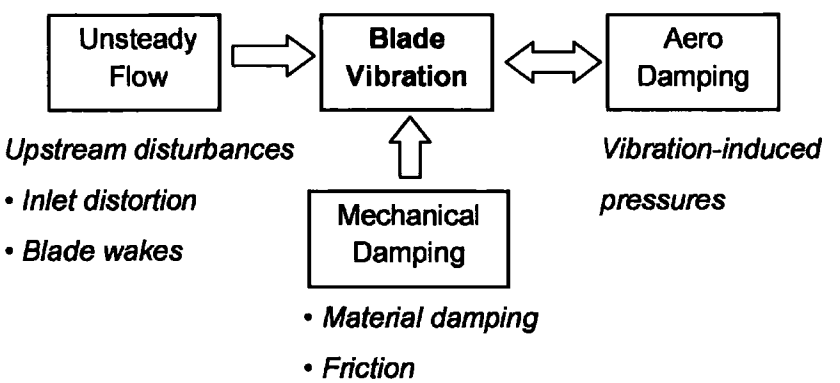

Figure 1.3: Interaction of aerodynamic excitation forces, aerodynamic damping forces and mechanical damping forces with blade vibration

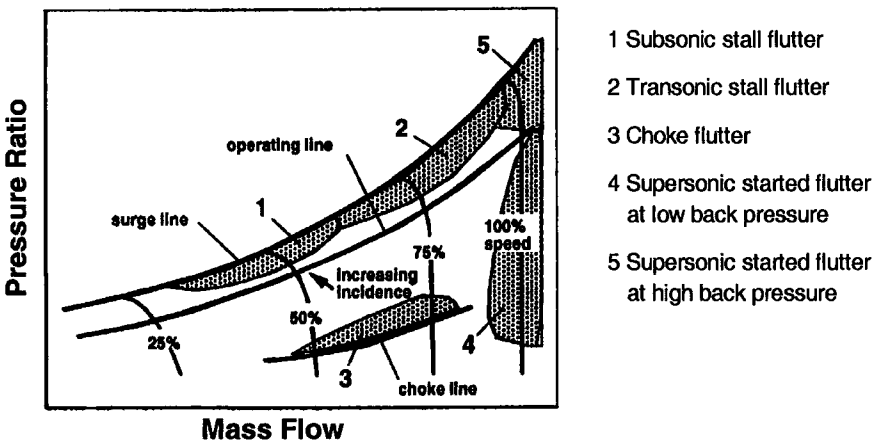

Figure 1.4: Compressor flutter map

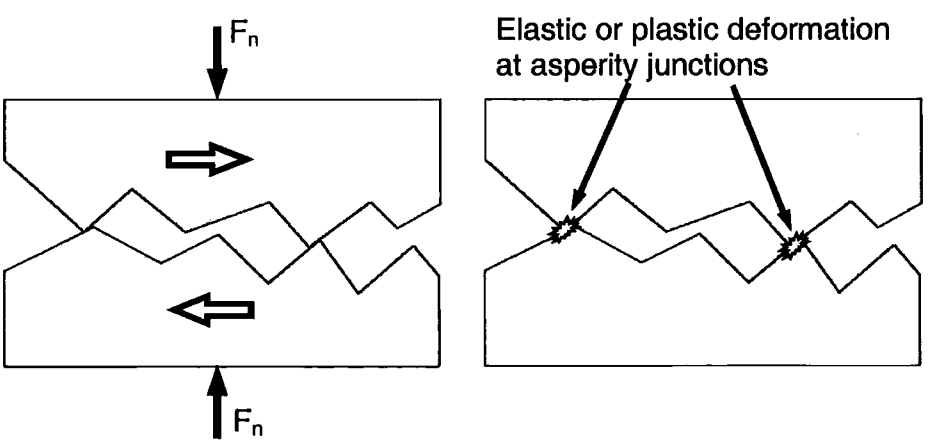

Figure 1.5: Local stress concentrations at asperity junctions

Chapter 2

Literature Review

2.1 Introduction

Aeroelasticity in turbomachinery is a multidisciplinary subject based around structural mechanics and unsteady fluid dynamics, usually involving the integration of finite element analysis (FEA) and advanced CFD methods. Due to the high computational demands of unsteady CFD calculations, the development of aeroelastic methods in recent years has generally progressed with advances in CFD. Much of the research on CFD has been focused on reducing the computational demands of the direct solution of the unsteady flow equations, which is normally prohibitively expensive for multistage turbomachinery applications. Similarly, advances in FEA have resulted in a number of techniques for reducing computational effort using various mathematical approaches and model techniques. For a particular application, the choice of structural modeling technique and the strategy for flow-structure coupling are largely dictated by the type of flow solver used, where methods of coupling have been established for specific types of CFD analysis. Whilst friction modelling has been used for many years in structural analysis, the use of friction models within aeroelastic calculations is starting to emerge, driven by the need to optimise friction damper design. Such friction models involve modelling contact surfaces at microscopic level to varying degrees, which vary significantly from empirical relationships based on experiment to advanced analytical calculations. Integration techniques between friction models and aeroelastic calculations are relatively immature and levels

of integration are subject to large variation.

This chapter starts with a fairly comprehensive overview of developments in unsteady CFD methods, which have had the strongest influence in the progress of turbomachinery flutter and forced response calculations. An outline of significant developments in structural modelling is given, with a particular emphasis on FE analysis and the common approaches for reducing computational effort. An outline of flow-structure coupling methodologies is given, describing the common configurations for integrating FEA with CFD. The chapter concludes with a review of the development of various friction models and implementation into structural and aeroelastic calculations.

2.2 Computational methods for unsteady turbomachinery flows

2.2.1 Governing flow equations

The governing system equations for a CFD model are obtained from the Conservation Laws of fluid flow through a discretised computational domain. These laws can be condensed into a compact form to give the full system of Navier-Stokes equations, providing the general description of fluid flow. The Reynolds-averaged Navier-Stokes equations with turbulence modelling can predict viscous flow in great detail and can include the mechanisms of aerodynamic losses and vortices. However, the high accuracy of the Navier-Stokes equations is at the expense of high computational demands. By making the assumption of inviscid, isentropic flow and neglecting the viscous stress terms in the Navier-Stokes equations, a simplified system of equations is derived – the Euler Equations, which are less computationally demanding. This simplification provides an accurate description of a fluid with highly turbulent flow with high Reynolds number, where the effects of boundary layers can be neglected.

Traditionally, the Navier-Stokes and Euler equations were used to perform the steady flow analysis, which forms the basis of turbomachinery blade design. However, unsteady flow analysis is a more complex problem due to the temporal variation

in the flow field. Both the Navier-Stokes and Euler equations can be applied to unsteady flow where the time-dependent variables are represented discretely either in the time-domain or in the frequency-domain as Fourier coefficients.

2.2.2 Spatial discretisation

Spatial discretisation techniques currently used for CFD analysis largely fall into two categories: finite difference and finite volume. The finite difference scheme is the oldest method used to obtain solutions of differential equations and is the simplest to apply. However, it is not commonly used in turbomachinery analysis, instead being mainly used in external aerodynamics. The finite difference scheme requires an orthogonal mesh with uniform spacing. For analysis of realistic cases, a transformation from the physical mesh to a computational mesh is required. Transformation is difficult for complex geometries, such as that of turbomachinery, but is more straightforward for more common profiles, as used in external aerodynamics, where transformation procedures and corresponding grids are used routinely.

The finite volume scheme, widely used in turbomachinery analysis, involves the discretisation of the fluid domain as a continuum, divided into a finite number of control volumes. The discretised equations are represented in integral form as fluxes through the control volumes, satisfying the conservation laws. This approach allows calculations to be performed in the physical domain and since no transformation is required, the method can be used for complex 3D geometries of any mesh type. Mesh types fall into one of two categories: structured finite difference meshes and unstructured finite volume meshes.

2.2.3 Numerical integration techniques

Time-marching is commonly adopted for high speed compressible flow. The flow equations are integrated in time and solved at each time step using either an explicit or implicit time-marching scheme. The implicit scheme couples every point of the domain simultaneously at each time step. Whilst the solution of a large number of linear simultaneous equations may seem undesirable, this method is unconditionally

stable and can be used for large time-steps. The simplest of these to implement is the explicit scheme, where each point on the mesh is solved in turn at each time step. The simplicity of this method therefore arises due to the lack of simultaneous equations. However, the scheme is only stable for small time step length, requiring large numbers of steps and longer computing times.

2.3 Advances in unsteady aerodynamic methods

Numerous schemes for the solution of the Euler or Navier-Stokes equations have been developed for calculating steady flow through blade passages or unsteady flow due to blade vibration and propagating aerodynamic disturbances from adjacent bladerows or unsteady inlet conditions. Steady flow calculations currently provide the basis for new turbomachinery designs. However, it is now realised that the calculation of unsteady flow is becoming more important to ensure further improvements in aerodynamic performance and structural integrity. A great deal of progress has been made in the use of numerical methods for the calculation of unsteady flows. Unsteady CFD schemes can generally be divided into non-linear time-marching schemes and time-linearised frequency-domain methods.

2.3.1 Time-marching methods

The most popular approach for solving the steady and unsteady non-linear flow equations is the time-marching technique, where the equations are discretised on a computational grid and marched until all transients have decayed to achieve either a steady-state steady solution or a periodic unsteady solution. Computational difficulties arise in time-marching solutions due to large size of system equations, which can be up to the order of 10^6. Additional difficulties arise due to the need for a sufficiently small time-step to capture the important flow disturbances as well as meeting the stability requirements for explicit schemes. Whilst non-linear time-marching provides a powerful insight into complex flow phenomena, it is usually too time-consuming for routine industrial use. Nevertheless, with increases in computing resources, many techniques have been made to maximize accuracy and reduce

computational requirements.

The early explicit MacCormack scheme (MacCormack [10]) dominated practical CFD use until the early 1980's, solving the 2D Euler equations. Jameson [11] developed the popular explicit central difference scheme, a method similar to that of MacCormack which utilised the finite volume discretisation. Several 2D Euler codes have since been developed, such as those used by Fransson and Pandolfi [12]; Gerolymos [13]; and He [14] for the calculation of flows around oscilating blades, and by Giles [15] for bladerow interaction calculations. However, the use of 2D methods have been shown to be inadequate for aeroelastic applications (Namba [16]; Chi [17] and Hall & Lorence [18], where significant 3D effects have been found to be present. The fully-3D calculation of the Euler equations have been reported by Gerolymos [19], Hall and Lorence [18] and Marshall and Giles [20] for the use in flutter and forced response calculations. Inviscid flow calculations are often used in turbomachinery design but are not always suitable for aeroelastic calculations for cases with significant viscous effects, such as flow separation, recirculation and shock-boundary layer interaction can greatly affect blade response. Under these circumstances, a viscous solution is required. The solution of the 3D Navier-Stokes equations has been reported by He and Denton [21] for flow around vibrating blades and Rai [22] and Chen et al. [23] for bladerow interaction problems.

The modelling of unsteady flow with temporal and circumferential periodic disturbances has created computational difficulties as multi passage or whole annulus solutions are often required. The implementation of phase-shifted boundary conditions reduces computational effort by allowing a whole annulus to be represented by a single passage. Erdos [24] was first to implement phase-shifted boundary conditions for the 2D Euler equations by developing the direct store method, which was used by Gerolymos [13] in 2D inviscid flutter calculations. The direct store method requires vast computer storage and is prone to convergence issues. Rai [25] proposed an alternative to periodic boundary conditions by modifying the blade numbers of a rotor-stator turbine stage to allow a directly repeating boundary condition in a small number of passages. The time-inclined method proposed by Giles [15] implemented phase-shifted boundary conditions by transforming the flow equations into

a computational time-domain, but is subject to limitations on the rotor-stator pitch ratio and inter-blade phase angle (IBPA). The Fourier shape correction method of He [26, 27] allows single passage domains to be used with phase-shifted boundary conditions, overcoming problems with storage requirements. However, for complex flow and multi-stage calculations, direct periodicity does not exist and multi-passage or whole annulus domains must be used.

2.3.2 Linearised methods

Compared with the high level of computation associated with non-linear time-accurate solutions, time-linearised methods provide a highly efficient means of unsteady flow calculation. This frequency-domain approach eliminates the need for high temporal resolution and allows a single passage calculation to be performed without the difficulties in implementing phase-shifted boundary conditions, as seen in time-accurate methods. In time-linearised methods, unsteady flow is decomposed into steady and unsteady parts, where linear harmonic flow perturbations are superimposed onto a steady flow solution. Introducing a pseudo-time derivative into the time-linearised Euler ro Navier-Stokes equations, the system can be solved using a range of well-established time-marching schemes to give the steady-state harmonic amplitudes. The harmonic perturbation equation is based on the nonlinear steady solution and is solved in the frequency domain independently of the steady part to yield the harmonic amplitude of the perturbation. The perturbation equation represents a single frequency and a more general solution can be obtained by combining individual solutions at multiple frequencies. However, forced response analysis usually only requires a single flow harmonic at the blade natural frequency of interest, based on the assumption that all frequencies outside the natural frequency have no effect on the steady state vibration amplitude.

Classical linearised methods, such as that of Whitehead [28] were based on tables of flow data of unloaded flat plate cascades, where flow coefficients could be derived for standard geometries for use in analytical flat plate theory. The introduction of computers allowed semi-analytical formulations to be solved, normally with the assumptions of inviscid, irrotational and incompressible flow. Developments of this

type were applied to subsonic flow by Whitehead [29], transonic flow by Namba [30] and supersonic flow by Verdon and McCune [31]. Whilst these methods could have been useful in the aerodynamic design, they are not suitable for practical aerodynamic or aeromechanical analysis. These methods do produce accurate results for the conditions in which they are intended and provide an invaluable benchmark for the validation of modern CFD solvers. An important development of the method is the computer program LINSUB by Whitehead [32], which can calculate several important types of unsteady inviscid flow around a flat plate cascade, such as wake/rotor interaction, potential interaction and blade vibration.

The development of time-linearised potential flow methods, such as those of Whitehead [33] and Verdon and Caspar [34], enabled the analysis of real aerofoils, where the steady flow is based on the solution of the non-linear potential equations. A later development of the potential method by Hall and Verdon [35] includes the effects of incoming vertical and entropic disturbances to allow the calculation of wake-rotor interaction. The need to capture transonic flow details with higher accuracy led to the time-linearised Euler method of Ni [36]. This approach was later developed by Hall and Crawley [37], who solved the linearised unsteady 2D Euler equations using shock fitting giving accurate results, but this proved difficult for complex three-dimensional shocks. Lindquist and Giles [38] showed that shock capturing schemes could accurately model three-dimensional shocks with greater ease. Linearised schemes have subsequently been developed into fully-3D methods by Hall et al. [39] and Marshall and Giles [20].

The efficient linearised Euler methods were very successful but were limited to flow conditions with insignificant viscous effects. Viscous effects can be significant in aeroelastic problems which often occur at off-design conditions, for example at part-speeds, where viscous flows become important. One of the first time-linearised Navier-Stokes solvers was the 2D hybrid viscous-inviscid approach of Cizmas and Hall [40]. Holmes et al. [41] were amongst the first to extend the linearised Navier-Stokes to a fully-3D analysis, but using a turbulence model that limited the scheme to flows with a thin attached boundary layer. Clark and Hall [42] produced a 2D linearised Navier-Stokes solver using a turbulence model capable of dealing with

large flow separations in stall flutter and Sbardalla and Imregun [43] reported a 3D viscous linearised method capable of dealing with off-design conditions. Typically being of two orders of magnitude faster than the equivalent time-domain solutions, time-linearised methods offer a powerful unsteady flow prediction tool for blade designers. However, the non-linear effects are neglected, which can reduce accuracy for cases with features such as shock oscillation and flow separation.

2.3.3 Non-linear harmonic method

Until recently, CFD analysts were limited to the use of expensive non-linear time-marching methods or efficient, but less accurate linearised methods. Whilst linearised methods were developed as an efficient alternative to time-marching schemes, they are limited to linear flow conditions. The non-linear harmonic method relieves this limitation, exploiting the efficiency of the linearised frequency-domain methods, whilst capturing some important non-linear effects of the time-accurate solutions.

Giles [44] devised a linearised Euler method that recognised changes in the non-linear steady flow field due to the linear unsteadiness by introducing quadratic source terms to the steady solution. He [45] adopted the idea of updating the steady solution and proposed the non-linear harmonic method. Instead of using the steady solution as a base, He included the deterministic stress terms, due to the unsteadiness, to produce the time-averaged solution. Unsteady flow is modelled by superimposing the unsteady harmonic perturbations onto the time-averaged flow. The use of pseudo-time-marching allows the use of well-established efficient algorithms to be used. Non-linear interaction between the time-averaged and flow perturbations is included by solving the perturbation equations together with the deterministic stress terms to modify the time-averaged flow. Non-linearity between the individual perturbation harmonics can be included by simultaneously solving the harmonic equations in a strongly coupled manner.

The non-linear capability is further improved by increasing the number of harmonics of the perturbation equation to give a higher-order representation of the flow unsteadiness. A method developed by Hall et al. [46] uses a harmonic balance technique, representing the flow variables by a Fourier series in time with spatially

varying coefficients, in a similar fashion to the Fourier shape correction method of He [26, 27]. The method can be applied to the Euler or Navier-Stokes equations and is shown by Hall et al. to provide reasonable predictions for strongly nonlinear flow. This approach has been adopted by Vasanthakumar [47] and implemented into the non-linear harmonic method to provide a system where both the deterministic stress terms of the time-averaged flow and cross-coupling terms of the individual harmonics are solved simultaneously with flow perturbation equations.

The non-linear harmonic method has been extended to the three-dimensional solution of the Navier-Stokes equations and used for the accurate prediction of flow due to blade vibration (Vasanthakumar et al. [48]) and Stator-Rotor interaction (Chen et al [49]). It has been shown to produce results with comparable accuracy to three-dimensional viscous non-linear time-marching schemes, but with a considerable saving of processing time and storage requirements. Validation of the baseline solver against semi-analytical solutions is given by Vasanthakumar et al. [48] for inviscid flow through unloaded 2-D and 3-D vibrating flat plate cascades and by Chen et al. [49] for wake blade interaction in a uniform steady flow past an unloaded flat blade cascade. Chen et al. also verify the non-linear capability of the non-linear harmonic method for a single stage compressor by comparing the deterministic stresses with those obtained from non-linear time marching in both 2-D and 3-D. Verification on the use of the linear method for bladerow interaction in a subsonic turbine stage and a transonic counter-rotating prop fan is provided by Ning et al. [50], who showed qualitative and quantitative agreement with test data and non-linear time-accurate solutions. The ability of the method to predict bladerow interaction is further verified against test data for a transonic turbine stage by Ning et al. [51].

2.4 Structural Modelling

Much of the earlier work on turbomachinery structural dynamics focussed purely on predicting the natural frequencies of bladed disc assemblies for the intention of designing the machines to operate outside resonant conditions. The early pioneer of

turbomachinery vibration was Campbell [52], who identified the characteristics of vibrational modes of steam turbine bladed discs, and discovered the importance of mistuning, resulting from blade-blade variations in material properties and geometries. The first attempts at modelling the dynamic response of bladed discs involved the analytical solutions of continuous models. Bishop and Johnson [53] used receptance coupling substructure analysis, modelling the blades with Euler beam theory and then coupling them to the disc by combining the frequency responses. Continuous models were also solved by energy conservation principles, using the well-established Rayleigh-Ritz method. Whilst these methods have since been replaced with discrete modelling, they are often used in the validation of numerical schemes.

2.4.1 Finite Element Analysis

The Finite Element (FE) method is a numerical technique for solving a range of physical problems, where the governing equations are represented by algebraic, differential or integral equations. Often being the first choice for detailed structural analysis, finite element analysis (FEA) discretises the distribution of a variable through a complex geometry by dividing the region into small elements of simple geometries. The elements are interconnected mathematically at the nodes, ensuring that the boundary of each element is compatible with its neighbour whilst satisfying the global boundary conditions. The simple geometry of the elements allows the distribution of the variable through the element to be defined by a simple shape function – usually polynomial or trigonometric. The discretisation of the body allows the governing equations for each element to be calculated and assembled into matrix form to give the system equations. The manner in which the element equations are constructed and the physical variables required in the analysis are dependent on the nature of the physical problem, but always involves the specification of nodal coordinates material properties and loading conditions. All physical problems are broken down into a series of matrix equations, where the governing equations of the system take a specific form for the type of problem to be solved.

Finite element analysis, therefore, breaks down a complex problem into a series of coupled equations in matrix form, which are normally solved using general pur-

pose solvers. Due to fact that most structural properties are linear, most dynamic structural calculations are performed in the frequency domain to save computational effort. Any non-linearities such as friction damping can be incorporated into the forcing functions of the right-hand side of the dynamic equations. Frequency domain solutions are usually solved using eigenvalue methods, but other approaches include the harmonic balance method and the state-space method. Problems incorporating high non-linearity or complicated forcing functions can be solved using one of the many time-integration schemes available in commercial solvers. Such time-marching schemes are usually much more time-consuming than frequency-domain approaches. The size of FE matrices can easily reach sizes of 10^6 square, providing a large computational task and a number of methods can be adopted for reducing the computational effort.

2.4.2 Reduced Order Modelling

Various techniques have been adopted in order to reduce computational costs of FEA, particularly for dynamic analyses. There are numerous strategies for improving efficiency, and common techniques approach the problem by either conditioning or reducing the element matrices.

Modal Reduction

Modal reduction provides a convenient method for solving the coupled dynamic equations by expressing the displacements of the masses within a structure as a linear combination of normal system modes. The dynamic response to a harmonic disturbance of arbitrary frequency is considered to be a combination of the contributions of all modes of the structure in the vicinity of the disturbance frequency. Based on the results of a modal analysis, the response of each mode under consideration is calculated individually, to yield the modal amplitudes. During this process, the contribution of each individual mode to the disturbance is calculated separately before being superimposed to give the total system response.

It has been previously discussed that the resonant response of a structure to a harmonic disturbance at a particular natural frequency is characterised by the mode

shape, where the motion of every point on the structure vibrates harmonically and in phase at the excitation frequency, and with a specific relative amplitude. The motion of the structure is therefore 'locked' into that particular mode, where the motion of the entire structure can be defined by a single representative amplitude. Analogous to a single-DoF oscillator, the modal reduction technique calculates the response of each mode in modal space, governed by a series of single DoF modal equations. The modal transformation therefore uncouples the large number of coupled dynamic equations of the FE model to a series of uncoupled second-order differential equations, which are easily solved.

Since modal reduction is a linear approach, it is suitable for systems where the mass and stiffness matrices are constant. The major cost of modal methods is in the calculation of the individual modes, so the method is better suited to cases that can be modelled using a small number of modes.

Lumped Mass

The mass of a standard FE model is consistently defined throughout each element, with the mass distribution defined by the element shape function. This results in a non-diagonal mass matrix, which is difficult to include in the dynamic solution. A common method for obtaining a diagonal mass matrix is to place discrete masses at each node, resulting in a diagonal lumped mass matrix. The mass distribution is discontinuous through the element and each discrete mass is calculated to preserve the total element mass. The lumped mass method used by Ballhaus & Goorjian [141] is the most computationally efficient and has been used for aeroelastic calculations where reduced computational requirements take priority. In addition to the gain in efficiency, it is also recognised that the lumped mass matrix results in higher accuracy for the analysis of thin structures such as blade aerofoils.

Static Condensation

In many circumstances, some degrees of freedom do not significantly contribute to the behaviour of the system and it is not necessary to solve the model using every DoF. The process of static condensation simplifies the problem with the selection

of 'master' and 'slave' DoF to eliminate the unwanted DoF from the solution. For example, the in-plane displacements of a thin aerofoil may be selected as slaves, then condensed out of the system using the technique commonly known as Guyan reduction (Guyan [55]). The resulting order of the mass and stiffness matrices are reduced by the number of slave DoF.

2.4.3 FEA in Turbomachinery

Multistage turbomachines consist of several mechanically-coupled bladed disk assemblies, subject to various effects of disk dynamics, rotor dynamics, inter-stage coupling and bearing effects. Without some sort of model simplification of such large systems, the structural analysis alone would give rise to excessively large FE models for aeromechanical analysis. Early structural analysis was concerned only with predicting the natural frequencies of the blades or bladed disk assemblies to allow blade designers to avoid resonant crossing points on the Campbell diagram. More recent aeromechanical methods involve a similar approach including the calculation of the blade modeshapes, which are usually prescribed onto the CFD mesh based on the assumed modes method.

Tuned Systems

The simplest approach to finite element modelling is to model only one blade within the bladerow, exploiting the cyclic symmetry of the geometry and neglecting the mechanical coupling between blades through the disk structure. A single blade is modelled either as a cantilevered aerofoil constrained at the hub, neglecting mechanical coupling between blades or the disk. This method is appropriate for capturing flow-structure coupling effects in most turbomachinery problems.

For cases with significant inter-blade mechanical coupling, such as for shrouded bladed discs, it is more common to model the structure using cyclic symmetry, reducing the whole bladed disk to a single sector model. Each sector consists of one blade, a portion of disk and any shrouds, which is subject to complex boundary conditions at the periodic boundaries of the sector-sector interfaces. In aeroelastic calculations utilising multi-passage CFD solutions, the cyclic symmetry approach

allows the full assembly modal mass to be derived, which can not be done using a single blade FE model. An additional consideration is that the modes change smoothly between adjacent blades, instead of the step changes would occur between blades if the sector modes were expanded from a single blade.

The tuned approach has been used in decoupled aeroelastic calculations of tuned bladed disks by Chiang and Kielb [56], Manwaring and Kirkeng [57], Green and Marshall [59], Filsinger et al. [60] and Tran et al. [61] and fully-coupled calculations by Gerolymos [62], Marshall [5], Tran et al. [61].

Mistuned Systems

The assumption of cyclic symmetry allows highly detailed FE models of bladed disks to be produced using a single blade sector, but this approach implies that all blades are identical without the effects of mistuning. Mistuning results from blade-blade variations in geometry and material properties caused by manufacturing tolerances and in-service wear. The result typically has a detrimental effect in forced response cases, where vibration is concentrated to a small number of blades, amplifying stress levels beyond those of a tuned system in a phenomenon known as localisation. The direct approach to mistuning would be to run several full whole-bladed-disk FE models with randomly mistuned blades, but this would be too costly in terms of terms of CPU time and storage space. Predicting the effects of mistuning requires computationally efficient methods of performing free-vibration and forces response calculations of full assembly models. Several methods have been developed to reduce the size of large FE models of industrial bladed disk assemblies.

Early methods using lumped parameter models were reported by Ewins [63], Griffin and Hoosac [64], Wei and Pierre [65]. Such models were used in the first investigations of mistuning, when the implications of mistuning were not well-understood and the amplification effect was loosely described in terms of complex modes. The mode localisation behaviour was realised by Wei and Pierre using a singe-DoF model per blade sector based on modal reduction of the spring-mass system. By representing the system as an eigenvalue problem, Wei and Pierre also revealed that sensitivity to mistuning increases with mode density.

The component mode synthesis method of Craig and Bampton [66] reduces the number of DoF of the bladed disk, by considering each blade sector as a separate FE model, represented by a summation of the sector eigenvalues and eigenvectors using modal reduction. Based on the FE solution of a single blade sector, the modes and frequencies of each individual sector component are mistuned, then assembled to allow the complete mistuned assembly to be analysed. Variation between the properties of sectors is usually given randomly and a series of reduced-order solutions can be analysed statistically. Craig-Bampton approaches have been implemented by Irretier [67], Zheng and Wang [68] and Castanier et al. [69]. In a similar manner, Yang and Griffin [70] combine the frequency response functions using receptance techniques. A further development in the use of the component mode synthesis method is by Bladh et al. [71] who investigates the effects of mechanical inter-stage coupling between adjacent bladerows on the sensitivity to mistuning. Moyroud et al. [72] provide a comparison of the Craig-Bamton method and a modal decomposition of a full assembly against an unreduced full FE analysis of for tuned and mistuned cases, including a shrouded transonic fan assembly. Monte-Carlo simulations using statistical methods provide an alternative approach to the modelling of mistuning, as described by Myhre et al. [73]. However, whilst various methods have been developed to attempt to model mistuning, the mechanisms behind mistuning and the implications on blade vibration are not yet fully understood and no reliable prediction method is currently available.

2.5 Aeroelastic Modelling

Dynamic aeroelastic modelling techniques for forced vibration and flutter calculations involve the integration of unsteady aerodynamics with structural dynamics. Various levels of fluid-structure coupling can be employed, depending on the coupling strategy adopted. The type of coupling approach chosen for a particular application is generally determined by the availibility of computing resources, the type of fluid solver used and the need to include fluid or structural non-linearities. At a fundamental level, aeroelastic methods are divided into decoupled and coupled

categories.

Decoupled approaches are based on an open-loop architecture, where the fluid and structure are solved separately with uni-directional transfer of information on a linear basis. Whilst decoupled approaches were originally developed for linearised aerodynamic methods, the method allows a wide range of aerodynamic solutions to be incorporated. The decoupled method is the most common choice for typical turbomachinery cases due to its high computing efficiency.

Fully-coupled schemes are based on closed-loop architecture. The fluid and structure are normally integrated simultaneously in time, exchanging instantaneous forces and displacements at each step in the solution. Modern fully-coupled schemes are usually associated with non-linear time-accurate CFD solvers, which are capable of intrinsically capturing flow and structural non-linearities. However, the computational costs of time-accurate CFD codes are usually too high for routine use, resulting in fully-coupled methods being limited mainly to research and diagnostic applications.

2.5.1 Decoupled Aeroelastic Methods

Decoupled methods treat the fluid and structure in a linearised manner with a minimal degree of interaction between the two domains. The approach is based on the assumptions of linear aerodynamic damping and that blade natural frequencies and mode shapes are not affected by aerodynamic loading. These assumptions are generally valid for turbomachinery blades, which are of high density and stiffness in relation to the surrounding fluid and vibrate with low amplitudes. This unidirectional approach allows the aerodynamic calculations to be performed independently to the blade dynamics, offering considerable savings in computing requirements. It is commonly accepted that mode shapes effectively remain unchanged for lightly damped turbomachinery blades, and this assumption has been widely adopted i.e. Kielb [9]; Marshall and Imregun [5]). Linear damping has been observed for transonic fan rotors by Li and He [74] and Schmitt et al. [75].

In a decoupled aeroelastic analysis, blade structural dynamics are firstly obtained with a free vibration calculation to provide the blade modeshapes and natural fre-

quencies. The analysis is then done for a single mode at the corresponding natural frequency. Traditionally, the decoupled method has been used for flutter prediction and has been extended to forced response calculations in more recent years. Flutter calculations are concerned with determining the aeroelastic stability of the system, indicated by the direction of energy flow resulting from the blade vibrating in the fluid. A decoupled flutter prediction therefore involves calculating the vibration-induced pressures due to blade motion in the specified mode shape. In a forced response analysis, the aerodynamic analysis involves the calculation of aerodynamic damping for the given mode, in a similar manner to a flutter calculation; and the calculation to the aerodynamic forcing terms, providing blade excitation from the incoming flow disturbances.

Flutter

The flutter phenomenon has been experienced since the advent of the earliest aircraft soon after the turn of the 20^{th} century, leading to the first aeroelastic prediction methods. Some of the first flutter calculations of isolated aerofoils were performed by Theodorsen and Garrick [76], who modelled the bending and torsion of an aerofoil section in incompressible potential flow; and by Goland [77], who applied a known aerodynamic load to the differential equation solution of a uniform cantilever beam. An important early development in turbomachinery aeroelastic analysis was by Lane [78], who provided the general solution for a tuned cascade and showed that a linear system of identical blades can be represented by a single equivalent blade, where the vibration of all blades are assumed to occur with the same amplitude and with a fixed interblade phase angle.

A significant advance in the prediction of flutter boundaries was the Energy Method proposed by Carta [79], which calculates the net energy transfer between a vibrating body and the flow-induced pressures of the surrounding fluid. Based on the isolated flat plate theory of Theodorsen [80], Carta evaluated the logarithmic decrement of a shrouded bladed disc as the ratio of work done by fluid pressures to the average kinetic energy of the system. The energy method is based on the assumption that the flutter occurs in a single natural mode of vibration, neglecting

the effect of mode modification by aerodynamic forces. The energy method was further developed by Mikolajczak et al. [81], who generalised Carta's method to include mechanical damping and drag force based on flat plate cascade theories.

The assumed modes approach provides the basis of all decoupled aeroelastic methods for flutter and forced response calculations. The eigensolution approach provides a very flexible method of combining a variety of aerodynamic methods with structural dynamics using an assumed mode approach, where the simplified structural representation in the frequency domain allows significant savings in solution times. The aerodynamic forces can be obtained from almost any source, either directly frequency domain or transformed from the time-domain into the frequency domain by means of Fourier analysis. The eigensolution method was introduced into turbomachinery applications by Bendiksen and Friedmann [82] who combined Theosdorsen's model with Lane's assumption to predict the effect of bending and torsion on the flutter stability of a tuned cascade. Kaza and Kielb [83] developed the method to predict mistuned cascade flutter, and Kielb and Ramsey [84] went on to model supersonic fan flutter using flat plate cascade theory.

The solution of the 2-D potential equations in decoupled flutter analysis has been done by Verdon and Caspar [85], Whitehead [86] and Hall [87]. The solution of the Euler equations has been done in 2-D by Takahara et al. [88], and Hall and Crawley [37]; and in 3-D by Hall and Lorence [18]. The solution of the Navier-Stokes equations in decoupled flutter calculations has been reported for 2D calculations by Giles and Haimes [89]; and for 3D calculations by Siden [90], He and Denton [21], Clark and Hall [92], and Chassaing and Gerolymos [93].

Forced Response

The main difference between a forced response analysis and a flutter analysis is the inclusion of the incoming flow disturbances providing blade forced vibration and the calculation of resulting blade response. Whereas a flutter analysis is concerned with the direction of energy flow between a vibrating blade and the induced fluid forces, a forced response analysis involves the calculation of: a) incoming flow disturbances; b) aerodynamic damping; and c) blade modal response. The decoupled approach

allows the aerodynamic excitation and damping loads to be derived independently from a wide range of sources, such as from flow measurements, empirical models or CFD calculations.

Early forced response calculations of flat plate cascades were based on the *frozen gust* assumption of Whitehead [29], where a vortical inlet disturbance is assumed to be convected downstream without being distorted by the flow field. An extension to this approach by Goldstein and Atassi [94] introduced a degree of wake distortion for an isolated aerofoil in incompressible flow. Aerodynamic damping calculations using similar flat plate cascade theory were given for subsonic flow by Whitehead [28], transonic flow by Namba [30], and supersonic flow by Verdon and McCune [31]. The use of measured wake data to determine incoming flow disturbances is described by Manwaring and Fleeter [95] who carried out extensive experimental studies of unsteady loading of compressor blades under distortions, wakes and potential fields. Examples of empirical modes include Mugridge and Morfey [96] and Raj and Lakshminarayana [97].

Modern decoupled forced response methods are based around CFD calculations, usually solving the linearised 3-D Euler equations (Giles [44]; Hall et al. [39]). An early example is by Chiang and Kielb [56], who produced a forced response system combining both semi-empirical and analytical fluid calculations in order to minimise computing costs of the CFD calculations. The incoming inlet flow disturbances providing blade excitation were modelled using a semi-empirical rotor wake-vortex model, measured data from the inlet distortion and a quasi-3D Euler solver for the pressure disturbances. This work demonstrated both the flexibility of the decoupled forced response method and the ability to efficiently predict vibration levels on a routine basis.

The use of linearised CFD calculations of both aerodynamic damping and forcing terms is described by Kielb [98], who presents a resonant forced vibration analysis of an aeroengine fan rotor under inlet distortion subject to aerodynamic and structural damping. Manwaring and Kirkeng [57] describe the forced response of a low pressure turbine blade due to circumferential pressure distortion involving the 3-D solution of the linearised Euler equations. Campobasso and Giles [99] describe an extension

of the decoupled method to the analysis of mistuned systems, where the decoupling of aerodynamic loads allows a detailed investigation on mistuning effects.

The use of non-linear time-marching CFD schemes is less popular with the decoupled method and a flexible interfacing technique has been reported by Moyroud et al. [100]. Additionally, Schmitt et al. [75] use a variation of the decoupled approach based on the the superposition of aerodynamic forces to evaluate the use of both decoupled and fully-coupled forced response methodologies. Rather than the traditional consideration of aerodynamic damping as an equivalent viscous damping ratio, Schmitt et al. directly apply the vibration-induced pressures to the modal equation.

The decoupled method is particularly suited for resonance tracking schemes, where a number of forced response calculations are needed to capture large shifts in resonant frequency due to friction dampers. Green and Marshall [59] present a method of modelling a rotor acceleration of a high pressure turbine blade with under-platform dampers. Aerodynamic forcing and damping terms obtained from a linearised 3-D Euler solver are interpolated and scaled over the frequency range, before being passed to a non-linear transient dynamics solver. In a similar manner, Bréard et al. [101], describe a decoupled frequency sweep with friction damping using a 3-D viscous time-marching scheme, neglecting aerodynamic damping.

2.5.2 Fully Coupled Aeroelastic Methods

Whilst aeroelastic behaviour remains fairly linear under many operating conditions, the need to model more complex flow-structure coupling effects with significant non-linerities has lead to the development of fully coupled methods. With the rise in popularity of time-marching CFD schemes in the 1980's, fluid-structure coupling methodologies soon emerged that solved the fluid and structural equations simultaneously, usually in the time domain. In fully-coupled approaches, the level of interaction between the fluid and structural domains can vary from partially integrated schemes to fully integrated schemes. Partially integrated schemes solve the fluid and structural domains separately, exchanging information at each step in the solution. Inter-grid interpolation is required at each step and one of several

interfacing schemes can be used to transfer data between the fluid and structural meshes (i.e. Steger and Benek [104]; Rai [105]; and Moyroud [100]). Fully integrated methods combine the fluid and structural equations into a single numerical integration scheme, solving the entire system without the need to transfer information between meshes at each step. Whilst fully-coupled methods involve a greater degree of computation, they allow the inclusion of most nonlinear effects, with the capability of providing less conservative flutter stability boundaries where limit cycle behaviour is experienced. A second benefit of the fully-coupled method is that the inter-blade phase angle providing the greatest instability automatically comes out of the solution, rather than being an input requirement to the decoupled solution.

Flutter

The partially-integrated flutter method, developed by Ballhaus and Goorjian [141], involves the simultaneous solution of the fluid and structure, each of which are considered separately. Structural dynamics are usually based on the free-vibration modal properties of the structure, which can be obtained numerically from a finite element or analytical model, or from experiment. The modal representation greatly reduces computational effort by reducing the structural equations to a small number of orthogonal modal equations which can be integrated in time. Alternatively, a full finite element model can be integrated in time in parallel with the CFD solver, where the fluid pressure distribution at each time step is fed back to the FE package. A wide variety of aerodynamic models can therefore be incorporated with little restriction on the choice of fluid solver used.

Early investigations of stall flutter in linear cascades were done by Sisto et al. [106] and Abdel-Rahim et al. [107] based on a 2D vortex and boundary layer method for incompressible flow. Each 2D blade section was represented by a 2 DoF spring model, solving the bending and torsion equations of motion. Bakhle et al. [108] utilised a similar rigid blade structural model, coupled with a 3D nonlinear potential flow model. He [109] performed flutter and rotating stall calculations on a cascade in two structural degrees of freedom using a 2D Navier-Stokes solver. A number of more sophisticated methods based on 3D Euler and Navier-Stokes solvers,

integrated with FE models have been developed by Vahdati and Imregun [110], Marshall [5], Chew et al. [111] and Hwang and Fang [112].

Fully integrated methods consider both the fluid and structure as a single continuum, where the fluid and structural equations are discretised such that they can be integrated in time using a single numerical scheme. The method was pioneered for flutter by Bendiksen [113], who integrated the Lagrangian-Eulerian formulation of the aeroelastic equations in time using a 5-stage Runge-Kutta time-marching scheme. The simultaneous solution of the flow and structural equations eliminates any possible time lag in the coupling between the two domains, and is claimed to predict energy transfer with greater accuracy than partially integrated schemes.

The disadvantage of fully coupled methods is the high computing costs associated with integrating the fluid and structure. One method of reducing computational demands is to implement a hybrid approach, such as the method of Gerolymos [19]. In this approach, the time-domain solution of the 3D Euler equations is coupled with the frequency-domain modal solution of the structural dynamics. Based on a free vibration modal analysis, the motion of a blade mode shape and a given inter-blade phase angle is prescribed onto the CFD mesh and the aerodynamic solution is marched for one period. After each period, the blade mode shape is recalculated based on the aerodynamic coefficients and the cycle is repeated until convergence of the blade mode in the frequency domain is achieved. This method improves the computing efficiency over fully coupled methods whilst maintaining the ability to model the nonlinear effect of aerodynamic forces on mode shape.

Forced Response

The development of fully coupled forced response methods has occurred only fairly recently with advances in computing power. Providing the most realistic simulation of fluid-structure coupling effects, fully coupled schemes normally involve the time-accurate representation of the viscous compressible flow. Fully-coupled forced response analyses usually involve the linear modal solution of the blade dynamics for the purpose of reducing computation. Sayama et al. [114] solve the Favre-averaged unsteady Navier-Stokes equations by means of non-linear time-marching, where the

fluid mesh is deformed at each step according to the structural motion such that changes in aerodynamic damping and flow unsteadiness are accommodated. Based on a linear modal analysis, structural non-linearities, such as friction dampers are included through an iterative modal solution. The application of the scheme for inlet distortion and bladerow interaction cases for compressor fans and turbine stages with the inclusion of friction damping are described by Vahdati et al. [115] and Bréard et al. [101]. In addition, a similar approach based on linear structural dynamics is applied to a counter-rotating prop fan by Schmitt et al. [75] for the purpose of evaluating decoupled methodologies.

2.6 Blade Root Friction Modelling

Friction is defined as the tangential force opposing the relative motion of two surfaces in contact that are subject to a normal pressure. Frictional forces are often very difficult to calculate accurately as they depend on many physical properties of the surface topography, materials, loading conditions and the presence of any contaminants. The evolution of friction models over the last century has yielded a variety of approaches that can be placed into two categories: macroslip and microslip. Macroslip models offer the most simple approach, based on the classical Coulomb friction theory and assuming rigid motion of a body over a contact surface. Microslip models offer greater fidelity for conditions with small displacements and high pressures, by incorporating the effects of local deformation of the contact surfaces on a microscopic scale.

2.6.1 Macroslip Models

The most common understanding of friction is Coulomb friction, developed by Amontons and Coulomb during the late 17th and 18th centuries, respectively. Coulomb friction corresponds to dry, unlubricated surfaces, and states that the whole friction surface is either stuck or sliding. The frictional force is determined by either a static or dynamic coefficient of friction, relating to the ratio of the tangential frictional

force to the normal force, ie,

$$\mu = \frac{F_t}{F_n}. \tag{2.1}$$

The static coefficient of friction relates to the maximum tangential force the contact interface can withstand without relative motion, whilst the dynamic friction coefficient corresponds to the tangential load sustained during relative motion (sliding). In practice, the static friction coefficient is higher than the dynamic coefficient due to adhesion (chemical bonding) between the surfaces, which can be particularly high for clean surfaces of similar chemical composition. A characteristic of the Coulomb friction model is that it does not allow sliding to take place until the critical tangential force is reached, after which point the frictional force remains constant. In terms of displacement, the frictional force is of constant amplitude and opposes the motion for any sliding displacement. One of the earlier studies of dynamic systems with Coulomb friction was by den Hartog [116], who obtained the exact steady-state response of a SDOF system, where friction damping was calculated based on a piecewise linear hysteresis curve.

An extension to this approach is to incorporate a degree of flexibility in the contact surface before slip takes place, to form an elastic Coulomb model, commonly known as macroslip. Macroslip assumes the bulk material around the surfaces remain rigid when subject to a tangential load, but allows a degree of elastic motion of the contact surface before the critical tangential force is reached and sliding takes place. Such an approach was implemented by Caughey [117], and Menq and Griffin [118], who added a series damper stiffness to a Coulomb under-platform friction element to provide a system with a bilinear hysterestis curve. The application of the macroslip model to a bladed disc assembly was reported by Muszynska and Jones [119]. Further development of the macroslip model has been done by Menq et al. [120], who investigated the effect of varying the normal force on friction damping behaviour.

The popularity of the Coulomb macroslip model is due to the simplicity of the method, which is easy to implement and requires only a small amount of empirical contact data. The approach is fairly robust and it has been shown by Griffin [121] that predictions made by the macroslip approach correlate reasonably well with

experimental data. However, the rigid approximation of the macroslip model is not valid under conditions of high normal contact pressure or very small amplitudes of vibration. Under such conditions, the Coulomb approach predicts sticking behaviour with no sliding, resulting in purely elastic tangential motion of the contact surfaces. In reality, small regions of localised slip occur at low displacements whilst the rest of the surface remains stuck, hence a degree of hysteretic friction damping is always encountered. In these cases, a microslip model is required to predict the contact behaviour before gross sliding occurs where macroslip models predict lock-up.

2.6.2 Microslip Models

Microslip models consider the contact surfaces at a microscopic level, where the influence of surface roughness plays a crucial role. Surfaces of apparently flat surfaces are represented by a series of asperities of varying geometry. Under a given normal pressure, a proportion of the asperities will be in contact, resulting in local contact pressures that are much higher than the nominal pressure. Highly loaded asperities are either close to or at the plastic yield stress, where further tangential loading results in plasic flow, or sliding, immediately. Lightly loaded asperities require higher tangential loading to reach the yield stress, where plastic flow occurs with higher deformation. Due to the variation in asperity geometry, the load carried by each asperity varies and, hence the stick-slip transition occurs at a range of conditions. The global effect results in a smooth hysteresis curve, which is representative of hysteresis curves measured experimentally for small amplitude and high-pressure cases.

Analytical microslip friction models have been developed since the late 1940's, with early methods produced by Mindilin [122] and Courtney-Pratt and Eisner [123]. Courtney-Pratt and Eisner explained microslip in terms of elastic and plastic deformation, where high local stresses are encountered from normal loading and friction is provided by plastic flow at contact asperity junctions. Multi-asperity contact models were pioneered by Greenwood and Williamson [124], who considered asperities as being spherical near the summits with constant tip radius and random height distribution. Further work of Greenwood and Tripp [125], showed that the

contact of two surfaces can be represented by a single rough body on a smooth surface, thus allowing the simplification of mathematical models. An alternative approach to microslip was developed by Burdekin et al. [126], who developed an elastic analysis based on prismatic rods of equal stiffness and linear height distribution, analogous to brush bristles. Chang et al. [127], devised an elastic-plastic asperity model for normal loading based on volume conservation, in a similar manner to Greenwood and Williamson, but with the conservation of a control volume of plastically-deformed asperities. Chang et al. [128], also developed a method of calculating the static coefficient of friction, assuming no additional tangential load can be carried once asperities reach von Mises yield criterion and plastic flow occurs. A theoretical study of microslip based on the random modelling of asperity height distribution and asperity deformation was developed by Björklund, [129].

A very useful publication of an analytical microslip model is by Olofsson [130], who extended the spherical asperity model of Hagman [131], to include cyclic displacement under constant normal load. The model is shown to agree well with experimental results. The model was subsequently adapted to model the friction of ansiotropic materials using ellipsoidal asperities to allow for changes in surface properties in different orientations, which typically occur in machined materials (Hagman and Olofsson [132].

In recent years, two-dimensional microslip models for planar oscillating motion have emerged. Sanliturk and Ewins [133], developed 2D models for both macroslip and microslip, based on the work of Menq et al. [134]. The advanced friction modelling techniques of Petrov and Ewins [135] are now capable of dealing with arbitrary variation of normal loads, variation in surface properties and multi-harmonic planar motion.

2.6.3 Application of Friction Models in Turbomachinery

Friction models are difficult to solve analytically due to the highly non-linear nature of friction contact, with the main difficulty caused by the transition from stick to slip. An early analytical method produced by den Hartog [116] is based on the piecewise linear behaviour of a rigid Coulomb friction model to obtain the analytical solution

for steady-state vibration. However, such analytical models become impractical for complex problems and have difficulty in predicting resonant responses. Forced response calculations incorporating friction are, therefore, usually solved by numerical methods in the time or frequency domain.

The numerical integration of friction models in the time domain provides a simple, robust approach, where solutions are usually obtained using standard finite difference schemes. The major benefit of this approach is that it overcomes the difficulty of dealing with the transition from stick to slip in the macroslip model, where the state of the system is determined at every step in time. Additional sources of nonlinearity that are readily incorporated into time-integration schemes are multi-harmonic motion, and time-dependent variation in contact properties and normal loading (i.e. Petrov and Ewins [135]). The greatest disadvantage of time integration is the length in computing time required to reach steady-state solutions after initial transients have decayed. This is particularly significant for lightly-damped structures, such as turbomachinery blades. It is therefore more common to solve friction models in the frequency domain.

The most popular frequency domain approach is the Harmonic Balance Method (HBM), where harmonic friction forces are assumed to result from harmonic motion. The friction forces for any given amplitude of vibration are obtained through time-marching to yield the nonlinear force over one period of oscillation. The force is then linearised by taking the Fourier transform to give only the first harmonic amplitudes, assuming that the structural response filters out higher order harmonics. The fundamental terms in the Fourier series represent the in-phase and out-phase forcing components, where the in-phase component effectively represents a spring stiffness and the out-phase component represents an equivalent viscous damping term. The fundamental Fourier components are often combined in the form of a complex stiffness, where the real and imaginary components represent the stiffness and damping terms respectively. The fundamental harmonic representation has been shown to be valid for a wide range of cases in several studies, for example Menq and Griffin [118], Csaba [136], and . As discussed by Griffin [137], special cases where the single harmonic assumption becomes invalid are when the the friction

interface is stuck for large parts of the cycle or if there is a natural frequency at an integer multiple of the excitation frequency. The linearised force corresponds to a single amplitude of vibration, which can be applied to the structural model in its linearised form. The forced response of the structure is then calculated and the friction calculation is repeated at the new amplitude to yield the updated friction force. The process is repeated until convergence is reached between the structural and friction models.

An alternative frequency-domain approach to the HBM is Lazan's Method, or the Equivalent Energy Balance Method. Lazan's method is used in the same manner as the HBM, with the only difference being in the calculation of the equivalent linearised hysteresis loop. Also being elliptical in shape, the loop is calculated to satisfy two conditions: 1) the area of the ellipse is equal to the area of enclosed within the nonlinear hysteresis curve, ensuring consistant energy dissipation; and 2) the peak amplitude of both curves are equal. A study by Csaba [136] shows close agreement between the two linearised approaches.

In turbomachinery applications, research into friction modelling has focused on applications where friction is intentionally included, such as under-platform dampers and blade shrouds, rather than blade root friction itself, which is not intentionally designed into blades. In blade design, friction damping analysis is usually performed for the optimisation of friction dampers. With the requirement for fast solutions within optimiser codes, the integration of various friction models with finite element models is usually performed in the frequency domain, employing the HBM with the modal superposition technique. Examples of friction damper optimisation techniques are given by Csaba [138], Sanliturk et al. [139], and Panning et al. [140].

2.7 Current State-of-Art

Many advanced time-accurate CFD methods are currently available solving the 3D unsteady Euler or Navier-Stokes equations, providing reliable means of predicting highly complex flows through turbomachinery blade passages. However, the high computing demands of such schemes means that time-accurate flow solvers are gen-

erally too expensive for routine aeromechanical analysis and are usually used for research and diagnostic purposes. Linearised frequency domain approaches offer a highly efficient solution of 3D viscous and inviscid unsteady flow for cases without strong non-linearities, providing a popular basis for forced response and flutter calculations. Non-linear frequency domain solvers, such as the nonlinear harmonic method, exploit the efficiency of linearised methods, whilst retaining the ability to include significant non-linear effects.

Fully-integrated flutter and forced response methods involve the simultaneous solution of the fluid and structural domains in the time-domain and are usually associated with non-linear time-marching fluid solvers. The structural response is often solved in modal space, but the fully integrated solution of a full finite element model is quite common, particulary when structural non-linearities are included. Decoupled methods are the most common choice for routine forced response and flutter analysis due to their high efficiency. Decoupled methods can be used with any unsteady flow solution, but are normally used with time-linearised flow solvers for reasons of efficiency. Decoupled methods are particularly suited to the majority of aeromechanical analysis cases which do not show significant non-linear flow-structure coupling effects.

Blade friction analysis in turbomachinery applications have focused on blade damper components for the purposes of optimising damper designs, rather than predicting root damping at the blade-disk interface. The development of friction methods has provided advanced generic contact models capable of predicting microslip, multi-directional and multi-harmonic friction forces. In turbomachinery, recent research has applied various advanced contact models to complex damper geometries and blade finite element models. In terms of aeromechanical analysis, optimisation techniques have incorporated less advanced friction mechanics to simplified blade models, subject to decoupled aerodynamic modal forces to evaluate damper designs. The application of advanced friction models in turbomachinery flutter and forced response analysis is currently immature.

Chapter 3

Computational Models and Methods

3.1 Non-linear Harmonic Method

3.1.1 Description

The nonlinear harmonic method aims to exploit the CPU efficiency of time-linearised frequency-domain approaches, whilst retaining the ability to capture significant non-linear effects. Solving the fully 3D Navier-Stokes equations, the unsteady flow field is modelled by superimposing unsteady harmonic perturbations onto time-averaged variables. The system is solved in the frequency-domain using a pseudo-time marching scheme, therefore eliminating the need for temporal resolution, increasing efficiency over time-accurate methods. The use of phase-shifted boundary conditions allows each bladerow to be modelled using a single-passage domain, further reducing the computational effort. The rotor-stator interface treatment follows a flux-averaged characteristic-based mixing plane approach, resulting in the continuous passing of all flow parameters across the interface. Spatial discretisation is performed using a cell-centred finite volume approach and blade deformation is facilitated by a spring-analogous deforming mesh [48].

The deformation of each point within the CFD mesh is specified using a two-stage process based on the modal analysis of an FE structural mesh. The first stage is

described in detail later in Chapter 4 and involves interpolating the modal displacements from the surface of the FE mesh to the blade surface boundaries of the CFD mesh. Whereas the upper and lower surfaces of the FE mesh correspond to adjacent blade passages, the surface displacements of the upper and lower blade boundaries of the single-passage CFD mesh are specified based on the periodic boundary condition defined later by Equation 3.2. The modal displacements are subsequently scaled to provide the displacement amplitudes of the CFD mesh surface nodes about a steady mean position for the single harmonic in question. The second stage involves the distribution of the displacement amplitudes throughout the CFD mesh. With the mesh boundaries at inlet, outlet, hub and casing constrained to having zero displacement, the CFD nodal displacements are distributed throughout the mesh using a spring analogy.

The governing flow equations are the fully 3D Reynolds-averaged Navier-Stokes equations applied to a cylindrical coordinate system (x, θ, r) in an absolute frame of reference. Over a moving finite volume, ΔV, the full unsteady flow equation in integral form is given by

$$\frac{\partial}{\partial t}\int\int\int_{\Delta V}\mathbf{U}\,dV + \oiint_{A}\left[\left(\mathbf{F}-\mathbf{F}_V\right)\vec{n}_x + \left(\mathbf{G}-\mathbf{G}_V\right)\vec{n}_\theta + \left(\mathbf{H}-\mathbf{H}_V\right)\vec{n}_r\right]d\vec{A} = \int\int\int_{\Delta V}\mathbf{S}dV \quad (3.1)$$

where

$$\mathbf{U} = \begin{pmatrix} \rho \\ \rho u \\ \rho v r \\ \rho w \\ \rho e \end{pmatrix}, \quad \mathbf{F} = \begin{pmatrix} \rho u - \rho u_g \\ \rho u u + p - \rho u u_g \\ r\left(\rho u v - \rho v u_g\right) \\ \rho u w - \rho w u_g \\ \left(\rho e + p\right)u - \rho e u_g \end{pmatrix}$$

$$\mathbf{G} = \begin{pmatrix} \rho v - \rho v_g \\ \rho u v + p - \rho u v_g \\ r\left(\rho v v - \rho v v_g\right) \\ \rho v w - \rho w v_g \\ \left(\rho e + p\right)v - \rho e v_g \end{pmatrix}, \quad \mathbf{H} = \begin{pmatrix} \rho w - \rho w_g \\ \rho u w + p - \rho u w_g \\ r\left(\rho v w - \rho v w_g\right) \\ \rho w w - \rho w w_g \\ \left(\rho e + p\right)w - \rho e w_g \end{pmatrix}$$

$$\mathbf{F}_v = \begin{pmatrix} 0 \\ \tau_{xx} \\ r\tau_{x\theta} \\ \tau_{xr} \\ u\tau_{xx} + v\tau_{x\theta} + w\tau_{xr} + q_x \end{pmatrix}, \quad \mathbf{G}_v = \begin{pmatrix} 0 \\ \tau_{\theta x} \\ r\tau_{\theta\theta} \\ \tau_{\theta r} \\ u\tau_{\theta x} + v\tau_{\theta\theta} + w\tau_{\theta r} + q_\theta \end{pmatrix}$$

$$\mathbf{H}_v = \begin{pmatrix} 0 \\ \tau_{rx} \\ r\tau_{r\theta} \\ \tau_{rr} \\ u\tau_{rx} + v\tau_{r\theta} + w\tau_{rr} + q_r \end{pmatrix}, \quad \mathbf{S} = \begin{pmatrix} 0 \\ 0 \\ 0 \\ \rho v^2/r \\ 0 \end{pmatrix}$$

In the above expressions,

$$\tau_{xx} = \tfrac{2}{3}\mu\left[2\tfrac{\partial u}{\partial x} - \tfrac{\partial w}{\partial r} - \tfrac{1}{r}\tfrac{\partial v}{\partial \theta}\right] - \rho\overline{u'u'}, \quad \tau_{\theta\theta} = \tfrac{2}{3}\mu\left[2\tfrac{1}{r}\tfrac{\partial v}{\partial \theta} - \tfrac{\partial u}{\partial x} - \tfrac{\partial w}{\partial r}\right] - \rho\overline{v'v'},$$
$$\tau_{rr} = \tfrac{2}{3}\mu\left[2\tfrac{\partial w}{\partial r} - \tfrac{1}{r}\tfrac{\partial v}{\partial \theta} - \tfrac{\partial u}{\partial x}\right] - \rho\overline{w'w'}, \quad \tau_{x\theta} = \tau_{\theta x} = \mu\left[\tfrac{\partial v}{\partial x} - \tfrac{1}{r}\tfrac{\partial u}{\partial \theta}\right] - \rho\overline{u'v'},$$
$$\tau_{\theta r} = \tau_{r\theta} = \mu\left[\tfrac{1}{r}\tfrac{\partial w}{\partial \theta} - \tfrac{\partial v}{\partial r}\right] - \rho\overline{v'w'}, \quad \tau_{rx} = \tau_{xr} = \mu\left[\tfrac{\partial x}{\partial r} - \tfrac{\partial w}{\partial x}\right] - \rho\overline{w'u'},$$

and

$$q_x = -k\tfrac{\partial T}{\partial x}, \quad q_\theta = -\tfrac{k}{r}\tfrac{\partial T}{\partial \theta}, \quad q_r = -k\tfrac{\partial T}{\partial r},$$

the continuity, momentum and energy conservation variables are represented by the field vector $\mathbf{U}$, the inviscid fluxes in the x, θ , and r directions are represented by the vectors $\mathbf{F}$, $\mathbf{G}$ and $\mathbf{H}$, and the viscous fluxes are represented by the vectors $\mathbf{F}_v$, $\mathbf{G}_v$ and $\mathbf{H}_v$. The grid velocities u_g, v_g and w_g used in the flux expressions account for the motion of the vibrating blade. The viscosity is taken as the sum of the laminar and turbulent viscosity. The laminar viscosity is taken from Sutherland's Law. Turbulence is accounted for by the turbulence viscosity using the Baldwin-Lomax [141] mixing length model, assuming that the random effect of turbulence can be treated in the same manner as in a steady flow. The coefficient of heat conductivity is linked to viscosity by the Prandtl number and the flow equations are closed by expressing pressure in terms of an assumed ideal gas.

3.1.2 Time-Averaged Equations

In the non-linear harmonic method, the flow equation is solved assuming that the unsteady flow field comprises of a time-averaged flow plus an unsteady perturbation, represented by

$$\mathbf{U}(x,\theta,r,t) = \bar{\mathbf{U}}(x,\theta,r) + \mathbf{U}'(x,\theta,r,t)$$

In contrast to linear harmonic methods, which superimpose the flow perturbation onto the steady solution, the nonlinear harmonic method bases the perturbation on a time-averaged flow, which is itself dependent on the unsteadiness. The time-averaged and unsteady conservative variables are therefore represented by

$$\overline{\mathbf{U}} = \begin{pmatrix} \overline{\rho} \\ (\overline{\rho u}) \\ r\,(\overline{\rho v}) \\ (\overline{\rho w}) \\ (\overline{\rho e}) \end{pmatrix} \quad \text{and} \quad \mathbf{U}' = \begin{pmatrix} \rho' \\ (\rho u)' \\ r\,(\rho v)' \\ (\rho w)' \\ (\rho e)' \end{pmatrix}$$

where $\bar{\mathbf{U}}$ is the vector of time-averaged conservative variables and $\mathbf{U}'$ is the vector of perturbation conservative variables. Similarly, the displacements and velocities of the computational mesh are separated into mean and unsteady parts, given by

$$x_g = \bar{x}_g + x'_g,\ \theta_g = \bar{\theta}_g + \theta'_g,\ r_g = \bar{r}_g + r'_g$$

and

$$u_g = \bar{u}_g + u'_g,\ v_g = \bar{v}_g + v'_g,\ w_g = \bar{w}_g + w'_g$$

Applying the equations to the unsteady nonlinear Navier-Stokes equation results in the time-averaged Navier-Stokes equation

$$\oint\!\!\!\oint_A \left(\overline{\mathbf{F}} - \overline{\mathbf{F}_V}\right) d\overline{A_x} + \left(\overline{\mathbf{G}} - \overline{\mathbf{G}_V}\right) d\overline{A_\theta} + \left(\overline{\mathbf{H}} - \overline{\mathbf{H}_V}\right) d\overline{A_r} + \left(\overline{\mathbf{F}' d\mathbf{A}'_x}\right) + \left(\overline{\mathbf{G}' d\mathbf{A}'_\theta}\right)$$
$$+ \left(\overline{\mathbf{H}' d\mathbf{A}'_r}\right) - \left(\overline{\mathbf{F}'_V d\mathbf{A}'_x}\right) - \left(\overline{\mathbf{G}'_V d\mathbf{A}'_\theta}\right) - \left(\overline{\mathbf{H}'_V d\mathbf{A}'_r}\right)$$
$$= \iiint_{\Delta V} \left(\overline{\mathbf{S}} d\overline{\mathbf{V}} + \overline{\mathbf{S}' d\mathbf{V}'}\right)$$

where the inviscid and viscous vectors are given by

$$\overline{\mathbf{F}} = \begin{pmatrix} \overline{\rho u} - \overline{\rho u_g} \\ (\overline{\rho u} - \overline{\rho u_g})\overline{u} + \overline{p} + \overline{(\rho u)'u'} - \overline{(\rho u_g)'u'} \\ r\left[(\overline{\rho u} - \overline{\rho u_g})\overline{v} + \overline{(\rho u)'v'} - \overline{(\rho u_g)'v'}\right] \\ (\overline{\rho u} - \overline{\rho u_g})\overline{w} + \overline{(\rho u)'w'} - \overline{(\rho u_g)'w'} \\ (\overline{\rho u} - \overline{\rho u_g})\overline{e} + \overline{pu} + \overline{p'u'} + \overline{(\rho u)'e'} - \overline{(\rho u_g)'e'} \end{pmatrix}$$

$$\overline{\mathbf{G}} = \begin{pmatrix} \overline{\rho v} - \overline{\rho v_g} \\ (\overline{\rho v} - \overline{\rho v_g})\overline{u} + \overline{(\rho v)'u'} - \overline{(\rho v_g)'u'} \\ r\left[(\overline{\rho v} - \overline{\rho v_g})\overline{v} + \overline{p} + \overline{(\rho v)'v'} - \overline{(\rho v_g)'v'}\right] \\ (\overline{\rho v} - \overline{\rho v_g})\overline{w} + \overline{(\rho v)'w'} - \overline{(\rho v_g)'w'} \\ (\overline{\rho v} - \overline{\rho v_g})\overline{e} + \overline{pv} + \overline{p'v'} + \overline{(\rho v)'e'} - \overline{(\rho v_g)'e'} \end{pmatrix}$$

$$\overline{\mathbf{H}} = \begin{pmatrix} \overline{\rho w} - \overline{\rho w_g} \\ (\overline{\rho w} - \overline{\rho w_g})\overline{u} + \overline{(\rho w)'u'} - \overline{(\rho w_g)'u'} \\ r\left[(\overline{\rho w} - \overline{\rho w_g})\overline{v} + \overline{(\rho w)'v'} - \overline{(\rho w_g)'v'}\right] \\ (\overline{\rho w} - \overline{\rho w_g})\overline{w} + \overline{p} + \overline{(\rho w)'w'} - \overline{(\rho w_g)'w'} \\ (\overline{\rho w} - \overline{\rho w_g})\overline{e} + \overline{pw} + \overline{p'w'} + \overline{(\rho w)'e'} - \overline{(\rho w_g)'e'} \end{pmatrix}$$

$$\overline{\mathbf{F}_V} = \begin{pmatrix} 0 \\ \overline{\tau}_{xx} \\ r\overline{\tau}_{x\theta} \\ \overline{\tau}_{xr} \\ \overline{u\tau}_{xx} + \overline{v\tau}_{x\theta} + \overline{w\tau}_{xr} + \overline{u'\tau'_{xx}} + \overline{v'\tau'_{x\theta}} + \overline{w'\tau'_{xr}} - \overline{q}_x \end{pmatrix}$$

$$\overline{\mathbf{G}_V} = \begin{pmatrix} 0 \\ \overline{\tau}_{\theta x} \\ r\overline{\tau}_{\theta\theta} \\ \overline{\tau}_{\theta r} \\ \overline{u\tau}_{\theta x} + \overline{v\tau}_{\theta\theta} + \overline{w\tau}_{\theta r} + \overline{u'\tau'_{\theta x}} + \overline{v'\tau'_{\theta\theta}} + \overline{w'\tau'_{\theta r}} - \overline{q}_\theta \end{pmatrix}$$

$$\overline{\mathbf{H}_V} = \begin{pmatrix} 0 \\ \overline{\tau}_{rx} \\ r\overline{\tau}_{r\theta} \\ \overline{\tau}_{rr} \\ \overline{u\tau}_{rx} + \overline{v\tau}_{r\theta} + \overline{w\tau}_{rr} + \overline{u'\tau'_{rx}} + \overline{v'\tau'_{r\theta}} + \overline{w'\tau'_{rr}} - \overline{q}_r \end{pmatrix}$$

$$\overline{\mathbf{S}} = \begin{pmatrix} 0 \\ 0 \\ 0 \\ \left[\overline{\rho v v} + \overline{(\rho v)' v'}\right] / r \\ 0 \end{pmatrix}$$

and

$$\overline{\tau}_{xx} = \frac{2}{3}\mu\left[2\frac{\partial \overline{u}}{\partial x} - \frac{\partial \overline{w}}{\partial r} - \frac{1}{r}\frac{\partial \overline{v}}{\partial \theta}\right], \quad \overline{\tau}_{\theta\theta} = \frac{2}{3}\mu\left[2\frac{1}{r}\frac{\partial \overline{v}}{\partial \theta} - \frac{\partial \overline{u}}{\partial x} - \frac{\partial \overline{w}}{\partial r}\right]$$

$$\overline{\tau}_{rr} = \frac{2}{3}\mu\left[2\frac{\partial \overline{w}}{\partial r} - \frac{1}{r}\frac{\partial \overline{v}}{\partial \theta} - \frac{\partial \overline{u}}{\partial x}\right], \quad \overline{\tau}_{x\theta} = \overline{\tau}_{\theta x} = \mu\left[\frac{\partial \overline{v}}{\partial x} + \frac{1}{r}\frac{\partial \overline{u}}{\partial \theta}\right]$$

$$\overline{\tau}_{\theta r} = \overline{\tau}_{r\theta} = \mu\left[\frac{1}{r}\frac{\partial \overline{w}}{\partial \theta} + \frac{\partial \overline{v}}{\partial r}\right], \quad \overline{\tau}_{rx} = \overline{\tau}_{xr} = \mu\left[\frac{\partial \overline{u}}{\partial r} + \frac{\partial \overline{w}}{\partial x}\right]$$

$$\overline{q}_x = -k\frac{\partial \overline{T}}{\partial x}, \quad \overline{q}_\theta = -k\frac{1}{r}\frac{\partial \overline{T}}{\partial \theta}, \quad \overline{q}_r = -k\frac{\partial \overline{T}}{\partial r}$$

The laminar and turbulent viscosity coefficients are based on the steady flow solution and are assumed to remain unchanged by the flow perturbations. This results in linear viscous terms in the momentum equations and non-linear terms in the energy equation.

A comparison between the time-averaged and the basic unsteady formulation shows that time-averaging produces additional terms in the momentum and energy equations due to non-linearity. The additional deterministic stress terms in the flux vectors are similar to the turbulence stress terms and are caused by the non-linear influence of the flow perturbations on the time-averaged flow. The non-linear harmonic method features an option to solve the deterministic stress terms in the solution, which is not implemented in the forced response calculations included in this thesis. The inclusion of the deterministic stress terms offers the basis of incorporating non-linearity into the analysis, marking the fundamental difference between

the non-linear harmonic method and time-linearised approaches. The extra terms shown in the time-averaged equation arise from non-linearities due to the movement of the computational mesh. Aeroelastic vibration amplitudes are generally of very small amplitude, so the additional terms in the time-averaged equation are assumed to be of negligible quantity, allowing them to be neglected in the analysis. The time-averaged equation is therefore simplified and written in the form

$$\oint\!\!\!\oint_A [(\overline{F} - \overline{F_V})d\overline{A}_x + (\overline{G} - \overline{G_V})d\overline{A}_\theta + (\overline{H} - \overline{H_V})d\overline{A}_r] = \iiint_{\Delta V} \overline{S}d\overline{V}$$

3.1.3 Harmonic Perturbation Equations

Unsteady flows of interest in turbomachinery are generally periodic in nature, where perturbations can be represented by Fourier series. In aeroelastic applications, only the flow harmonic at the respective blade resonant frequency needs to be calculated, assuming that flow harmonics outside the resonant frequency have no effect on the steady state dynamic response. This allows the flow perturbation to be modelled using the fundamental harmonic at the resonant frequency,

$$U' = \widetilde{U}e^{i\omega t}$$

Similarly, the mesh moving velocities u_g, v_g and w_g are represented in harmonic form

$$u_g = \bar{u}_g + \tilde{u}_g e^{i\omega t}, \quad v_g = \bar{v}_g + \tilde{v}_g e^{i\omega t}, \quad w_g = \bar{w}_g + \tilde{w}_g e^{i\omega t}$$

where

$$\tilde{u}_g = i\omega\tilde{x}, \quad \tilde{v}_g = i\omega\tilde{\theta}, \quad \tilde{w}_g = i\omega\tilde{r}$$

and the mesh is assumed to vibrate harmonically about its steady position

$$x = \bar{x} + \tilde{x}e^{i\omega t}, \quad \theta = \bar{\theta} + \tilde{\theta}e^{i\omega t}, \quad r = \bar{r} + \tilde{r}e^{i\omega t}$$

The full unsteady perturbation equations are defined by the difference between the original full equation and the time-averaged equation . The full perturbation equations containing high-order derivatives can not easily be solved in the frequency domain, therefore the first-order terms are assumed to dominate in order to simplify the calculation. Retaining only the first-order terms of the full unsteady flow

equations, the unsteady perturbation equations are given by

$$\oint\!\!\!\!\!\!\iint_A [(\widetilde{F}-\widetilde{F_V})d\overline{A}_x + (\widetilde{G}-\widetilde{G_V})d\overline{A}_\theta + (\widetilde{H}-\widetilde{H_V})d\overline{A}_r + (\overline{F}-\overline{F_V})d\widetilde{A}_x$$
$$+ (\overline{G}-\overline{G_V})d\widetilde{A}_\theta + (\overline{H}-\overline{H_V})d\widetilde{A}_r] = \iiint_{\Delta V} (\overline{S}d\widetilde{V} + \widetilde{S}d\overline{V}) - i\omega \iiint_{\Delta V} (\overline{U}d\widetilde{V} + \widetilde{U}d\overline{V})$$

where

$$\widetilde{F} = \begin{pmatrix} (\widetilde{\rho u}) - (\widetilde{\rho u_g}) \\ (\overline{\rho u} - \overline{\rho u_g})\widetilde{u} + [(\widetilde{\rho u}) - (\widetilde{\rho u_g})]\,\overline{u} + \widetilde{p} \\ r\,[(\overline{\rho u} - \overline{\rho u_g})\widetilde{v} + [(\widetilde{\rho u}) - (\widetilde{\rho u_g})]\,\overline{v}] \\ (\overline{\rho u} - \overline{\rho u_g})\widetilde{w} + [(\widetilde{\rho u}) - (\widetilde{\rho u_g})]\,\overline{w} \\ (\overline{\rho e} + \overline{p})\widetilde{u} + [(\widetilde{\rho e}) + \widetilde{p}]\,\overline{u} - \overline{\rho e}\widetilde{u_g} - (\widetilde{\rho e})\overline{u_g} \end{pmatrix}$$

$$\widetilde{G} = \begin{pmatrix} (\widetilde{\rho v}) - (\widetilde{\rho v_g}) \\ (\overline{\rho v} - \overline{\rho v_g})\widetilde{u} + [(\widetilde{\rho v}) - (\widetilde{\rho v_g})]\,\overline{u} \\ r\,[(\overline{\rho v} - \overline{\rho v_g})\widetilde{v} + [(\widetilde{\rho v}) - (\widetilde{\rho v_g})]\,\overline{v} + \widetilde{p}] \\ (\overline{\rho v} - \overline{\rho v_g})\widetilde{w} + [(\widetilde{\rho v}) - (\widetilde{\rho v_g})]\,\overline{w} \\ (\overline{\rho e} + \overline{p})\widetilde{v} + [(\widetilde{\rho e}) + \widetilde{p}]\,\overline{v} - \overline{\rho e}\widetilde{v_g} - (\widetilde{\rho e})\overline{v_g} \end{pmatrix}$$

$$\widetilde{H} = \begin{pmatrix} (\widetilde{\rho w}) - (\widetilde{\rho w_g}) \\ (\overline{\rho w} - \overline{\rho w_g})\widetilde{u} + [(\widetilde{\rho w}) - (\widetilde{\rho w_g})]\,\overline{u} \\ r\,[(\overline{\rho w} - \overline{\rho w_g})\widetilde{v} + [(\widetilde{\rho w}) - (\widetilde{\rho w_g})]\,\overline{v}] \\ (\overline{\rho w} - \overline{\rho w_g})\widetilde{w} + [(\widetilde{\rho w}) - (\widetilde{\rho w_g})]\,\overline{w} + \widetilde{p} \\ (\overline{\rho e} + \overline{p})\widetilde{w} + [(\widetilde{\rho e}) + \widetilde{p}]\,\overline{w} - \overline{\rho e}\widetilde{w_g} - (\widetilde{\rho e})\overline{w_g} \end{pmatrix}$$

$$\widetilde{F_V} = \begin{pmatrix} 0 \\ \tau_{xx} \\ r\widetilde{\tau_{x\theta}} \\ \widetilde{\tau_{xr}} \\ \overline{u}\widetilde{\tau_{xx}} + \overline{v}\widetilde{\tau_{x\theta}} + \overline{w}\widetilde{\tau_{xr}} + \widetilde{u}\overline{\tau_{xx}} + \widetilde{v}\overline{\tau_{x\theta}} + \widetilde{w}\overline{\tau_{xr}} - \widetilde{q_x} \end{pmatrix}$$

$$\widetilde{G_V} = \begin{pmatrix} 0 \\ \tau_{\theta x} \\ r\widetilde{\tau_{\theta\theta}} \\ \widetilde{\tau_{\theta r}} \\ \overline{u}\widetilde{\tau_{\theta x}} + \overline{v}\widetilde{\tau_{\theta\theta}} + \overline{w}\widetilde{\tau_{\theta r}} + \widetilde{u}\overline{\tau_{\theta x}} + \widetilde{v}\overline{\tau_{\theta\theta}} + \widetilde{w}\overline{\tau_{\theta r}} - \widetilde{q_\theta} \end{pmatrix}$$

$$\widetilde{H_V} = \begin{pmatrix} 0 \\ \tau_{rx} \\ r\widetilde{\tau_{r\theta}} \\ \widetilde{\tau_{rr}} \\ \overline{u}\widetilde{\tau_{rx}} + \overline{v}\widetilde{\tau_{r\theta}} + \overline{w}\widetilde{\tau_{rr}} + \widetilde{u}\overline{\tau_{rx}} + \widetilde{v}\overline{\tau_{r\theta}} + \widetilde{w}\overline{\tau_{rr}} - \widetilde{q_r} \end{pmatrix}$$

$$\widetilde{S} = \begin{pmatrix} 0 \\ 0 \\ 0 \\ [(\widetilde{\rho v})\overline{v} + (\overline{\rho v})\widetilde{v}]/r \\ 0 \end{pmatrix}$$

3.1.4 Boundary Equations

The analysis is performed for a single blade-blade passage, which requires the flow conditions to be defined for inlet, outlet, periodic and blade surface boundaries. Conventional steady flow boundary conditions are applied in the time-averaged solution. For the time-averaged equations, the flow variables at the upper and lower periodic boundaries are subject to a direct repeating condition, enforcing an identical time-averaged flow in all passages in the bladerow. The first-order perturbation equations are subject to phase-shifted periodic boundary conditions, where identical flow disturbances are experienced by each passage subject to a phase difference defined by the interblade phase angle. For example, a harmonic perturbation on the upper boundary, $\tilde{\mathbf{U}}_U$, is expressed in terms of the perturbation seen on the lower boundary, $\tilde{\mathbf{U}}_L$, by

$$\tilde{\mathbf{U}}_U = \tilde{\mathbf{U}}_L e^{i\sigma} \tag{3.2}$$

where σ is the interblade phase angle. For the time-averaged flow, stagnation pressure, stagnation temperature and flow angle are specified at inlet and static pressure is defined at outlet. Non-reflecting boundary conditions are defined at inlet and outlet using either the one-dimensional condition of Giles [142] or the two-dimensional condition of Saxer and Giles [143]. Two different conditions can be used for the solid wall boundary for inviscid and viscous calculations using either a no slip wall boundary or a slip wall boundary treatment. Both approaches apply zero flux across

the solid boundary. The no-slip wall condition sets the velocities on the blade surface to zero and the wall shear stress is calculated using the local velocity gradients, requiring a fine mesh resolution around the boundary. The slip wall condition approximates the wall shear stress by the log law formulation of Denton [144].

3.1.5 Solution Method

The unsteady solution is performed by pseudo-time marching the flow equations in order to take advantage of the efficient time-marching schemes that have been extensively developed for steady flows. A pseudo-time variable, t, is introduced into both the time-averaged and first order perturbation equations, in a similar manner to conventional steady flow and linearised methods. The time-averaged and perturbation equations, therefore become

$$\frac{\partial}{\partial t'}\iiint_{\Delta V}(\overline{U}d\overline{V}) + \oiint_{A}[(\overline{F}-\overline{F_V})d\overline{A_x} + (\overline{G}-\overline{G_V})d\overline{A_\theta} + (\overline{H}-\overline{H_V})d\overline{A_r}] = \iiint_{\Delta V}(\overline{S}d\overline{V})$$

and

$$\begin{aligned}\frac{\partial}{\partial t'}\iiint_{\Delta V}(\widetilde{U}d\overline{V}) + \oiint_{A}[&(\overline{F}-\overline{F_V})d\widetilde{A_x} + (\overline{G}-\overline{G_V})d\widetilde{A_\theta} + (\overline{H}-\overline{H_V})d\widetilde{A_r} \\ &+ (\widetilde{F}-\widetilde{F_V})d\overline{A_x} + (\widetilde{G}-\widetilde{G_V})d\overline{A_\theta} + (\widetilde{H}-\widetilde{H_V})d\overline{A_r}] \\ &= \iiint_{\Delta V}(\widetilde{S}d\overline{V} + \overline{S}d\widetilde{V}) - i\omega\iiint_{\Delta V}(\overline{U}d\widetilde{V} + \widetilde{U}d\overline{V})\end{aligned}$$

The pseudo-time derivatives disappear after convergence, recovering the original time-averaged and perturbation equations. The flow equations are effectively transformed into two steady state equations, allowing standard steady solution acceleration techniques to be adopted, such as local time stepping and multiple grid techniques.

The spatial discretisation of the equations is made using the cell-centred finite volume method, which is a spatial second-order central difference scheme. A 2nd and 4th order adaptive smoothing method is implemented in order to reduce numerical oscillations and capture shock waves in the time-averaged flow.

The time-averaged and perturbation equations are solved in a coupled manner in order to capture the non-linear interaction between the time-averaged flow and

unsteady disturbances. The entire system of equations and are solved simultaneously using a 4-stage Runge-Kutta pseudo-time marching scheme. For the solution of the time-averaged equations at each fractional step in the Runge-Kutta scheme, the deterministic stress terms must be resolved. For periodic unsteady flow, the deterministic stress terms are evaluated directly from the phase and amplitude of the perturbations, obtained from the complex components of the 1st harmonic velocity perturbations.

3.1.6 The TF3D Flow Solver

The nonlinear harmonic method is carried out by the 3D CFD code TF3D, which has the additional ability to run as a purely time-linearised solver. The TF3D code has been developed by the University of Durham and validated for a range of oscillating blade and bladerow interaction applications, including:

- 2D wake/blade interaction in a uniform inviscid steady flow past an unloaded flat plate cascade, discussed by Chen et al [49]. The validity of the basic linear unsteady perturbation solver is demonstrated with a comparison against the results of LINSUB, a widely-used linear inviscid analytic program.

- 3D oscillating flat plate cascade, proposed by He and Denton [21]. The test case consists of a simple linear flat plate cascade, with vibration in the 1st torsion mode with uniform subsonic flow a zero incidence. Calculated results for unsteady pressure coefficient at 2D radial sections are compared with the 3D semi-analytical lifting surface method of Namba and Ishikawa [145].

- 3D bladerow interaction for the Alstom $2\frac{1}{2}$ stage transonic compressor case, as reported by He et al. [146]. The $2\frac{1}{2}$ stage steady viscous solution using mixing plane treatment is compared with experimental data. The effects of rotor-rotor interaction are investigated with the 3D unsteady multi-stage calculation.

- Bladerow interaction of the VKI BRITE-EURAM transonic turbine stage, as reported by Ning et al. [50]. The unsteady flow in the vane-rotor stage at

normal operating condition is calculated, solving the time-linearised Navier-Stokes equations. Predicted pressures over the rotor blade surfaces are validated against test data.

3.2 Structural Modelling

3.2.1 Finite Element Modelling

As discussed in Section 2.4.1, FEA discretises the distribution of a variable through a complex geometry by dividing the region into small elements of simple geometries, interconnected mathematically at the nodes. The governing equations for each element are assembled into matrix form to give the system equations. The manner in which the element equations are constructed is dependant on the nature of the physical problem, which fall into the following three categories for structural mechanics:

(1) *Steady-state problems.* Steady state or equilibrium problems are the most commonly-used aspect of the FE method. In structural mechanics, the elastic analysis of a body under equilibrium provides the static displacements of the body due to the applied loads. This is used for stress analysis, where the resulting material stresses are derived from the nodal displacements. Such problems are governed by a matrix equation of the form

$$[K]\{X\} = \{F\}$$

where $[K]$ is the stiffness matrix, found by summing all the element matrices, $\{X\}$is the vector of nodal displacements and $\{F\}$ is the vector of applied nodal forces.

(2) *Dynamic problems.* Dynamic problems include the effects of inertial force, obeying Newtons 2nd law, introducing a time-dependency into the system equations. Dynamic problems usually contain dissipative non-conservative forces and are represented by the matrix equation

$$[M]\left\{\ddot{X}\right\} + [C]\left\{\dot{X}\right\} + [K]\{X\} = \{F(t)\}$$

where $[M]$ and $[C]$ are the total mass and damping matrices of the structure and $\{\ddot{X}\}$, $\{\dot{X}\}$, and $\{X\}$ are the nodal accelerations, velocities and displacements. The solution of the system equations yields a time-varying or dynamic response of the system.

(3) *Eigenvalue problems.* Eigenvalues describe the values of a certain important parameter that cause the system to fall into a characteristic type of behaviour. In

structural dynamics, the natural frequencies and mode shapes of free vibration are given by the solution of the eigenvalue problem in a modal analysis. Here, the dynamic equation reduces to

$$[M]\left\{\ddot{X}\right\} + [K]\{X\} = \{0\} \tag{3.3}$$

which is solved to yield the natural frequencies and modeshapes of the system. The resulting eigenvectors and eigenfrequencies form the basis for subsequent calculations based on Modal Reduction.

3.2.2 Modal Reduction Method

As discussed in section 2.4.2, forced vibration at an arbitrary frequency can be modelled with the modal superposition technique by superimposing the dynamic response of several modes in the relevant frequency range. This approach decouples the large system of coupled equations in the FE model to a series of individual modal equations.

The forced response analysis of gas turbine blades is generally concerned with resonant vibration at frequencies very close to the natural frequency of interest. It is generally accepted that resonant vibration of lightly-damped blades is characterised by harmonic motion in the corresponding mode shape with virtually no contribution from any other mode. This allows the response to be calculated using the modal reduction method in a similar manner to the modal superposition technique, with the difference being that only the single mode of interest included in the analysis.

The modal reduction method is based on the results of the eigenvalue solution provided by a FE modal analysis, where the natural frequencies relate to the eigenvalues and the modeshapes are given by the eigenvectors. The analysis is performed in modal space, where all FE matrix coefficients and force vectors are converted into modal values before being applied to the single-DoF modal equation. The solution of the modal equation yields the modal amplitude which is used to scale the eigenvector, providing the physical response amplitudes of all nodes on the FE mesh.

Natural Frequencies and Modeshapes

The basis for the modal reduction technique is a modal analysis performed on the FE model, yielding the natural frequencies and modeshapes of free vibration. The modal analysis involves the solution of the eigenvalue problem (Equation 3.3) to provide the natural frequencies (eigenvalues) and modeshapes (eigenvectors). Assuming harmonic forcing and motion, the eigensolution is given by the linear equation

$$\left[K - \omega_i^2 M\right] \{\phi\}_i = \{0\} \tag{3.4}$$

For a system of n degrees of freedom, Equation 3.4 represents a coupled series of n linear homogeneous equations, where both the eigenvalue, ω_i^2 and eigenvector $\{\phi_i\}$ of any eigensolution, i, are unknown. For any non-zero eigensolution, the determinant of the eigenvector coefficient must reduce to zero, i.e.

$$\left\|K - \omega_i^2 M\right\| = \{0\}$$

giving a series of n eigenvalues. If all the eigenvalues are distinct, there exists a non-trivial solution to Equation 3.4 in $\{\phi_i\}$. The modeshape eigenvector for any specific natural frequency is then given by substituting the frequency into Equation 3.4. The resulting eigenvector has an arbitrary amplitude and the modeshape values are relative, describing only the shape of vibration for an arbitrary scale. Thus, the equation can be solved for the relative modeshape once any one of the displacements has been specified at an arbitrary value. It is most convenient to choose a scale such that the modal mass is set to unity, given by

$$\{\phi_i\}^{\mathrm{T}} [M] \{\phi_i\} = 1 \tag{3.5}$$

then the modal stiffness is intrinsically set to a value of $k_i = \omega_i^2$, where,

$$\{\phi_i\}^{\mathrm{T}} [K] \{\phi_i\} = \omega_i^2 \tag{3.6}$$

This mass-normalising of the modeshape greatly simplifies the implementation of modal reduction in forced response analysis, where the mass and stiffness variables are subsequently eliminated from the modal equation.

Modal Superposition

The eigenvectors are orthogonal with respect to the mass and stiffness matrices, thus for any eigenvalue, r, in relation to another eigenvalue, s, the orthogonality condition can be shown as

$$\{\phi_r\}^T [M] \{\phi_s\} = 0, \quad \{\phi_r\}^T [K] \{\phi_s\} = 0 \tag{3.7}$$

The orthogonality of eigenvectors means that the dynamic responses of individual modes can be calculated independently, then linearly superimposed. In a forced response analysis, the solution of each mode yields the modal amplitude which is subsequently used to scale each eigenvector to give the physical modal displacements. The modal responses can then be superimposed, providing the total structural response. The finite element dynamic equations of the full model are written in the form

$$[M] \left\{\ddot{X}(t)\right\} + [C] \left\{\dot{X}(t)\right\} + [K] \{X(t)\} = \{F(t)\} \tag{3.8}$$

where $\{X\}$ is the vector of nodal displacements and $\{F\}$ is the vector of excitation forces. The principle of linear modal superposition allows the structural response to be made up of a combination of natural modes, each multiplied by the modal amplitude in the form

$$\{X(t)\} = [\phi] \{q(t)\} = q_1(t) \{\phi\}_1 + q_2(t) \{\phi)\}_2 + \ldots + q_n(t)\{\phi\}_n \tag{3.9}$$

where $\{q\}$ is the vector of the individual modal amplitudes, q_i, and $[\phi]$ is the eigenvector matrix, the columns of which represent each eigenvector. Substituting 3.9 into 3.8 and pre-multiplying by $[\phi]^{\mathrm{T}}$ gives

$$[\phi]^{\mathrm{T}} [M] [\phi] \{\ddot{q}\} + [\phi]^{\mathrm{T}} [C] [\phi] \{\dot{q}\} + [\phi]^{\mathrm{T}} [K] [\phi] \{q\} = [\phi]^{\mathrm{T}} \{F\} \tag{3.10}$$

Both the mass and stiffness matrices are diagonal due to the orthogonality conditions 3.7, but the damping matrix is not generally diagonal. Considering damping in the form of a modal damping ratio, ζ_i , for each mode allows Equation 3.10 to be expressed as a series of decoupled scalar modal equations

$$\ddot{q}_i + 2\zeta\omega_i\dot{q}_i + \omega_i^2 q_i = f_i \qquad i = 1, 2, \ldots, n$$

with the modal mass of unity and the modal stiffness of ω_i^2, defined by Equations 3.5 and 3.6. The modal force is then obtained from the physical force vector by

$$f_i = \{\phi\}_i^{\mathrm{T}} \{F\}. \tag{3.11}$$

The modal equations are solved in either the time or frequency domain to give the modal amplitudes of all modes included in the analysis. The solution is subsequently transformed into physical space using Equation 3.9.

Single Degree of Freedom Modelling

As previously discussed, resonant vibration very close to a natural frequency is dominated by the corresponding mode, allowing the influence of all other modes to be neglected from the analysis. From the mode orthogonality condition (Equation 3.7), the series of decoupled of equations can be further condensed to one single-DoF modal equation for that particular mode. To simplify algebraic notation, the subscript, i, defining mode number is omitted from the remainder of this text, as the following aeromechanical methods consider only one mode during any analysis. The format of the modal equation for any given mode is, therefore

$$\ddot{q}(t) + 2\zeta\omega_i\dot{q}(t) + \omega_i^2 q(t) = f(t)$$

where

$$q(t) = \{\phi\}^{\mathrm{T}} \{X(t)\}, \text{ and } f(t) = \{\phi\}^{\mathrm{T}} \{F(t)\}.$$

The modal equation can be directly solved in its current form by means of numerical integration in the time domain. However, it is more convenient to make the assumption of harmonic forcing and motion,

$$f = \tilde{f}e^{\mathbf{i}\omega t}, \quad q_i = \tilde{q}_i e^{\mathbf{i}\omega t},$$

and expressing the modal equation in terms of complex amplitudes

$$\ddot{\tilde{q}}_i + 2\zeta\omega_i\dot{\tilde{q}}_i + \omega_i^2\tilde{q}_i = \tilde{f}_i, \tag{3.12}$$

which can be rewritten as

$$-\omega^2\tilde{q}_i + 2\mathbf{i}\zeta\omega\omega_i\tilde{q}_i + \omega_i^2\tilde{q}_i = \tilde{f}_i$$

(3.13)

allowing the solution to be solved analytically, or indeed by numerical integration techniques.

The application of aerodynamic forces to the modal equation is described in detail in Section 4.3 and is summarised here. The aerodynamic excitation forces from the CFD forcing calculation are transformed from the complex force distribution over the blade into a single complex modal force using

$$\tilde{f} = \sum_{j=1}^{n} \left\{ \phi_j \cdot \left(F_j^{\Re} + \mathbf{i} F_j^{\Im} \right) \right\} \tag{3.14}$$

Aerodynamic damping can be considered in terms of an equivalent viscous damping ration ζ_{aero}, which is calculated from the work done on the blade by the fluid in a CFD damping calculation. Work is calculated in physical terms by integrating the aerodynamic damping force distribution, to give

$$W_d^{cfd} = \pi \sum_{j=1}^{n} \left(D_j^{\Im} x_j \right)^{cfd}, \tag{3.15}$$

where x_j^{cfd} is the absolute displacement amplitude at a given point on the blade surface. The aerodynamic damping ratio is calculated from the work based on the principle of equivalent viscous damping,

$$\zeta_{aero} = \frac{-W_d^{cfd}}{2\pi\omega_i^2 \left(q^{cfd}\right)^2} \tag{3.16}$$

3.3 Friction Damping Modelling

3.3.1 Macroslip Models

Macroslip friction models, commonly known as *Coulomb friction* models, treat the two bodies in contact as perfectly rigid, disallowing any flexibility of the bulk material around the contact surfaces. This results in the entire contact surface behaving as a solid block, which is either in a state of gross stick or gross slip. The friction behaviour of the surface is described by the coefficient of friction, which is defined as the force required to initiate or maintain sliding of a friction surface, and is given by the ratio of the tangential to the normal force, as

$$\mu = \frac{F_t}{F_n}. \tag{3.17}$$

The friction coefficient is therefore used to determine the point at which slip occurs and the maximum tangential friction force that can be sustained by the contact. In other words, sliding motion can only be achieved after a critical tangential force is applied and the maximum friction force is exceeded. Two variations of the macroslip friction approach are considered: Rigid Coulomb and Elastic Coulomb. Rigid Coulomb is the most commonly-known representation of friction, which neglects the elastic behaviour of the contact surface and permits tangential motion only after the critical tangential force is applied. Elastic Coulomb friction, however, encompasses the gross elastic deformation of the asperity junctions with the inclusion of an elastic contact stiffness. The elastic model provides a degree of tangential displacement before the critical tangential load is applied and gross slip occurs. Whilst the rigid Coulomb model offers a simple approximation suitable for dynamic problems with large sliding displacements, the Elastic Coulomb model offers a better approximation for cases with relatively low tangential motion.

Rigid Coulomb Friction

The rigid Coulomb model neglects any elastic tangential deformation of the contact surface, permitting gross sliding of the entire surface only after the elastic limit is reached. This approach can be visualised by considering a brick on a rough surface,

as illustrated in Figure 3.1. The contact surface has friction coefficient, μ, is subject to a normal force F_n. If a tangential load, F, of increasing magnitude is gradually applied to the brick, it initially remains stuck and does not move until the tangential force reaches a critical value. Below the critical value, the contact surface imposes a friction shear force on the brick, maintaining equilibrium with the applied force and preventing motion. Once the critical tangential force is exceed, the friction force reaches a maximum value, given by

$$F_t^{lim} = \mu F_n, \tag{3.18}$$

after which, equilibrium is lost and the brick slides.

Now considering the brick to be subject to a tangential displacement, it is seen in Figure 3.2 that the friction force remains constant for any given sliding displacement, with the direction opposing motion. Applying a harmonic tangential displacement at the friction surface gives a friction force in the form of a square wave, as shown in Figure 3.3. Plotting the friction force against tangential displacement provides the hysteresis curve provided in Figure 3.4. The friction work done over one cycle is considered as the area enclosed within the hysteresis curve, given by

$$\begin{aligned} W_f &= \left\{F_t^{lim} - (-F_t^{lim})\right\}\left\{x^{max} - (-x^{max})\right\} \\ &= 4F_t^{lim}x^{max} \\ &= 4\mu F_n x^{max}. \end{aligned} \tag{3.19}$$

The equivalent viscous damping ratio is obtained in a similar manner to aerodynamic damping in Equation 4.23, to give

$$\zeta_{aero} = \frac{-W_f}{2\pi\omega^2\left(x^{max}\right)^2}. \tag{3.20}$$

A note of caution is given when the friction damping is represented by the viscous model. It can be seen in Equation 3.19 that the friction damping work is proportional to the displacement amplitude. However, it is discussed later in Section 4.4 that viscous damping work is proportional to the square of the displacement amplitude. This means that friction damping can not be accurately represented by the viscous model, with the consequence that the equivalent viscous damping ratio calculated at one vibration amplitude is not valid at any other amplitude. This point

is illustrated in Figure 3.5, where the equivalent viscous damping ratio is plotted against displacement amplitude, to show that the effect of rigid Coulomb damping decays with increasing displacement. It is therefore highlighted that a great deal of caution must be used when friction is expressed in terms of an equivalent viscous damping ratio.

Elastic Coulomb Friction

The Elastic Coulomb model is an extension to the rigid model that incorporates a linear elastic contact stiffness to represent the elastic deformation of the contact asperities before the elastic limit is reached. The Elastic Coulomb model can be visualised by considering the contact surface as a brush on a flat surface with uniform bristles and rigid body, which is subject to a normal force. As illustrated in Figure 3.6, the bristles of the brush deform elastically for a small applied tangential load, giving a small amount of tangential defloection of the brush body. If the tangential load is gradually increased, the bristles will deform elastically until a critical point, after which gross sliding occurs. This initial elastic motion is representative of the elastic deformation experienced by the contact asperities before the yield stresses are reached and plastic deformation takes place.

The Elastic Coulomb model therefore behaves a similar same way to the Rigid Coulomb model, with the exception that contact surface deforms elastically during gross stick. Considering the contact surface to be subject to an increasing tangential displacement, Figure 3.7 shows the friction force as the surface is displaced from an initial position. For tangential loads below the critical value, the contact surface deforms with an elastic contact stiffness, k_t. Once the elastic limit is reached, the friction force remains fixed and gross sliding occurs. Defining the elastic contact stiffness as

$$k_t = \frac{dF_t}{dx} \tag{3.21}$$

the displacement given by a tangential force under elastic conditions is given by

$$dx = \frac{dF_t}{k_t}. \tag{3.22}$$

It is known that the maximum friction force, given by Equation 3.18, is achieved at

the point of slip. Therefore, the displacement at the elastic limit is given by

$$x^{lim} = \frac{\mu F_n}{k_t}. \tag{3.23}$$

For any tangential displacement less than than the critical value, the friction surface will behave like a spring with purely elastic deformation. Once the elastic limit is exceeded, gross sliding will occur as in the Rigid Coulomb Model. The resulting hysteresis curves for a range of displacement amplitudes are shown in Figure 3.8. The first graph shows the purely elastic behaviour, for small displacements below the elastic limit; the second graph shows the hysteresis curve for a displacement slightly greater than the elastic limit; whilst the third graph shows the behaviour for very large displacements relative to the elastic limit. From these three graphs, it can be seen that: a) zero damping is achieved for the purely elastic case with very small amplitudes; and b) the elastic model behaves similarly to the rigid model for large displacements, where the elastic part of the curve becomes less significant. This highlights the limitation of the Elastic Coulomb model for small displacements and also explains why the simpler rigid model is used in most engineering applications, where sliding displacements are usually far greater than the elastic limit.

Knowing that the area of a parallelogram is equal to the product of the base and height, the work done by the Elastic Coulomb model is therefore equal to

$$W_f = 4x^{slip}F^{lim} \tag{3.24}$$

where x^{slip} is the slip displacement, which is non-zero when the elastic limit is exceeded and is defined by

$$x^{slip} = \begin{cases} 0, & x^{max} \leq x^{lim} \\ x^{max} - x^{lim}, & x^{max} > x^{lim} \end{cases} \tag{3.25}$$

Expressing the friction work in Equation 3.27 in this form gives

$$W_f = \begin{cases} 0, & x^{max} \leq x^{lim} \\ 4F_f^{lim}\left(x^{max} - x^{lim}\right), & x^{max} > x^{lim} \end{cases} \tag{3.26}$$

Substituting the expressions for F^{lim} and x^{lim} in Equations 3.18 and 3.23 into

the above expression defines the Elastic Coulomb friction work as

$$W_f = \begin{cases} 0, & x^{max} \leq x^{lim} \\ 4\mu F_n \left(x^{max} - \frac{\mu F_n}{k_t} \right), & x^{max} > x^{lim} \end{cases} \tag{3.27}$$

The equivalent viscous damping ratio is gained by substituting the work into Equation 3.20 giving

$$W_f = \begin{cases} 0, & x^{max} \leq x^{lim} \\ \frac{2\mu F_n \; x^{max} - \frac{\mu F_n}{k_t}}{\pi \omega^2 (x^{max})^2}, & x^{max} > x^{lim} \end{cases} \tag{3.28}$$

Figure 3.9 provides a graphical representation of the Elastic Coulomb friction work and equivalent viscous damping ratio as functions of displacement amplitude. Here it can be seen that the work is zero for small displacements, but increases linearly once the elastic limit is exceeded. The damping ratio remains at zero for small displacements, increases to a maximum value soon after as gross slip is achieved, then decays towards zero as the displacements are further increased.

3.3.2 Microslip Model

Microslip models predict friction due to small-scale displacements with greater accuracy than the Coulomb models by accounting for the contributions of individual asperities before gross sliding occurs. Representing asperity geometries as statistical distribution allows the population of highly-loaded asperities to deform plastically and contribute to damping before gross slip is achieved. This approach does not assume a rigid bulk material, thus allowing some regions of the contact surface to remain stuck, whilst other parts achieve sliding. The result of this method is that a degree of plastic sliding, and therefore hysteretic damping, is achieved before gross sliding is predicted by the Coulomb models, thus providing a more realistic representation of the physical problem.

The microslip model implemented in this project was proposed by Hagman [131] and applied by Olofsson [130], who provides a detailed description of the model with examples. In this thesis, the original friction equations derived by Hagman and Olofsson are further extended for use in a linear FE friction model.

In the microslip model, the shape of the asperities is assumed to be spherical, with equal radii and uniform height distribution. The elastic behaviour of each individual asperity is determined by Hertz theory, which states that the compound elastic modulus for two spheres under normal loading is given by

$$\frac{1}{E^*} = \frac{1-\nu_1^2}{E_1} + \frac{1-\nu_2^2}{E_2} \tag{3.29}$$

where E and ν are the elastic modulus and Poisson's ratio of each material. Similarly, the compound shear modulus is stated as

$$\frac{1}{G^*} = \frac{2-\nu_1^2}{G_1} + \frac{2-\nu_2^2}{G_2} \tag{3.30}$$

For a contact surface under an applied normal load, the number of asperities in contact is assumed to increase linearly with the normal approach of the surfaces. The expression

$$N = Cz \tag{3.31}$$

relates the number of asperity junctions per unit area, N, to the normal approach, z, by the surface contact parameter, C. The normal approach is the deformation of the bulk material in the normal direction due to an applied normal pressure, and is given by the expression

$$z = \left(\frac{15P}{8E^*CA_0R^{\frac{1}{2}}}\right)^{0.4} \tag{3.32}$$

The total friction load over the contact surface is taken to be the sum of the forces from all asperities in elastic and plastic contact, given by

$$F_f = \sum F_{spring} + \sum F_{slip} \tag{3.33}$$

where F_{spring} is the friction force of each contact asperity under elastic Hertzian contact and F_{slip} is the friction force of each asperity undergoing plastic flow. The force during initial loading with an increasing tangential displacement from the rest position is shown in Figure 3.10. During the range of microslip from the rest position up to the slip limit, x^{lim}, the total frictional load is obtained by integrating the contribution of each individual asperity over the whole surface, which is stated by Olofsson [130] to be given by

$$F_f = \frac{8}{15}\mu CA_0E^*R^{\frac{1}{2}}\left[z^{\frac{5}{2}} - \left(z - \frac{4G^*x}{\mu E^*}\right)^{\frac{5}{2}}\right] \tag{3.34}$$

Equation 3.34 is valid up to the slip limit given by

$$x^{lim} = \frac{z\mu E^*}{4G^*} \tag{3.35}$$

After the slip limit is exceeded and gross slip occurs, the friction force is given by Equation 3.17 in an identical manner to the Coulomb models.

The hysteresis curve for cyclic tangential displacement from an initial rest point is provided in Figure 3.11. After the peak tangential displacement, x^{max}, is reached after the initial loading, the direction of motion is reversed. The residual slip strain is unloaded, before reloading occurs in the opposite direction. The size of the microslip region during unloading and reloading is equal to twice the size of the microslip displacement of the initial loading condition. The friction force during microslip in the reverse part of the cycle, returning from a maximum positive displacement of x^{max} to a maximum negative displacement of $-x^{max}$ is given by

$$F_f = F_f^{max} - \frac{16}{15}\mu C A_0 E^* R^{\frac{1}{2}} \left[z^{\frac{5}{2}} - \left(z - \frac{2G^*\left(x^{max} - x\right)}{\mu E^*} \right)^{\frac{5}{2}} \right] \tag{3.36}$$

where F^{max} is the peak friction force at the maximum positive displacement, x^{lim}. If the elastic limit is exceeded on the return stroke and gross slip occurs then the friction force is given by $-F_t^{lim}$.

Similarly, once the maximum negative displacement on the return stroke is reached and the forward motion recommences, the signs of F^{max} and x^{max} in Equation 3.36 are reversed and the friction force is given using Equation 3.36.

The dissipated work done by the friction force over one vibratory cycle is given by the area enclosed within the hysteresis curve. The work done within the microslip region for displacement amplitudes up to the slip limit, as shown in Figure 3.12, is calculated by integrating the microslip force over one cycle. The microslip work is stated by Olofsson [130] to be

$$W_{ms} = \frac{4}{7}\left[14\mu P x^{lim} + \frac{P\left(\mu E^* z - 4G^* x^{lim}\right)^{\frac{7}{2}}}{\mu^{\frac{3}{2}} E^{*\frac{5}{2}} z^{\frac{5}{2}} G^*} - \frac{\mu^2 E^* z P}{G^*} - 7F^{lim} x^{lim} \right] \tag{3.37}$$

Equation 3.37 is only valid within the microslip range for displacement amplitudes up to the slip limit, given by Equation 3.35. Figure 3.13 shows graphically the work done during both microslip and gross sliding regions when the displacement

amplitude exceeds the slip limit. The areas are divided up into a parallelogram of equal area to the sliding work, and two microslip regions of combined area equal to the microslip work shown in Figure 3.12. The microslip work is equal to value given by Equation 3.37 for a displacement amplitude of $x^{max} = x^{lim}$ at the slip limit. The sliding work is calculated in a similar manner to the Elastic Coulomb sliding work given in Equation 3.26 to give

$$\begin{aligned} W_{sl} &= 4F_f^{lim}\left(x^{max} - x^{lim}\right) \\ &= \frac{8}{15}\mu C A_0 E^* R^{\frac{1}{2}}\left[z^{\frac{5}{2}} - \left(z - \frac{4G^* x^{lim}}{\mu E^*}\right)^{\frac{5}{2}}\right], \quad x^{max} > x^{lim} \end{aligned} \tag{3.38}$$

The work calculated by the microslip model for arbitrary displacement amplitude is therefore given by

$$W_f = \begin{cases} W_{ms}, & x^{max} \leq x^{lim} \\ W_{ms} + W_{sl}, & x^{max} > x^{lim} \end{cases} \tag{3.39}$$

Figure 3.14 shows the damping work predicted by the microslip model for a range of displacement amplitudes, together with the work contribution due to microslip and gross sliding. The graph shows a smooth continuous curve as the displacement is increased from the microslip range into gross sliding, giving a much more realistic representation of damping behaviour over such small displacement levels. The resulting damping ratios are plotted in Figure 3.15, showing that the damping ratio remains finite and continuous over the microslip-gross sliding range.

3.3.3 Implementation of Friction Models

The above friction models are implemented into the forced response analysis based on an FE modal approach for compatibility with the blade forced response methods. The strategy is to incorporate the flexibility of the friction surface into the blade mode shape, allowing the consideration of friction damping into the modal forced response calculation. For any given modal amplitude, the small-scale sliding displacements at the root-slot interface are obtained from the mode shape, allowing the damping work to be calculated over one vibratory cycle, which is subsequently used to calculate the equivalent viscous damping ratio.

The nonlinear force-displacement relationship is approximated in a linear fashion to allow the stiffness and damping effects of the friction interface to be separated, allowing an effective contact stiffness to be included in the modal analysis. The inclusion of contact sliding displacements into the modeshape is based on the assumption that that friction forces do not significantly change the modeshape for the light levels of damping commonly observed in practice. The assumption of linear contact stiffness is a good approximation for small displacements of the Elastic Coulomb and Microslip models, as shown in Figures 3.7 and 3.10. For Coulomb friction, the contact stiffness remains constant up to the slip limit, given by rearranging Equation 3.23 to give

$$k_t = \frac{\mu P_n A_0}{x^{lim}}. \tag{3.40}$$

Normal stiffness is taken as a factor of the tangential stiffness. This relationship has been discussed in the friction literature to be fairly reliable, with the stiffness ratio typically being around $\frac{k_n}{k_t} = 100$ for machined metal surfaces.

For the microslip model, the tangential stiffness varies with sliding displacement in a nonlinear manner, as shown in Figure 3.10, where the gradient reduces with displacement. The force-displacement curve is linearised by approximating the stiffness to a constant equivalent value. Since the absolute displacements are unknown in the modal analysis, the equivalent stiffness is calculated at a specified position along the microslip curve, as illustrated in Figure 3.16. The equivalent stiffness is therefore given by

$$k_t = \frac{\mu P_n A_0}{\gamma x^{lim}}. \tag{3.41}$$

Here, γ defines the position along the microslip curve relative to the slip limit (for example $\gamma = 0.5$ sets the displacement at half the slip displacement).

Normal stiffness is calculated based on the normal pressure and normal displacement, given by

$$k_n = \frac{P_n A_0}{z} \tag{3.42}$$

where z is the normal displacement obtained using Equation 3.32.

The equivalent normal and tangential contact stiffnesses are applied to the FE model by connecting each contact node on the root flank surfaces to ground via

three perpendicular spring elements in the planar and normal orientations. The modal analysis is then run to yield the contact modeshape over the flexible contact surfaces. For any given modal amplitude, the absolute displacement at each contact node is obtained by scaling the mode shape by the modal amplitude, allowing the friction forces to be determined.

The friction damping work done at each contact node over one vibratory cycle is calculated using Equation 3.19 for the Rigid Coulomb model, Equation 3.27 or Equation 3.39 for the microslip model. The work done at each node is summed over the blade root surface to give the total friction work and the equivalent viscous damping ratio is calculated from

$$\zeta_{fric} = \frac{W_{fric}}{2\pi\omega^2 q^2}. \tag{3.43}$$

The damping ratio provides a linearised equivalent of the friction damping effect and is only applicable for the modal amplitude given. Due to the nonlinear characteristics of friction, the work must be re-evaluated to provide the damping ratio for any different vibration amplitude.

Further discussion and implementation of the root friction modelling approach for an industrial compressor blade are provided in Chapter 8.

3.4 Figures

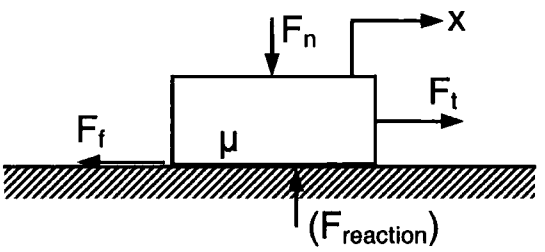

Figure 3.1: Brick representation of Rigid Coulomb friction model

Figure 3.2: Rigid Coulomb friction force for increasing displacement

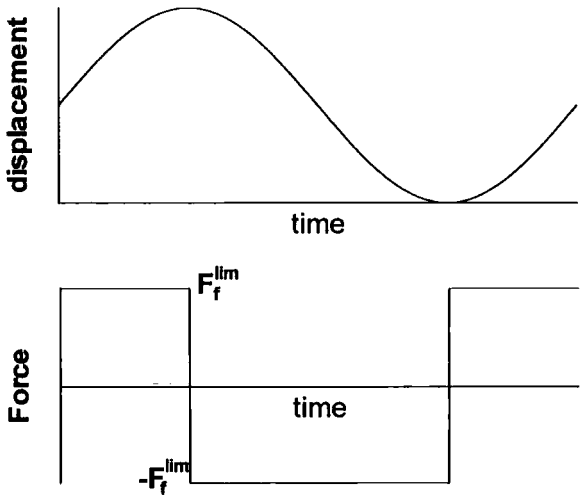

Figure 3.3: Rigid Coulomb friction force for sinusoidal displacement

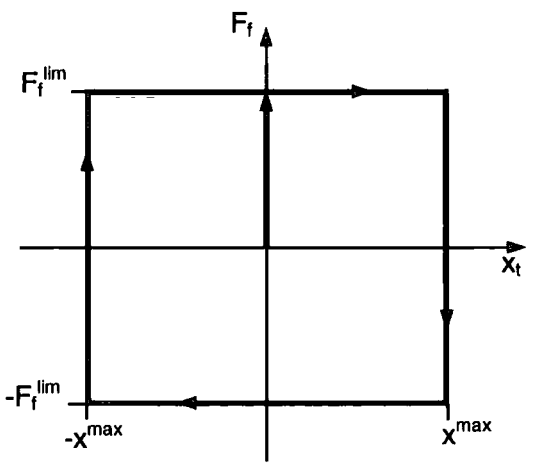

Figure 3.4: Rigid Coulomb hysteresis curve

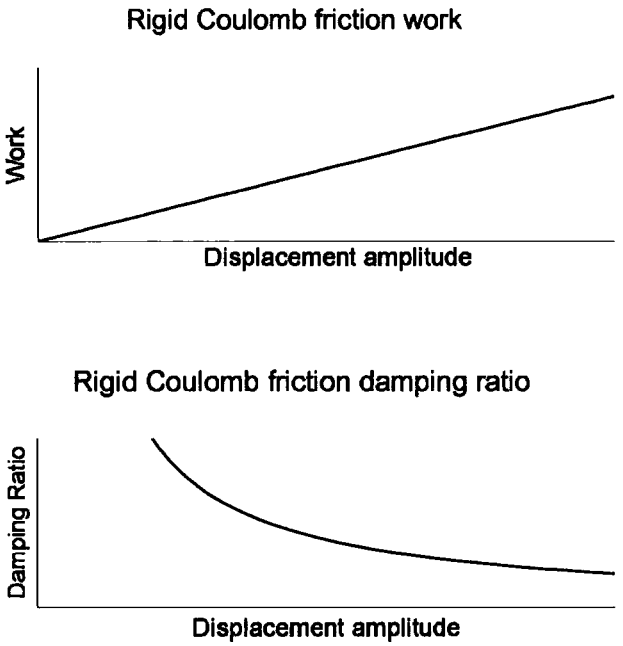

Figure 3.5: Variation of Rigid Coulomb friction work and damping ratio with displacement amplitude

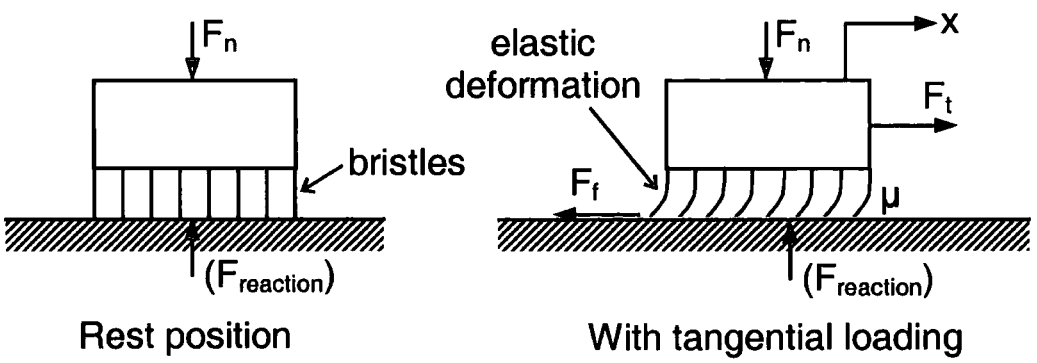

Figure 3.6: Brush representation of Elastic Coulomb friction model

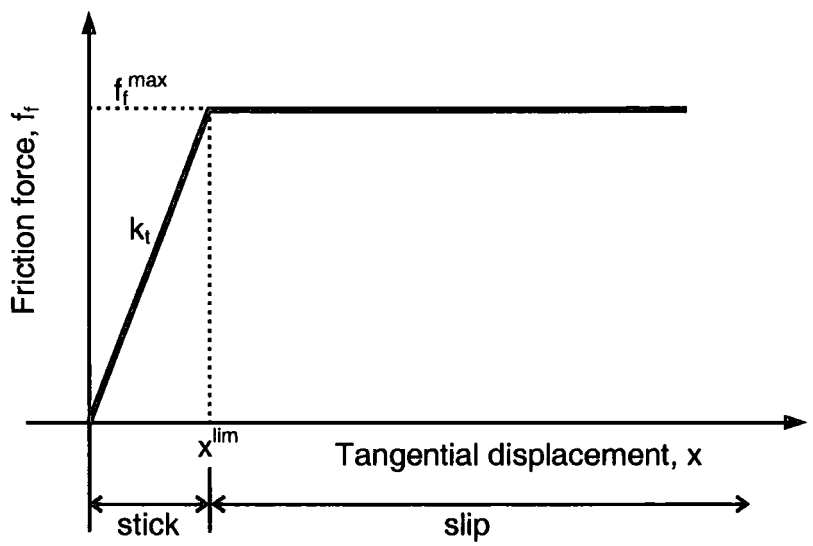

Figure 3.7: Elastic Coulomb friction force for increasing displacement

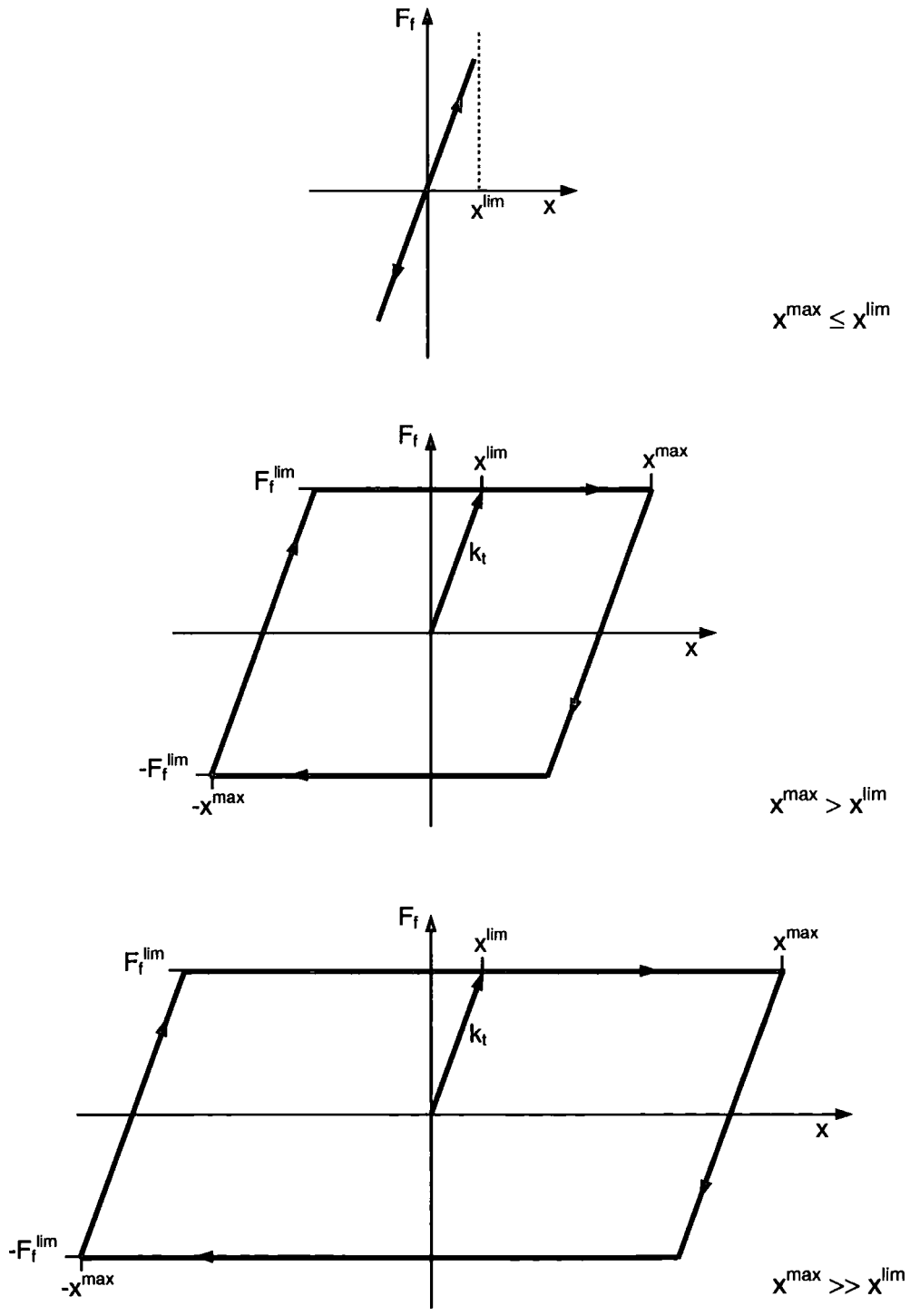

Figure 3.8: Elastic Coulomb hysteresis curves for various amplitudes of displacement

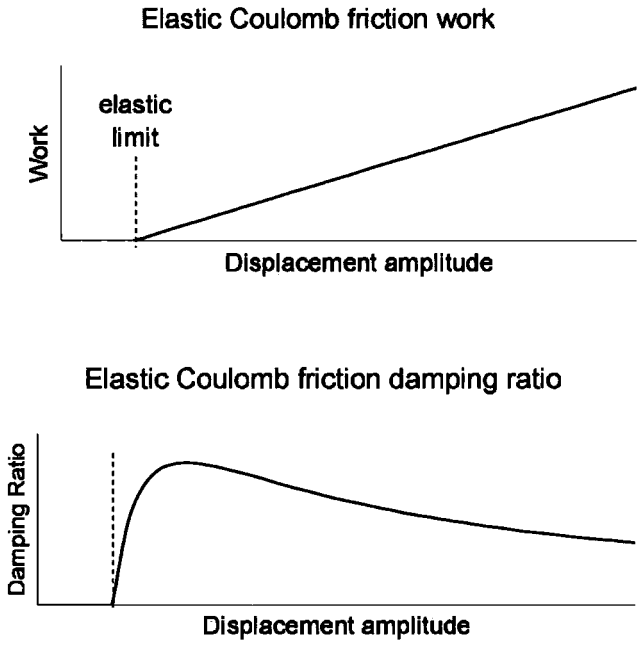

Figure 3.9: Variation of Elastic Coulomb friction work and damping ratio with displacement amplitude

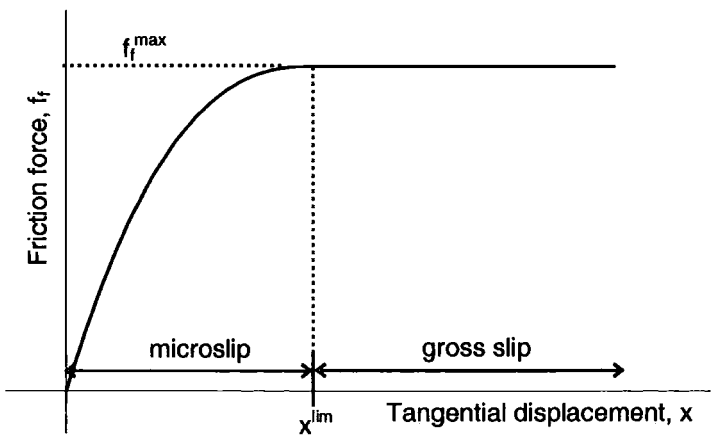

Figure 3.10: Microslip friction force during initial loading

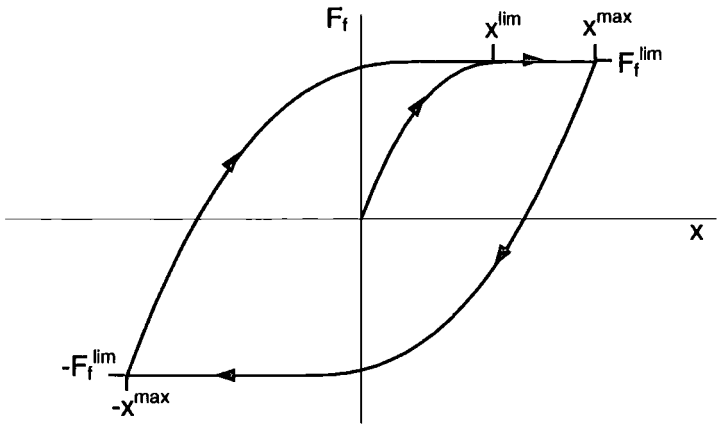

Figure 3.11: Microslip friction hysteresis curve

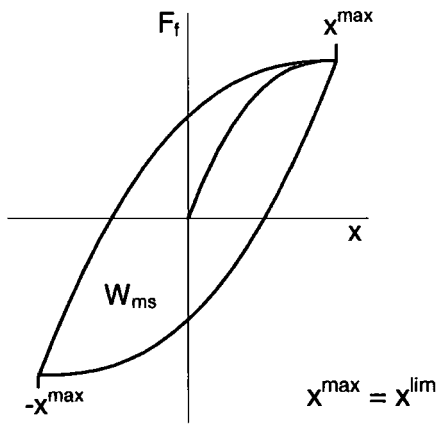

Figure 3.12: Microslip friction work at slip limit

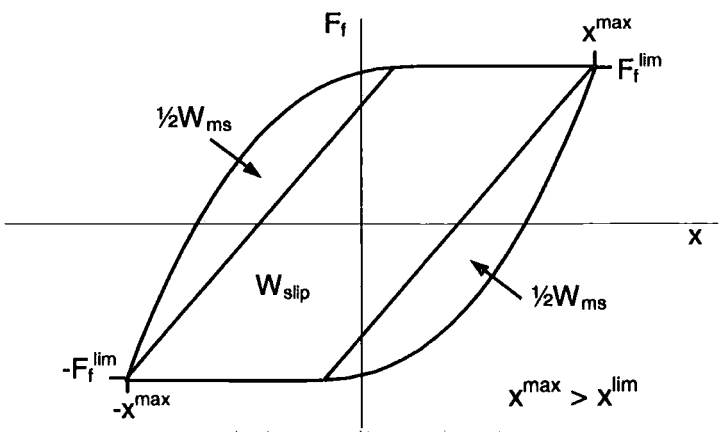

Figure 3.13: Graphical representation of microslip and sliding work

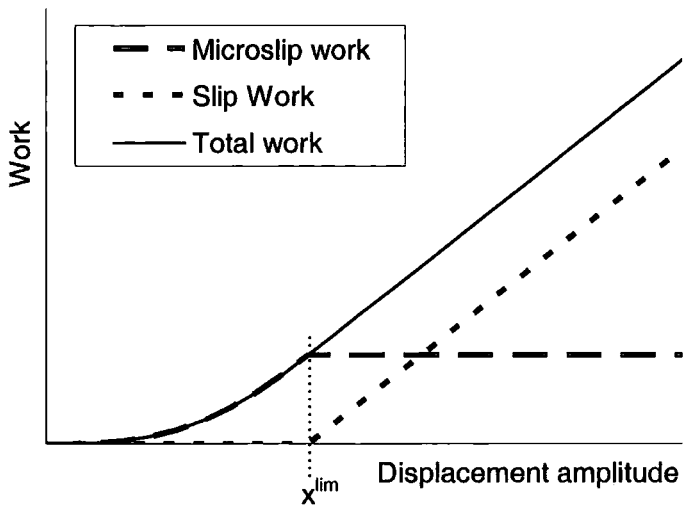

Figure 3.14: Friction work predicted by the microslip model

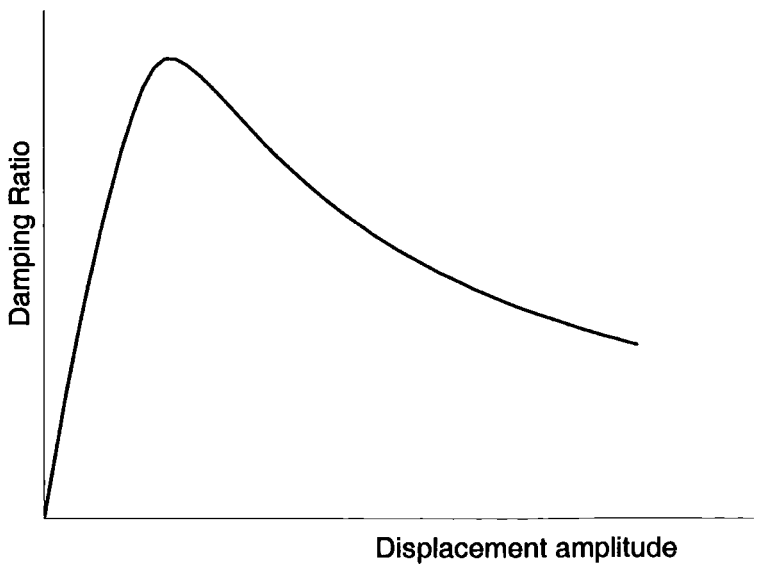

Figure 3.15: Variation in microslip damping ratio with displacement amplitude

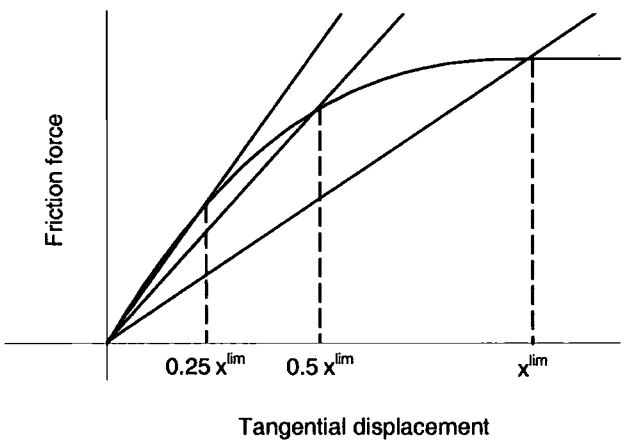

Figure 3.16: Calculation of tangential stiffness using various positions on microslip force curve

Chapter 4

Decoupled Forced Response System

4.1 Overview of Methodology

Linearised decoupled methods provide a highly efficient frequency domain approach for aeroelastic calculations. Fluid-structure interaction is dealt with in a loosely coupled linear manner, assuming that mode shapes and natural frequencies of the blade are not affected by aerodynamic loading. This assumption is valid for typical compressor blades, which are of high density and stiffness and vibrate with low amplitude. Efficient forced response methods based on the decoupled approach are usually preferred over time-accurate methods due to the relative simplicity of implementation, fast solution times and flexibility over choice of aerodynamic and structural methods.

The methodology of the decoupled approach is illustrated in Figure 4.1. This represents an open-loop system which requires only a single execution of the fluid and structural calculations. The resonant vibration of a single mode is calculated to give the steady-state blade vibration amplitude. Blade excitation is provided by unsteady aerodynamic forces of the corresponding harmonic and the system is subject to aerodynamic and structural damping. Blade modeshapes are obtained from an FE modal analysis, one of which is selected for analysis and interpolated onto the CFD mesh. The CFD analysis is simplified by decomposing the forcing

and damping calculations into two separate parts to yield the aerodynamic forcing function and the aerodynamic damping ratio. The forced response solution is then calculated using a modal approach for the given forcing and damping terms to give the resonant vibration amplitudes and stresses.

Finite Element Modal Analysis

Mode shapes and natural frequencies are provided by the modal analysis of a finite element model of the blade structure. The FE software used in the analysis was chosen to be Ansys, a typical commercial general-purpose package. The blade is modelled as a single isolated blade, fully constrained at the root and assuming no mechanical coupling between blades. Additionally, the method retains the capability of modelling a bladed disk based on cyclic symmetry, where the complex modeshape of a single blade segment is used. The stress stiffening effect of centrifugal loading is accounted for by performing a preliminary static analysis at the specified engine speed. Although less significant, steady fluid loading can be included in the static analysis if desired by approximating the steady fluid pressures as a small series of spanwise equivalent forces on the FE model. The result of the pre-stressing calculation is a modification to the system stiffness matrix used in the modal analysis.

The result of the modal analysis is a set of real mode eigenvectors, such that the modal response of every point of the blade moves in phase, with relative amplitude determined by the mode shape. If the blade is visualised to be repeated around the annulus to represent the entire disc, then the modal response of each blade will be seen to vibrate with a discrete interblade phase angle between neighbouring blades. Whilst this approach is commonly accepted in the literature for unshrouded blades, the decoupled approach is also capable of dealing with the analysis of shrouded bladed disc assemblies utilising cyclic symmetry in the modal analysis. In this case, a set of complex modes for the disc sector mode will result, representing a continuous travelling wave of blade motion around the disc.

A single mode for investigation is selected from the set at the resonant crossing point of interest on the Campbell diagram, dictating the mode, frequency and engine speed. The modeshape is subsequently interpolated onto the CFD mesh as a distri-

bution of real modeshape amplitudes over the aerofoil surfaces. The aerodynamic boundary conditions are obtained from the performance map of the machine.

Aerodynamic Forcing

The unsteady aerodynamic excitation forces are obtained from either a single or multi-stage CFD calculation which models the flow disturbances due to inlet distortion or bladerow interaction. The forcing analysis is done with non-vibrating blades to yield the unsteady harmonic pressure distribution over the blade surfaces due to incoming flow disturbances. The unsteady pressure harmonic at the blade natural frequency is integrated over the blade surfaces to provide the complex modal excitation force. Forcing harmonics outside the natural frequency are assumed to have an insignificant effect on the steady-state resonant response and are neglected. The formulation of the modal excitation force is given later in Section 4.3.

Aerodynamic Damping

Aerodynamic damping is calculated based on the assumption that vibration-induced pressures increase linearly with vibration amplitude. Whilst linear aerodynamic damping behaviour for two transonic fan rotors has been observed by Li and He [74] and Schmitt et al. [75], no evidence has yet been reported showing significant non-linear damping for high frequency forced response cases with small blade deformation. The CFD damping calculation is performed on an isolated bladerow in clean flow with the blade vibrating in the mode at the blade natural frequency. The amplitude of vibration is specified at a realistic level and the interblade phase angle is determined by the wavelength of the aerodynamic disturbance. The induced harmonic forces resulting from the blade vibrating in the fluid are calculated to give the pressure distribution at the vibration harmonic. The harmonic pressures and blade displacements are integrated over the blade surfaces to provide the work done on the fluid by the blade over one vibratory cycle. An equivalent aerodynamic modal damping ratio is then calculated from the work, based on the principle of equivalent viscous damping. The formulation for the aerodynamic damping calculation is provided in Section 4.3.

Forced Response Solution

Once the aerodynamic forcing and damping terms are known, the forced response is calculated very efficiently using a single DoF equation based on the CFD mesh. Linear mechanical damping is included as a prescribed damping ratio, based on the principal of equivalent viscous damping. Two methods of obtaining the forced response solution are used: 1) the modal equation method; and 2) a new energy method. The modal reduction method is the standard approach, involving the transformation of physical variables into modal space before solving the modal equation. The resulting modal amplitude is then expanded into physical space to give the actual blade response. The energy method provides an alternative forced response solution to the modal equation method and performs the calculations directly on the CFD mesh using actual vibratory displacements. Here, the mode shape is directly scaled to balance destabilising and stabilising work due to forcing and damping to provide the blade motion at equilibrium.

4.2 FE-CFD Mesh Interface

4.2.1 Problem Description

The modal displacements from the FE modal analysis are interpolated from the FE mesh to the CFD mesh to allow the aerodynamic modal forcing to be calculated using the fluid pressures on the CFD mesh. The calculation of modal forcing on the CFD mesh requires only a single interpolation process for each mode under consideration, providing an efficient forced response process. The alternative to this approach would be to interpolate fluid pressures onto the FE mesh, where the modal forcing would be calculated. The disadvantage of this alternative would be that fluid pressures would need to be transferred to the FE mesh every time the CFD solver is employed for the forcing and damping calculations. The calculation of modal forcing on the CFD mesh is therefore a much simpler approach.

The FE-CFD interface is a major component of the forced response prediction system, which must accurately interpolate the mode shape from the Ansys FE mesh to the CFD mesh. The interface must be capable of interpolating with high accuracy, whilst being robust enough to deal with the demands of industrial use. A large part of the problem is due to the unstructured nature of FE meshes and the need to facilitate the use of different structural element shapes. Whereas FE meshes may take on the appearance of structured meshes, looking similar to structured CFD meshes, the mesh data in Ansys is stored in an unstructured manner.

Further complications arise due to likelihood of slight variations between the mesh geometries, resulting in non-coincident boundary surfaces of the two meshes. The primary cause of this issue is due to the blade *unrunning* of the FE mesh, where structural analysts "undo" the effects of centrifugal, static gas and temperature loading of the blade to give the *cold* blade geometry. The cold shape is usually used for subsequent structural analysis, leading to a significant difference in geometry if the static deformation is not reapplied to the blade shape. The magnitude of this difference at the tip can be of similar size to the blade thickness. Secondary differences in geometry are due to the planar nature of the element surfaces, which do not conform exactly to the curved blade profile. Since the FE and CFD meshes

are not identical, the nodes of one mesh will not necessarily intersect the planar surfaces of the other mesh. Such differences are relatively small, but the implication on interpolation accuracy can be significant for low density meshes.

4.2.2 Metholology

A method of interpolation was developed to transfer the mode shape from an unstructured FE mesh comprising of tetrahedral, hexahedral, prismatic and wedge elements to a CFD structured mesh, based on the assumption of noncoincident mesh boundary surfaces. The harmonic amplitudes of the mode shape are transferred to the CFD mesh by 2D linear interpolation over the 3D FE mesh surface. For each point on the CFD mesh boundary surface, a plane on the FE mesh boundary is chosen. The plane is defined by three corner FE nodes on an external element face, giving a single plane per triangular face and a selection of four planes per rectangular face, as shown in Figure 4.2. Forming a triangle, the three nodes are selected to provide the closest centroid to the CFD point, thus defining the best interpolation plane to provide maximum accuracy.

Interpolation of the mode shape components is performed at the orthogonal projection of the CFD point onto the plane, as shown in Figure 4.3. The mode shape data for the CFD point is taken at the projection point in order to minimise errors caused by the mesh surfaces not coinciding. Methods of 3D interpolation are expected to reduce accuracy by introducing errors for non-coincident surfaces.

Misalignment of the FE and CFD meshes is common due to differences in coordinate systems, origins and orientation between the two meshes. Axial and rotational alignment of the FE mesh to the CFD mesh is incorporated based on the specification of reference nodes. The tip leading edge is normally taken as the reference point, as it is often the most flexible part of the aerofoil with the highest strain gradients, where interpolation accuracy is the most important.

At positions where the aero point lies close to an element-element boundary, noise in the interpolated values can be seen due to the step change in plane orientation from one element face to another. This effect is particularly noticeable in low-density meshes or in areas of high modeshape gradients. The interpolation quality

is improved by averaging the interpolated data over the two adjacent elements if the interpolation point lies within a specified proximity to an element-element boundary.

An additional source of error occurs when interpolation planes are not aligned with the pressure and suction surfaces, such as the tip, leading and trailing edges of typical, blunted FE meshes. Such surfaces lie normal to the desired interpolation planes and can cause significant interpolation errors for low density FE meshes around these regions. The errors are avoided by specifying the element and face numbers on the FE mesh and preventing these surfaces from being used to define interpolation planes. Fortunately, this edge effect does not provide concern for high-density meshes and can be neglected.

CFD meshes incorporating tip clearance cells require further attention to define the blade motion of the clearance cells above the blade tip. Since these cells lie outside the FE mesh geometry, the axial and tangential mode shape components are set equal to those at the tip. In order to prevent penetration of the blade mesh into the casing, radial motion at the tip is linearly reduced through the clearance cells to zero at the casing.

4.2.3 Mathematical Formulation

Orthogonal Projection onto Surface

As described above every combination of three adjacent FE mesh nodes is considered to define the interpolation points used for each surface CFD grid point. The actual three nodes chosen create a triangle with the closest centroid to the CFD point, provided that the face is valid for interpolation. With the three points defining a plane, 2D interpolation is performed at the orthogonal projection of the CFD point on the plane to allow for small deviations of the CFD mesh surface from the FE mesh surface.

Figure 4.4 shows three FE nodes A, B and C, defined relative to a global origin by the position vectors $\vec{a}$, $\vec{b}$ and $\vec{c}$. The vectors of B and C relative to C are defined as $\vec{AB}$ and $\vec{AC}$. A vector $\vec{n}$ normal to the ABC plane is obtained from the cross

product

$$\vec{n} = \vec{AB} \times \vec{AC} \tag{4.1}$$

The equation of the plane is therefore given by

$$\vec{r} \cdot \vec{n} = \lambda \tag{4.2}$$

where $\vec{r}$ is the position vector of an arbitrary point on the plane. The scalar λ is obtained from

$$\lambda = \vec{a} \cdot \vec{n} \tag{4.3}$$

Considering a point D positioned outside of the ABC plane, the orthogonal projection of the point onto the plane defines a single point, E, such that the vector $\vec{DE}$ is orthogonal to the plane. The parallel alignment of $\vec{DE}$ with the normal vector $\vec{n}$ gives the relationship

$$\vec{DE} = t\vec{n} \tag{4.4}$$

which is rewritten in the form

$$\vec{e} = \vec{d} + t\vec{n} \tag{4.5}$$

Substituting $\vec{e}$ into the plane equation (4.2) gives

$$\left(\vec{d} + t\vec{n}\right) \cdot \vec{n} = \lambda \tag{4.6}$$

which is expanded and rearranged to give

$$t = \frac{\lambda - \left(\vec{d} \cdot \vec{n}\right)}{|\vec{n}|^2} \tag{4.7}$$

Substituting t into Equation 4.5 gives the orthogonal projection of the CFD point, D, onto the plane, given by

$$\vec{e} = \vec{d} + \left(\frac{\lambda - \left(\vec{d} \cdot \vec{n}\right)}{|\vec{n}|^2}\right)\vec{n} \tag{4.8}$$

Transformation into Local Coordinate System

Before interpolation takes place, the four planar points A,B,C and E are transformed from the global X,Y,Z axes into a local i,j coordinate system. Figure 4.5 shows the four points on the local i,j axis, together with the field variable ϕ. The origin is taken at point A and the i-axis is aligned with the vector $\vec{AB}$, where the the unit vector of the i-axis is defined in 3D space by

$$\hat{i} = \frac{\vec{AB}}{|\ \vec{AB}\ |} \tag{4.9}$$

The j-axis lies orthogonal to both the i-axis and the plane normal defined as

$$\hat{j} = \frac{\vec{n} \times \hat{i}}{|\ \vec{n} \times \hat{i}\ |} \tag{4.10}$$

Points C and E are defined in the local 2D axes by taking the projection of each point in the direction of each axis. The local 2D coordinates of each of the four points is therefore given by

$$\begin{aligned} A_{ij} &= (0,0) \\ B_{ij} &= \left(|\ \vec{AB}\ |, 0\right) \\ C_{ij} &= \left((\vec{AC} \cdot \hat{i}), (\vec{AC} \cdot \hat{j})\right) \\ E_{ij} &= \left((\vec{AE} \cdot \hat{i}), (\vec{AE} \cdot \hat{j})\right) \end{aligned} \tag{4.11}$$

Interpolation Function

The linear interpolation function is calculated using the shape function of a 2D simplex triangular finite element based on an identical formulation to the ANSYS element, which can be found in the ANSYS literature. The three modeshape DoFs are interpolated using three individual interpolation functions where the linear interpolation function for a single field value is given by

$$\phi = \alpha_1 + \alpha_2 i + \alpha_3 j \tag{4.12}$$

The α_1, α_2 and α_3 parameters are calculated using the field values ϕ known at

the positions of the three FE nodes A, B and C from the expressions

$$\begin{aligned}\alpha_1 &= (s_A\phi_A + s_B\phi_B + s_C\phi_C)/2A \\ \alpha_2 &= (t_A\phi_A + t_B\phi_B + t_C\phi_C)/2A \\ \alpha_3 &= (u_A\phi_A + u_B\phi_B + u_C\phi_C)/2A\end{aligned} \tag{4.13}$$

where A is the area of the triangle ABC given by

$$A = \frac{i_b j_c}{2} \tag{4.14}$$

and the coefficients s, t and u are given by

$$\begin{aligned}s_A &= i_B j_c \\ s_B &= i_C j_A - i_A j_C \\ s_C &= i_A j_B - i_B j_A\end{aligned}$$

$$\begin{aligned}t_A &= j_B - j_C \\ t_B &= j_C - j_A \\ t_C &= j_A - j_B\end{aligned} \tag{4.15}$$

$$\begin{aligned}u_A &= i_C - i_B \\ u_C &= i_A - i_C \\ u_C &= i_B - i_A\end{aligned}$$

Once α_1, α_2 and α_3 are known, the mode shape component ϕ is interpolated at position E by solving Equation 4.12.

4.3 Modal Equation Method

The modal equation method is based on the single-DoF modal equation outlined in Section 3.2.2, where the forced response is obtained from the analytical solution of the modal equation in the frequency domain.

Modal forcing is calculated on the CFD mesh, which avoids the need to interpolate fluid pressures from the CFD mesh to the FE mesh for each modal force calculation. The modal force calculation is done using the modal displacements on the CFD mesh which are interpolated only once from the FE mesh to the CFD mesh in the manner described in Section 4.2.

The aerodynamic modal force is considered in terms of Lagrangian mechanics to be the virtual work done by the fluid integrated over the blade surface. The amplitude of translational displacement for each CFD mesh node on the blade surface is defined in the axial, radial and azimuthal directions, which are combined in a single vector $\{x_{cfd}\}$ to provide all the nodal degrees of freedom of blade displacement. Each nodal DoF is denoted by the index, j, giving a total, n, equal to three times the number of surface nodes.

The vector of aerodynamic force amplitudes acting on the nodal DoFs is defined as $\{\tilde{F}\}$, where the force amplitude acting on each individual DoF is given by

$$\tilde{F}_j = A_j \tilde{P}_j \tag{4.16}$$

Here, the force acting in the direction of the nodal DoF, j, is the product of the fluid pressure, $\tilde{P}_j$, at the surface position of DoF j and A_j is the projection of the effective nodal surface area in the direction of the DoF. The effective nodal surface area is a summation of a proportion of the areas of neighboring surface cells.

The mesh displacements in each DoF are related to the mode shape in the same manner as in Equation 3.9 to give

$$\{x_{cfd}\} = q_{cfd}\{\phi_{cfd}\} \tag{4.17}$$

for the single mode in question on the CFD mesh. The aerodynamic modal force is then obtained from the summation of the virtual work done by the fluid at each nodal DoF on the CFD mesh surface, given by

$$\tilde{f} = \{\phi_{cfd}\}^{\mathrm{T}} \left\{\tilde{F}\right\} \tag{4.18}$$

Considering the aerodynamic forces in terms of their real and imaginary components, the modal force expression is written as

$$\tilde{f} = \sum_{j=1}^{n} \left\{(\phi_{cfd})_j \ \left(F_j^{\Re} + \mathrm{i}F_j^{\Im}\right)\right\} \tag{4.19}$$

The aerodynamic damping ratio ζ_{aero} is calculated from the work done on the blade by the fluid, obtained from the CFD damping calculation. Work is calculated in physical terms by integrating the aerodynamic damping force distribution and blade displacements over one vibratory cycle, using

$$W_d^{cfd} = \pi \sum_{j=1}^{n} \left(D_j^{\Im} x_j^{\Re} - D_j^{\Re} x_j^{\Im}\right)^{cfd} \tag{4.20}$$

where $D^{\Re}$ and $D^{\Im}$ are the complex components of the physical damping force vector $\tilde{D}$ and $x^{\Re}$ and $x^{\Im}$ are the complex components of the blade displacement vector $\tilde{x}$.

However, if the blade motion in the damping calculation is specified to be entirely real with zero imaginary component, the above work expression is reduced to

$$W_d^{cfd} = \pi \sum_{j=1}^{n} \left(D_j^{\Im} x_j\right)^{cfd} \tag{4.21}$$

Alternatively, if the modal damping force $\tilde{d}$ is known, the work can be calculated in modal space using

$$W_d^{cfd} = \pi \left(d^{\Im} q^{\Re}\right)^{cfd} \tag{4.22}$$

Values relating to the CFD damping calculation are based on the specified vibration amplitude x^{cfd}, and are denoted by the superscript ^{cfd}. The aerodynamic damping ratio is calculated from the work based on the principle of equivalent viscous damping,

$$\zeta_{aero} = \frac{-W_d^{cfd}}{2\pi\omega_i^2 \left(q^{cfd}\right)^2} \tag{4.23}$$

The modal amplitude of the CFD damping calculation is simply given by the ratio between the CFD blade motion x^{cfd} and the mass-normalised mode shape, ϕ,

$$q^{cfd} = \frac{x^{cfd}}{\phi} \tag{4.24}$$

Mechanical damping, ζ_{mech}, can be estimated or calculated separately and is added to the aerodynamic damping to give total system damping ζ_{tot}.

The modal equation (Equation 3.12) is analytically solved in the frequency domain to provide the solution of the modal equation for excitation at arbitrary frequency, ω, given by

$$|q| = \frac{|f|}{\sqrt{\left(\omega_i^2 - \omega^2\right)^2 + \left(2\zeta_{tot}\omega_i\omega\right)^2}} \tag{4.25}$$

Since resonant vibration with excitation at the blade natural frequency, $\omega = \omega_i$, is only considered, the analytical solution to the modal equation reduces to,

$$|q^{fr}| = \frac{|f|}{2\omega_i^2\zeta_{tot}} \tag{4.26}$$

yielding the magnitude of the modal amplitude of the forced response solution. The resulting modal amplitude is then used to scale the modeshape by

$$\{|x^{fr}|\} = |q^{fr}|\{\phi\}, \tag{4.27}$$

transforming the modal amplitude into the physical response amplitudes of the blade. Blade stresses and strains can be obtained in a similar manner, where modal values from the FE mesh are scaled by the modal amplitude.

4.4 Energy Method

The energy method is a simple approach to obtaining the forced response solution that requires less knowledge of structural dynamics than modal reduction method. It eliminates the use of modal reduction theory for purely aeroelastic forced response calculations. The method is based on an energy balance applied directly on the CFD mesh in physical space. The major benefit of this approach is that the scale of the mass-normalised mode shape is not required for the CFD calculations, therefore eliminating a potential practical issue. Instead, modeshapes can be scaled freely, disregarding original modeshape scales and units, allowing modeshape files to be passed freely between analysts and designers with minimal communication about how the modeshapes were created.

Considering a system undergoing forced vibration in terms of work transfer, steady-state vibration occurs at the amplitude where the forcing work (destabilising) applied to the blade per cycle balances the dissipated damping work (stabilising). Based on a linear increase of forcing work with vibration amplitude and a quadratic increase of damping work, a single point of equilibrium can be found, giving the forced response solution, as shown in Figure 4.6. Firstly, forcing work and damping work are calculated at a specified amplitude of vibration, then the work values are scaled to achieve equilibrium to provide the vibration amplitude at the point of steady-state forced vibration.

The calculation of the damping work is the most straightforward task, knowing that the relative phase between the blade motion and damping forces remains constant for a given vibration amplitude. The damping work is simply taken as the value given by the CFD damping calculation using Equation 4.21.

Forcing work is calculated knowing that: 1) aerodynamic excitation forces remain fixed and are not affected by blade motion; and 2) the vibration will lag the force distribution with the phase providing the *maximum destabilising effect.* For example, the response of a simple spring-mass system undergoing resonant forced vibration will lag the excitation force by exactly 90°. In other words, the blade motion lags the forcing by the angle providing the maximum work to the blade. Similarly, for a multi-DoF system undergoing resonance from an excitation force distribution, the modeshape lags the forces by the phase angle providing the maximum work. However, since individual forces in the distribution may be out of phase with one-another, no datum forcing phase is defined, so the response phase can not be defined by a 90° lag. Instead, the response phase is defined at the angle providing the maximum forcing work. As illustrated in Figure 4.7, the forcing work follows a sinusoidal variation with vibration phase. A simple iterative approach calculates the work done on the blade at discrete angles varying between 0 and 2π to obtain the work done for all possible phase angles. The forcing work is simply taken to be the maximum value.

Once the aerodynamic forcing and damping work is known, the point of equilibrium at the amplitude of steady-state vibration is found by scaling the linear forcing

term and quadratic damping term to yield the forced response solution. Firstly aerodynamic forcing work, W_f, and aerodynamic damping work, W_{ad}, over one cycle are expressed as functions of modal amplitude, where forcing work is linearly proportional to modal amplitude and damping work is proportional to the square of modal amplitude. Representing the relationships using constant coefficients β_f and β_{ad} for the forcing and damping terms respectively, gives

$$W_f = \beta_f q; \;\; W_{ad} = \beta_{ad} q^2.$$

However, all work calculations are initially based on the scale of the blade motion used in the CFD damping calculation, where $\{x^{cfd}\}$ is the displacement amplitude vector of the CFD mesh. Any value corresponding to this vibration scale is denoted by the superscript ^{cfd}, and the above work expressions are written as

$$W_f^{cfd} = \beta_f q^{cfd}; \;\; W_{ad}^{cfd} = \beta_{ad} \left(q^{cfd}\right)^2.$$

Secondly, mechanical damping is included as

$$W_{md}^{cfd} = \beta_{md} \left(q^{cfd}\right)^2,$$

where the work is calculated from the structural damping ratio , ζ_{mech}, at the same modal amplitude by

$$W_{md}^{cfd} = 2\pi\zeta_{mech}\, \omega^2 \left(q^{cfd}\right)^2.$$

If the actual value of q^{cfd} is unknown at this stage, it can be calculated by comparing the blade motion of the CFD mesh in the damping calculation to the original mass-normalised eigenvector for any DoF, j, of the blade using

$$q^{cfd} = \frac{x_j^{cfd}}{\phi_j}.$$

The work coefficients, β_f, β_{ad} and β_{md} can be used to determine the work at arbitrary vibration amplitude, in particular, the equilibrium amplitude, q^{eq}, of the forced response solution;

$$\beta_f = \frac{W_f^{cfd}}{q^{cfd}} = \frac{W_f^{eq}}{q^{eq}}, \;\; \beta_{ad} = \frac{W_{ad}^{cfd}}{\left(q^{cfd}\right)^2} = \frac{W_{ad}^{eq}}{\left(q^{eq}\right)^2}, \;\; \beta_{md} = \frac{W_{md}^{cfd}}{\left(q^{cfd}\right)^2} = \frac{W_{md}^{eq}}{\left(q^{eq}\right)^2}. \tag{4.28}$$

The forcing and damping work is then scaled to find the point of equilibrium, where destabilising work input equals stabilising work dissipated, given by

$$-W_f^{eq} = W_{ad}^{eq} + W_{md}^{eq},$$

or in terms of vibration amplitude by substituting the relationships from Equation 4.28,

$$-\beta_f \, q^{eq} = \beta_{ad} \left(q^{eq}\right)^2 + \beta_{md} \left(q^{eq}\right)^2 .$$

Factorising for q^{eq} and substituting β terms for the expressions of the known values of work (Equation 4.28) gives

$$-\frac{W_f^{cfd}}{q^{cfd}} = \left(\frac{W_{ad}^{cfd}}{\left(q^{cfd}\right)^2} + \frac{W_{md}^{cfd}}{\left(q^{cfd}\right)^2} \right) q^{eq},$$

when rearranged gives

$$q^{eq} = \left(\frac{-W_f^{cfd}}{W_{ad}^{cfd} + W_{md}^{cfd}} \right) q^{cfd} \tag{4.29}$$

Expressing the equilibrium blade motion as

$$\left\{x^{eq}\right\} = \frac{q^{eq}}{q^{cfd}} \left\{x^{cfd}\right\}$$

allows the equilibrium modal amplitude to be eliminated from the above expression, where the energy balance equation expressed in terms of work, i.e.

$$\left\{x^{eq}\right\} = \left(\frac{-W_f^{cfd}}{W_{ad}^{cfd} + W_{md}^{cfd}} \right) \left\{x^{cfd}\right\} \tag{4.30}$$

Here, the actual blade motion of the CFD mesh used in the damping calculation is scaled to yield the harmonic amplitudes of the response solution. If mechanical damping is neglected, the calculation requires no knowledge of the eigenvector scale. Where mechanical damping is included, the eigenvector scale is needed but the method still avoids the use of modal algebra, providing a useful alternative to the modal equation method.

4.5 Figures

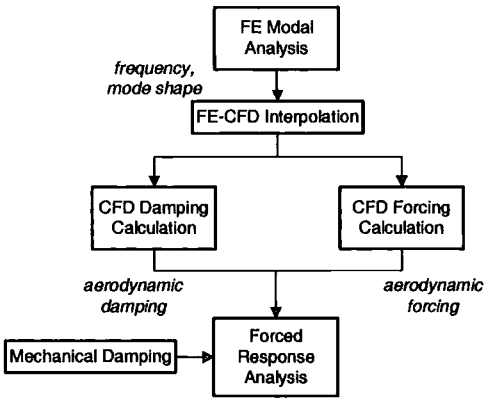

Figure 4.1: Decoupled forced response system

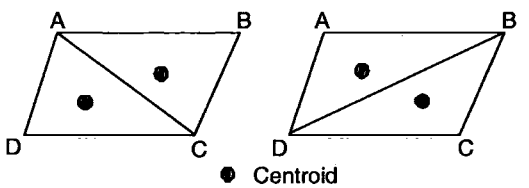

Figure 4.2: Possible interpolation planes for a rectangular FE element face

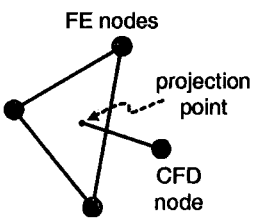

Figure 4.3: 2D interpolation at projection onto FE mesh surface

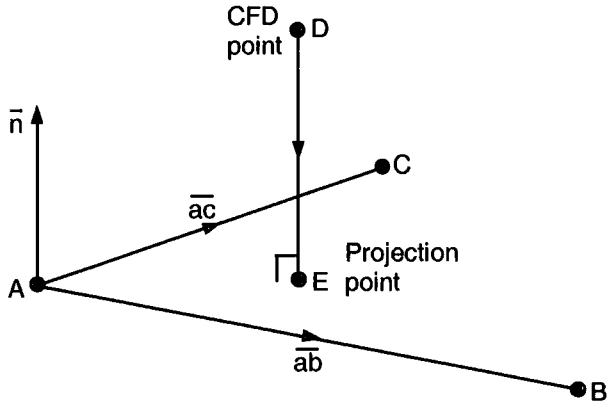

Figure 4.4: Calculation of orthogonal projection point

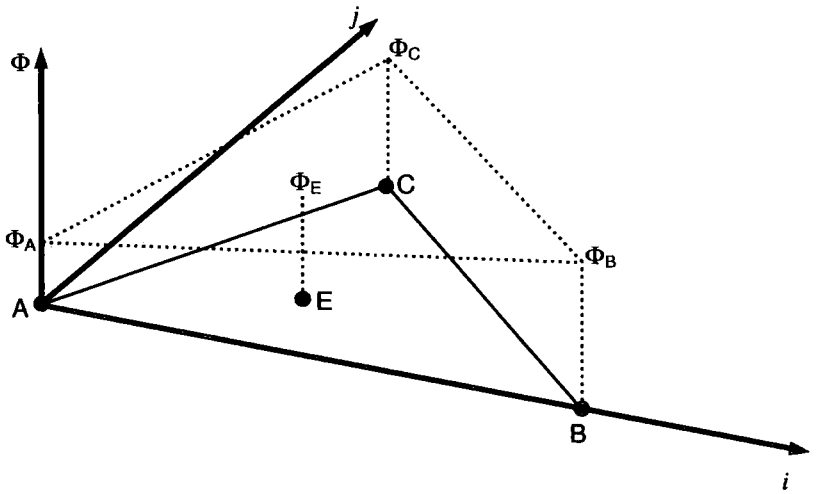

Figure 4.5: Transformation of interpolation points into local 2D geometrical axis system

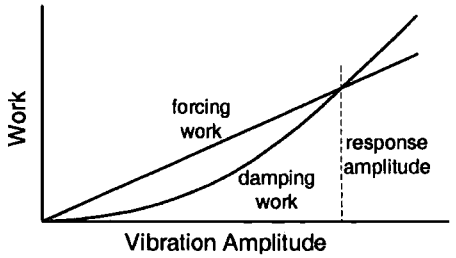

Figure 4.6: Equilibrium of forcing and damping work

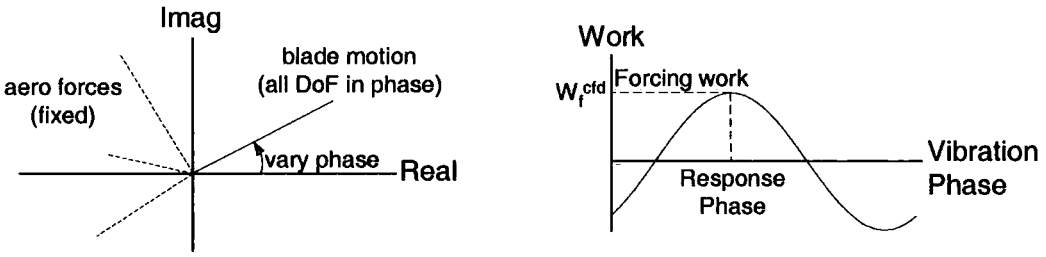

Figure 4.7: Response phase for maximum forcing work

Chapter 5

Verification of the Decoupled System

5.1 Introduction

The NASA Rotor 67 transonic fan rotor was used as the preliminary case study during the development of the components of the forced response system. The rotor provides a relatively simple case to demonstrate the forced response methodologies, involving only a single bladerow calculation. Four modes are considered in separate forced response analyses to demonstrate the implementation of the decoupled method and provide a basis for further investigation of alternative fluid-structure coupling strategies.

The system is evaluated for a challenging industrial study of a Siemens 3-stage transonic test compressor, where the forced response predictions of three high frequency crossing points on the Campbell diagram are compared with strain gauge test data. This case offers a good benchmark for the forced response system, providing many of the difficulties encountered in an industrial environment, whilst allowing the validation of predictions against engine test data. This case study has been done in cooperation with Siemens, who assisted in the analysis and provided test data.

5.2 NASA Rotor 67 Transonic Fan

5.2.1 Case Description

The NASA Rotor 67 transonic fan is typical of modern low-aspect ratio transonic fan design and consists of 22 unshrouded blades of $93mm$ chord length at tip. The details of the rotor aerodynamics are available in the public domain and there have been several published studies on its unsteady aerodynamic and aeromechanical performance. Publications on the aeromechanical analysis of NASA Rotor 67 have included the flutter calculations of Marshall and Imregun [5] and Srivastava et al. [147] based on time-accurate CFD codes. The fan is designed to produce a total pressure ratio of 1.63 for a mass flow rate of 32.25 kg/sec with a tip inlet relative Mach number of 1.38 at the design point of speed $16,043$ rpm.

For each of the four resonant operating conditions investigated, blade excitation is provided by hypothetical inlet distortions to simulate inlet flow conditions typically encountered in inlet distortion and bladerow interaction problems. The number of nodal diameters of the distortions are chosen to provide excitation for each mode at crossing points close to 100% design speed. The aim is to provide forced response calculations for a fairly wide range of resonant conditions from the fundamental modes typical of inlet distortion cases, to a high frequency mode typical of bladerow interaction problems. The crossing points of the 1^{st} and 2^{nd} bending, 1^{st} torsion and the 7^{th} modes with the 2^{nd}, 5^{th}, 7^{th} and 15^{th} excitation orders, respectively, are investigated. To illustrate the physical representation of this case study, the rotor geometry with a 2-node inlet flow distortion pattern is shown in Figure 5.1.

Structural Modelling

Due to the fact that only aerodynamic data was available, the FE mesh was constructed based on the geometry of the CFD mesh, giving a model comprising of 806 quadratic 20-node brick elements. The FE and CFD meshes can be seen later in this section in Figure 5.4. Since the geometry of the blade root was not known, the blade was modelled as an aerofoil cantilevered at the hub. The material properties of the blade were not known and typical properties for titanium were assumed (density,

4110 kg/m^3; Young's modulus of elasticity, 125 GPa, Poisson's ratio, 0.27).

The stress stiffening effect of the centrifugal loading is incorporated based on a static analysis at 100% speed. For simplicity, the influence of steady gas loads on the modal solution are assumed to be negligible. The blade static twisting effect did not need to be included since the FE mesh already conformed to the hot running shape of the CFD mesh.

CFD Modelling

The fluid H-mesh consisting of 110x25x29 results in a single-passage 3-D computational domain of approximately 73k cells, on which the linearised Navier-Stokes equations are solved in the frequency domain. A blade-blade view of the mesh can be seen in Figure 5.5 and a portion of the mesh over the blade surface is shown in Figure 5.4. For reasons of convenience, the blade count is modified from 22 to 21 in order to verify results against the previous work of Li and He [74]. Since a single passage approach is used in the CFD analysis, no computational benefits are gained from this change.

Flow conditions are taken close to the design load and the strength of the inlet distortion is specified by perturbing the steady flow solution at the inlet plane. Once the steady solution is achieved, a perturbation of the axial velocity at the inlet plane is prescribed. Assuming that all other flow conditions remain unchanged, the density is adjusted accordingly to ensure constant static pressure at the inlet. The strength of the axial velocity perturbation is set such that the relative dynamic head perturbation at inlet is at a realistic level of approximately 10%. The forcing calculation is performed through a single passage of non-vibrating blades subject to the prescribed inlet distortion to yield the resulting unsteady pressure distribution over the blade surfaces caused by the incoming flow disturbances.

The damping calculation is carried out with vibration in the specified modes, with the modeshapes scaled to provide a leading edge tip deflection equal to 1% blade chord. In each damping calculation, the blade is set to oscillate with fixed amplitude and phase, subject to clean, undisturbed inlet flow. The resulting unsteady pressure distribution is integrated over the moving pressure and suction surfaces to provide

Mode	Frequency (Hz)	Description
1	601.0	1^{st} flap
2	1307.9	2^{nd} flap
3	1913.2	1^{st} torsion
4	2740.6	1^{st} edgewise
5	3148.6	Combined
6	3520.0	Combined
7	4198.4	Combined

Table 5.1: Natural frequencies and modeshapes

the work done on the blade.

5.2.2 Results

Modal Analysis

The modal analysis yielded the first seven natural frequencies listed in Table 5.1 and four modes of interest are illustrated in Figure 5.2. The predicted frequencies were compared to the work of Marshall, 1996, and were found to differ slightly, as shown in Figure 5.3. The almost linear difference does not cause concern because many of the parameters used by Marshall are unspecified. The quality of the FE mesh was confirmed by checking the sensitivity of the natural frequencies to mesh density and element type. The results were compared against the frequencies of two additional models constructed with 195 and 806 linear 8-node brick elements. The effects of mesh refinement were found to be negligible, indicating the fidelity of the mesh.

The interpolation of the modeshape onto the CFD mesh was verified by superimposing the modeshape contour plots of the two meshes using Tecplot. Excellent interpolation accuracy was observed, and no visible difference was observed between the two meshes. The contour plots of the mode 7 axial component are provided in Figure 5.4. It should be noted that the interpolation accuracy was expected to be very high between the two meshes, since the blade shapes are identical and a high proportion of nodes coincide.

Mode No.	Nodal Diameters	V_x Distortion Amplitude	Engine Speed (%)	Modal Force
1	2	1%	112.4%	13.8
2	5	5%	97.8%	10.6
3	7	15%	102.2%	41.6
7	15	15%	104.7%	15.4

Table 5.2: Target inlet conditions and solution modal force

Aerodynamic Forcing

The first step in the aerodynamic analysis yielded the steady flow solution, on which the unsteady calculations were based. A contour plot of the Mach number and entropy at 33% span is provided in Figure 5.5. A thick boundary layer can be seen due to the relatively low mesh resolution, the effects of which are not a significant concern in this case.

The prescribed "target" inlet conditions for the forcing calculation are given in Table 5.2, representing light, but realistic cases. As mentioned in Section 3.1.4, only the stagnation pressure, stagnation temperature and flow angle are specified at the inlet and it is not possible to prescribe all inlet properties. Target properties such as density and velocity are specified as initial conditions at the start of the calculation but are subject to change during the course of the solution. Contour plots of the 7-node inlet axial velocity and density are shown in Figure 5.6 for the steady solution, target inlet conditions and actual inlet conditions achieved at solution. It can be seen that the solution inlet profile differs from the desired prescribed inlet conditions of 15% axial velocity. Smearing of the velocity and density perturbations can be seen towards the tip, together with a reduction in perturbation amplitude. In addition, Figure 5.7 shows that high pressure amplitudes have developed around the tip, caused by upstream travelling pressure disturbances. The resulting modal excitation force for each distortion case is given in Table 5.2.

Mode No.	Frequency (Hz)	Modal Amplitude	Work (J/cycle)	Damping Ratio
1	601.0	1.212×10^{-4}	-0.00486	0.369%
2	1307.9	8.657×10^{-5}	-0.00415	0.130%
3	1913.2	4.860×10^{-5}	-0.0119	0.568%
7	4198.4	4.073×10^{-5}	-0.0111	0.153%

Table 5.3: Aerodynamic damping

Aerodynamic Damping

The solutions of the damping calculations at the specified modal amplitudes are summarised in Table 5.3, where the damping ratio is given by Equation 4.23. It can be seen that aerodynamic damping is very dependent on modeshape, with relatively high damping of the 1^{st} bending and torsion modes. This behaviour is typical for turbomachinery blades and the predicted trend agrees fairly well with Kielb and Imregun [9] for an unshrouded damperless blade. Figure 5.8 shows the imaginary component of the damping force distribution over the pressure surface induced by blade motion in the 1^{st} torsion mode and the work done over one cycle due to motion in the axial direction. Negative work represents areas of positive damping. This representation of damping forces can provide a useful tool for blade designers who wish to fine-tune aerofoil designs to maximise aerodynamic damping for a particular mode.

Forced Response Solution

The modal equation (4.26) is solved for each crossing point in Table 5.4 using the aerodynamic forcing and damping values obtained above. The mode 3 calculation is repeated using a mechanical damping ratio of 0.1% for comparison with the energy method below. The resulting response of each mode is expressed in terms of modal amplitude and tip leading edge amplitude normalised to chord length.

The solutions of the energy equation (4.30) are provided in Table 5.5, where it can be seen that the energy method produces identical results to the modal solution

Mode No.	$\lvert\bar{f}\rvert$	ζ_{aero}	ζ_{mech}	q^{fr}	Tip L.E. Amp. (% chord)
1	13.8	0.369%	0	1.131×10^{-4}	1.096
2	10.6	0.130%	0	6.011×10^{-5}	0.691
3	41.6	0.568%	0	2.532×10^{-5}	0.521
3	41.6	0.568%	0.1%	2.153×10^{-5}	0.443
7	15.4	0.153%	0	0.721×10^{-5}	0.164

Table 5.4: Forced response solutions using modal method

Mode No.	ζ_{mech}	W_f^{cfd} $(J/cycle)$	W_{ad}^{cfd} $(J/cycle)$	W_{md}^{cfd} $(J/cycle)$	Tip L.E. Amp. (% chord)
1	0%	0.005265	-0.00486	0	1.096
2	0%	0.02876	-0.00415	0	0.691
3	0%	0.00635	-0.0122	0	0.521
3	0.1%	0.00635	-0.0122	-0.00214	0.443
7	0%	0.00197	-0.00111	0	0.164

Table 5.5: Forced response solutions using energy method

shown in Table 5.4. To verify the energy method used with mechanical damping, the mode 3 calculation is repeated with an assumed damping ratio of 0.1%, giving full agreement with the modal solution. The energy equation has, therefore, been shown to produce identical results to the modal method for resonant vibration cases both with and without the effect of mechanical damping.

5.3 Siemens Three-Stage Transonic Compressor

5.3.1 Case Description

The Siemens three-stage transonic test compressor shown in Figure 5.9 is a modern high performance modern machine, delivering a high specific flow with a mass flow rate of $26.3 kg/sec$ and a pressure ratio of 3:1 at a rotating speed of $18,650\, rpm$.

Details on the aerodynamic design of the compressor using 3-D design methods are provided by Li and Wells [148]. Consisting of an IGV, stage 0,1, and 2, the compressor has previously been extensively tested by Siemens on a full-scale rotating test rig to evaluate aerodynamic performance and structural integrity. Speed sweeps were carried out to map vibration characteristics with strain gauges applied to three blades in each row. The gauge is positioned on three blades near the trailing edge close to the the hub, as shown in Figure 5.10, and strain readings are averaged over the three blades to reduce the small variation due to blade mistuning. In this case study, the vibration of the last rotor blade is calculated at three resonant crossing points, where excitation of the 8^{th}, 9^{th} and 10^{th} modes is provided by the wakes of the 32 adjacent upstream stator blades. The forced vibration prediction system is verified by comparing predicted aerodynamic performance and blade forced vibration levels with the strain gauge test data.

Structural Modelling

The structural FE model of the blade includes both the aerofoil and root, is fully constrained in space at the upper surfaces of the root flanks and is solved using Ansys. The mesh was supplied by Siemens and is built from 1136 20-node brick elements as shown in Figure 5.11. The original FE mesh shape conformed to the *cold*, unstressed blade profile so the mesh geometry had to be modified to the *hot* shape prior to the aeromechanical analysis. This was primarily to minimise errors in the modeshape interpolation by improving the agreement with the CFD mesh profile. This was done by applying the centrifugal loads at 100% speed in a static analysis, neglecting temperature effects. Steady gas loads were included in the FE model provided by Siemens, which were applied at each radial section at mid-chord. Prior to the modal analysis, the mesh was modified by applying the resulting static deformations to the mesh nodal coordinates. The static analysis was then repeated to give the natural frequencies, modeshapes and prestressing terms, corresponding to the hot blade geometry.

Modeshape Interpolation

The interpolation of the modeshape onto the CFD mesh poses a challenging problem, where the interpolation of high-order modeshapes from a low resolution FE mesh raises several issues, including mesh alignment, shape mismatch, low mesh density and high modeshape gradients. Axial rotational and translational alignment due to differences in the coordinate systems is done by specifying the tip leading edge node indices of the both meshes, then bringing the FE reference node into alignment with the CFD node. An additional axial offset is specified to account for the blunted leading and trailing edges of the FE mesh. Aligning the meshes at the tip leading edge ensures the best possible interpolation accuracy around this critical region with highly localised blade motion.

Modeshapes are interpolated onto the tip clearance region of the CFD mesh, as outlined in Section 4.2.2. Axial and tangential motion of the clearance cells are set equal to blade tip and radial motion is linearly reduced to zero at the casing boundary.

CFD Modelling

The CFD calculations for the 3-stage compressor were performed by Dr. Wei Ning, Siemens, hence only a brief overview of the CFD calculations is provided herein. The steady solution is firstly obtained from a multi-stage analysis through the seven bladerows of the 3-stage machine, upon which, the unsteady flow is calculated from the linearised Navier-Stokes equations. Each blade passage is modelled by about 200,000 mesh points, giving around 1.5 million mesh points for the complete model. The forcing calculation is done through the 7 bladerows to provide the wakes passing through the rotor passages, and the damping calculation involves a single bladerow analysis.

Mode	8	9	10
Frequency *(Hz)*	8556	8823	10100

Table 5.6: Natural frequencies

5.3.2 Results

Modal Analysis

The calculated natural frequencies of modes 8, 9 and 10 at 100% speed are given in Table 5.6. The FE analysis was repeated at zero rotational speed and the Campbell diagram shown in Figure 5.12 was constructed around the crossing points of the 32-E.O. line with the three modes of interest. Here, it can be seen that the 32-E.O. interference from the upstream stator row intersects blade modes 8,9, and 10 at between 70% and 105% engine speed. Included in Figure 5.12 are the modal frequencies of the strain gauge measurements, where it can be seen that the FE modal analysis agrees reasonably well with the test data. As shown in Figure 5.13, the three modes are mainly aerofoil-dominated modes with very little motion at the hub and root, particularly for mode 9.

Modeshape Interpolation

A comparison between the original and interpolated axial component of the mode-shape data is given in Figure 5.14. The interpolation accuracy is very high for all three modes, regardless of a small degree of shape mismatch caused by the 'unloading' and 'reloading' of the FE mesh geometry. Whereas the tip L.E. of both meshes are perfectly aligned, the slight difference in blade twist between the meshes causes a misalignment at the tip T.E. of approximately half the blade thickness. In addition to verifying the interpolation accuracy for a challenging case, this also demonstrates that the mesh interface is very robust to differences in mesh shape.

CFD Solution

The steady flow calculations are compared with measurements at 90% and 100% design speed in Figure 5.15, showing a good overall level of agreement between

	Mode 8	Mode 9	Mode 10
ζ_{tot}	0.35%	0.17%	0.13%
ζ_{aero}	0.11%	0.17%	0.13%
ζ_{mech}	0.24%	Negligible	Negligible

Table 5.7: Aerodynamic and mechanical damping ratios

prediction and measurements, but with a slight under-prediction in efficiency. The resulting modal force and damping ratio from the CFD forcing and damping calculations are provided in Table 5.8.

To compare aerodynamic with mechanical damping, the total system damping, ζ_{tot}, was obtained from the test data using the half-power rule on the strain gauge frequency response. Mechanical damping, ζ_{mech}, is then taken as the difference between system and aerodynamic damping, ζ_{aero}. The comparison in Table 5.7 shows significant mechanical damping for mode 8 and negligible mechanical damping for modes 9 and 10. The mechanical damping for mode 8 is thought to be primarily due to friction at the blade root-disk interface, where a greater degree of root motion is apparent from the modeshape contours. The very small levels of displacement near the root for modes 9 and 10 explain the negligible damping for those modes.

Forced Response Solution

The resulting predicted modal force is used together with the predicted aerodynamic damping and mechanical damping to calculate the resonant displacements and strains for each mode. Table 5.8 lists the modal forcing, $|\overline{f}|$, total modal system damping ratios, ζ_{tot}, and the resulting forced response modal amplitude, q^{fr}. The modal solution was verified by checking the results against the energy method solution, which gave identical responses. Included in the table is the relative error between predicted strains at the gauge position and the measured strain gauge readings.

The mode 8 and 10 predictions show very good agreement. The greater disagreement of mode 9 is believed to be due to the poor positioning of the strain gauge for

Mode No.	Modal Force ($\|\overline{f}\|$)	Damping Ratio (ζ_{tot})	Modal Amp. (q^{fr})	Relative Error with Test
8	11.17	0.35%	5.51×10^{-7}	8%
9	5.25	0.17%	5.02×10^{-7}	65%
10	1.79	0.13%	1.71×10^{-7}	4%

Table 5.8: Forced response solutions

that particular mode (shown in Figure 5.10), raising the question about the accuracy of the mode 9 measurement. Originally positioned to capture the low order modes, the gauge is positioned over a region of high modeshape gradient, as visible in the mode shape contour plots in Figure 5.13. This causes a significant change in strain over the area of the gauge, reducing the accuracy of the strain measurement. Additionally, the strain gauge sensitivity factor, defined as the percentage of the local strain at the gauge location to the maximum strain on the blade, is at a satisfactory level of around 25% for mode 8, but is lower than desired for modes 9 and 10 due to the low modal displacements towards the blade root.

5.4 Conclusions

5.4.1 NASA Rotor 67 Transonic Fan

A case study of the NASA Rotor 67 transonic fan has been reported, providing a detailed demonstration of the complete forced response prediction system, and a basis for the validation of the individual system components. The resonant vibration of a range of modes is modelled with excitation provided by inlet distortions of low and high frequencies to simulate realistic aerodynamic conditions encountered in inlet distortion and bladerow interaction problems.

The FE modal analysis was undertaken with ANSYS using a 20-node brick element mesh, constrained as a cantilevered aerofoil. Mode shapes and natural frequencies are in reasonable agreement with published FE results and were found to be adequately insensitive to mesh resolution.

Very high mode shape interpolation accuracy of the FE-CFD interface was observed by comparing the contours of the original mode shapes on the FE mesh with interpolated mode shapes on the CFD mesh.

The CFD steady solution is in agreement with previous work of the research group by Li and He [74]. The inlet axial velocity and density distortions show a smearing of the target distortion pattern, which is likely to be due to upstream-travelling pressure waves. Aerodynamic damping calculated with blade motion in each of the prescribed modes shows reasonable damping predictions.

The decoupled forced response solution has been successfully implemented in a hypothetical but realistic case study. Forced vibration levels are within the expected order of magnitude, with the 1^{st} bending mode giving a tip deflection of approximately 1% chord.

The energy method is shown to provide identical results to the solution of the modal equation when implemented both with and without mechanical damping, demonstrating that the energy method provides a simple alternative to the solution of the modal equation.

5.4.2 Siemens Three-Stage Transonic Compressor

The forced response system was applied to predict the vibration of the last stage rotor of the Siemens three-stage transonic test compressor, caused by high frequency interference from the upstream stator wakes at three crossing points on the Campbell diagram. The system was validated by comparing predictions with aerodynamic performance and strain gauge measurements from a full-scale rotating engine test.

The FE mesh includes the root and originally conformed to the cold, unloaded shape. The mesh geometry was modified to match the hot, running shape based on a static FE analysis incorporating centrifugal and steady gas loads. Agreement in shape with the hot shape of the CFD mesh boundary was significantly improved but a visible difference in tip twist remained. Predicted natural frequencies agreed well with the measured blade frequencies.

The modeshape interpolation for this industrial case provided a challenging problem, raising several practical issues, including mesh alignment, shape mismatch, low

mesh density and high mode shape gradients. Mode shapes were interpolated with very high accuracy, overcoming the above complications. The interpolation method was found to be surprisingly robust to mismatching meshes, where a large difference in twist at the tip trailing edge caused no reduction in interpolation accuracy.

The 7-bladerow CFD calculation predicted the compressor performance maps with good agreement with measured data, but gave a slight under-prediction of efficiency. Predicted aerodynamic damping compared well with total measured system damping, for modes 9 and 10. An under-prediction in damping for mode 9 suggests significant mechanical damping due to a greater amount of movement at the root providing friction damping at the root-disk interface.

The forced response strain predictions, calculated using system damping, agreed within 10% of strain gauge readings for modes 8 and 10. The mode 9 result gave a discrepancy of 65%. However, the mode 9 result is inconclusive due to the poor positioning of the strain gauge for that mode.

It has been demonstrated that the forced response system is capable of predicting resonant strains with acceptable accuracy. The high efficiency of the unsteady multi-stage calculation enables the the system to be used routinely in the blade design process to tackle aeromechanical issues, where the turnaround time for each mode is a few hours on a single processor workstation.

5.5 Figures

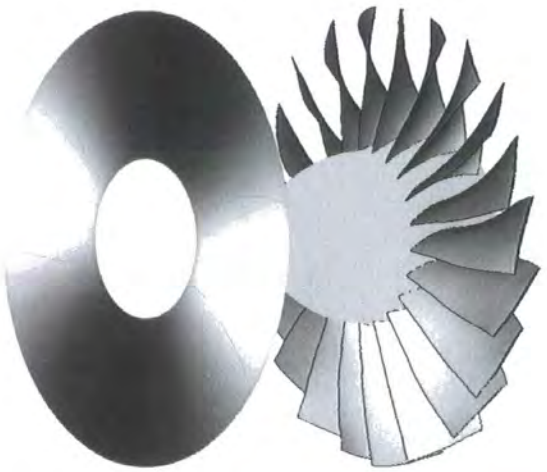

Figure 5.1: NASA Rotor 67 fan rotor geometry with contour plot of 2-node inlet distortion

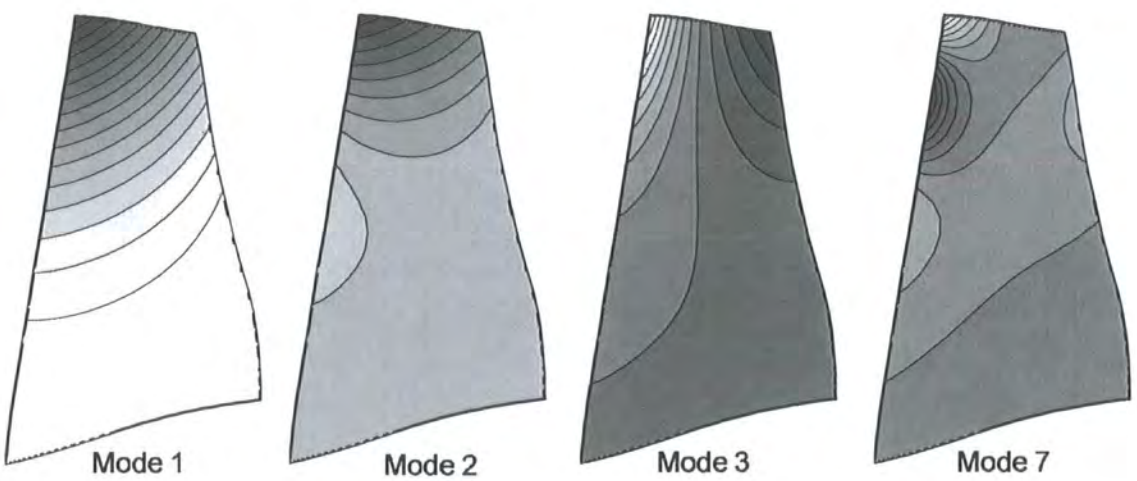

Figure 5.2: Mode shape axial components

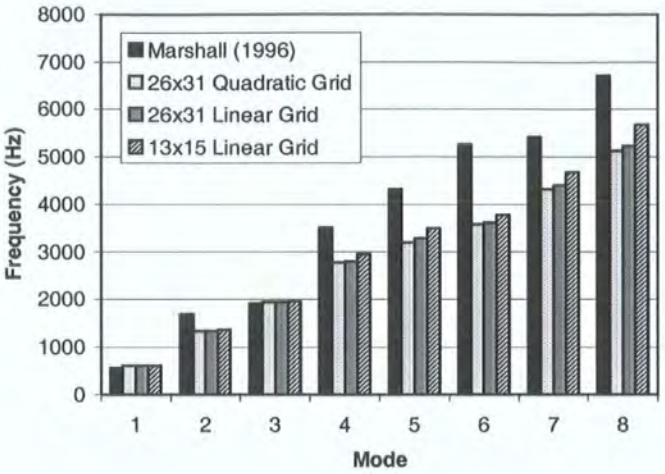

Figure 5.3: Comparison of natural frequencies with results of Marshall, 1996

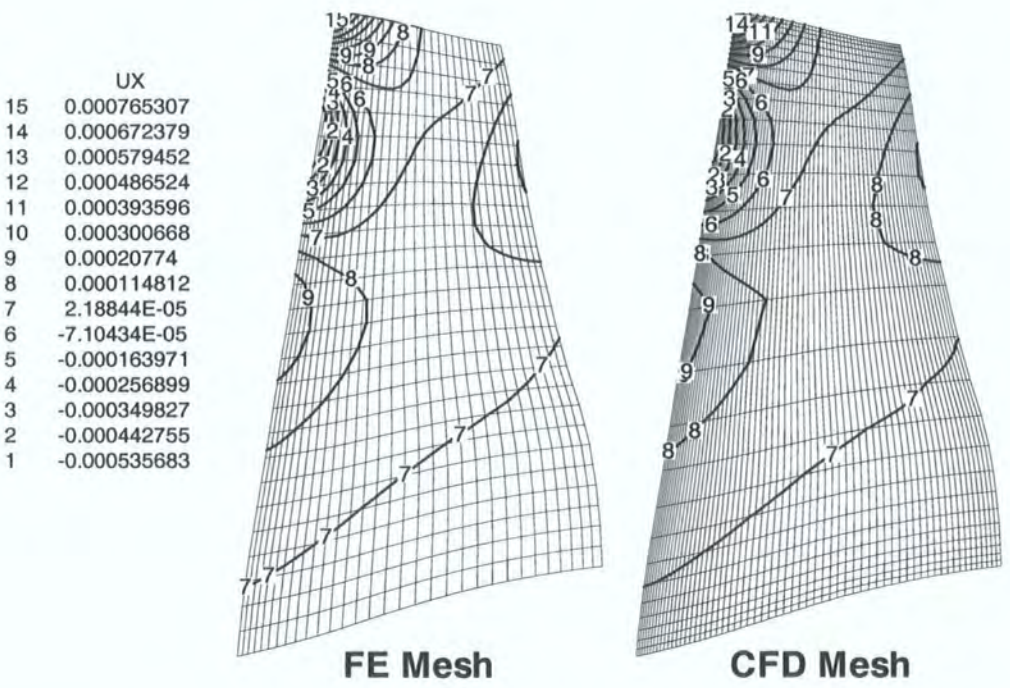

Figure 5.4: Comparison of original and interpolated modeshape (axial component)

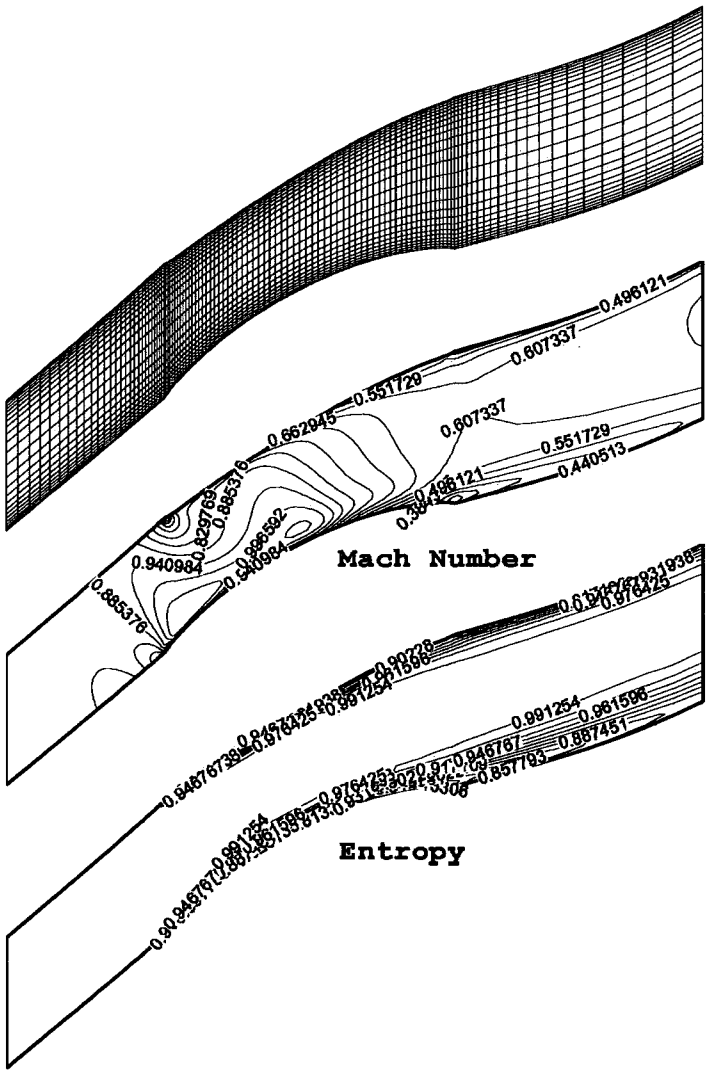

Figure 5.5: CFD mesh section and steady solution plotted at $\frac{1}{3}$ span)

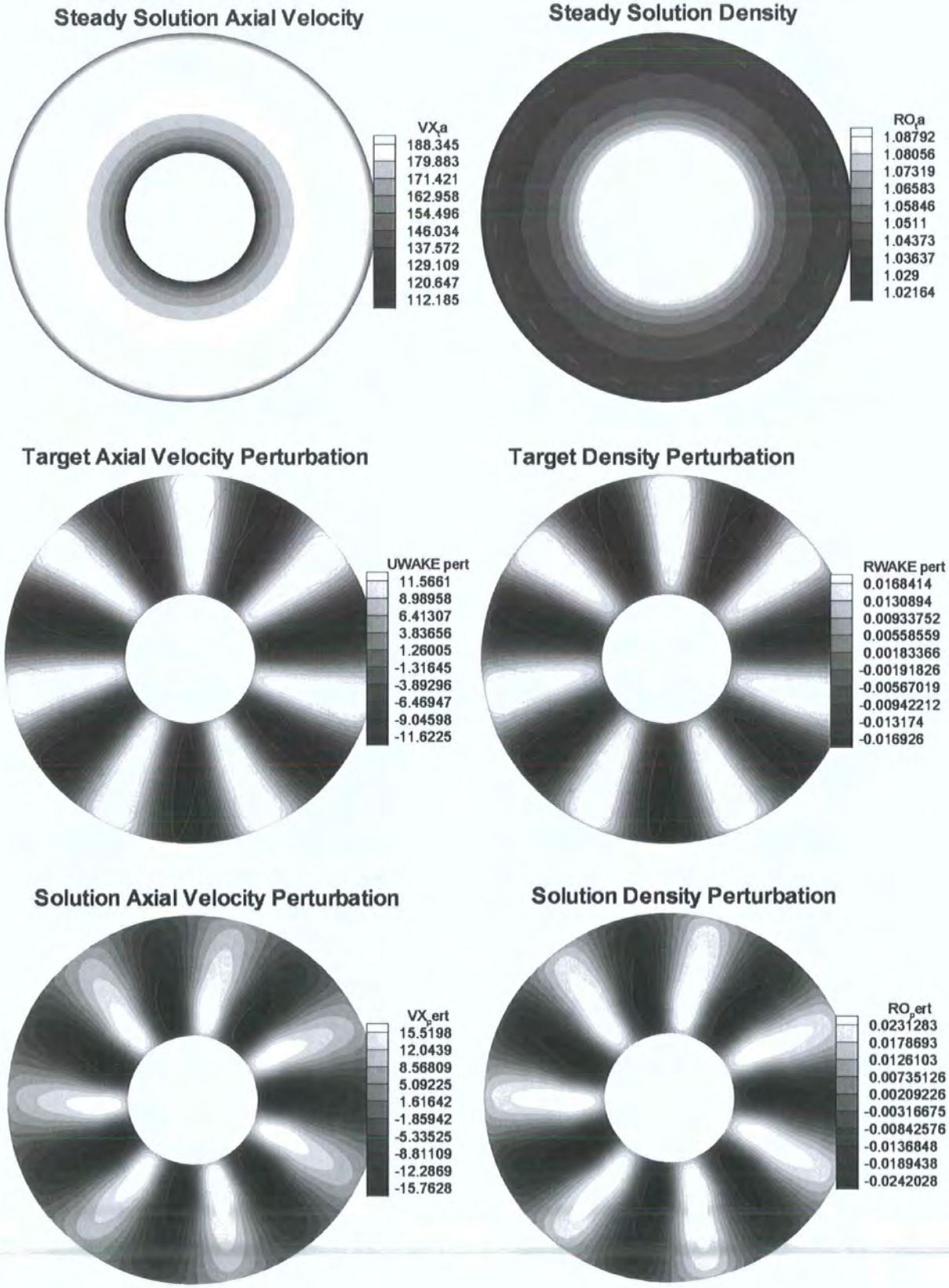

Figure 5.6: Inlet axial velocity and density distortion

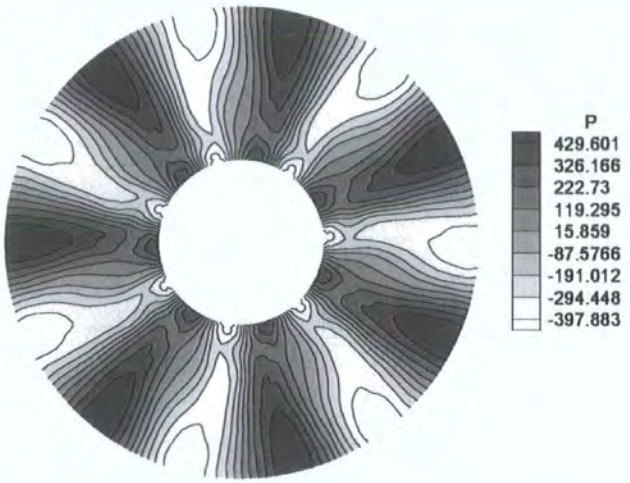

Figure 5.7: Inlet total pressure perturbation of solution

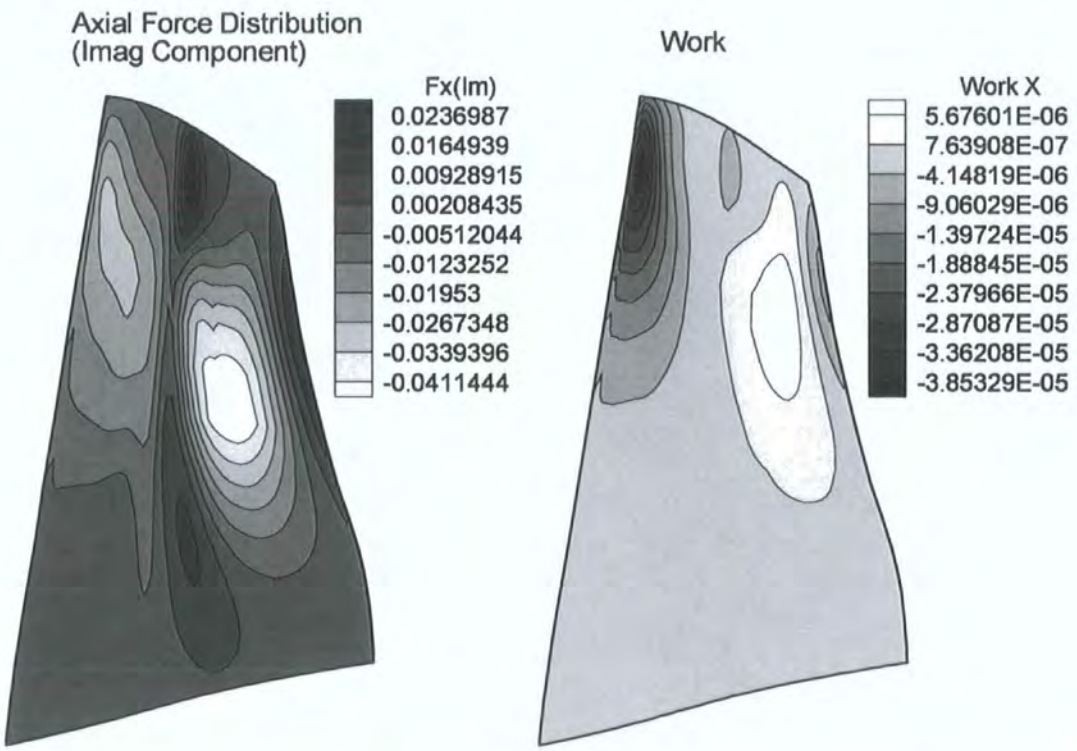

Figure 5.8: Mode 3, imaginary component of axial force and work in axial direction

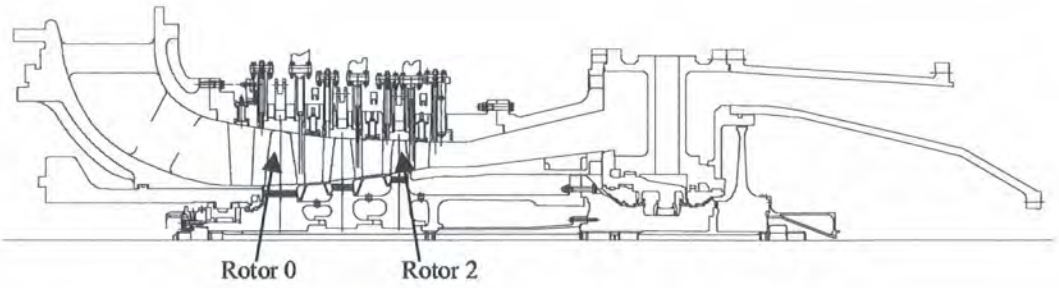

Figure 5.9: Cross section of Siemens 3-stage transonic compressor

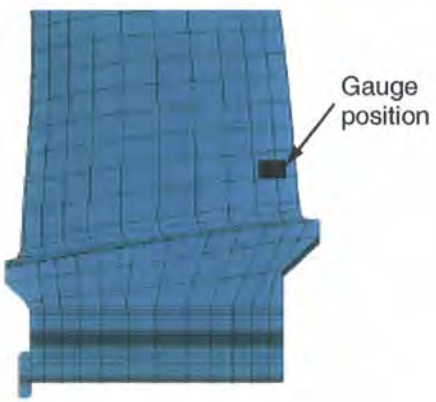

Figure 5.10: Strain gauge location on Rotor 2 blade

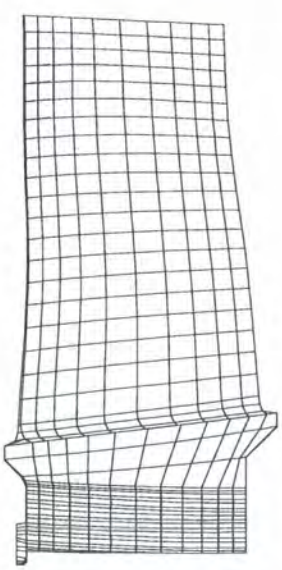

Figure 5.11: FE mesh of compressor blade

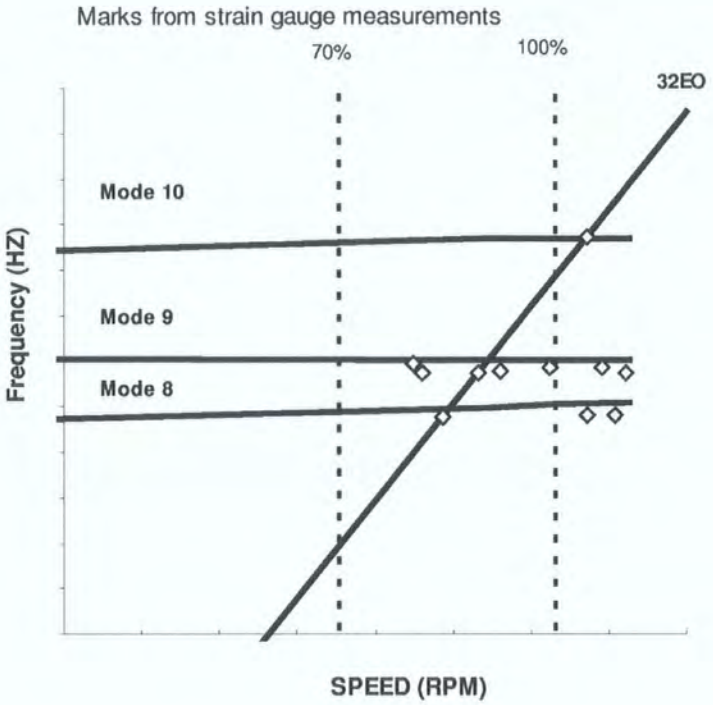

Figure 5.12: Campbell diagram around 32E.O. crossing point with modes 8, 9 and 10

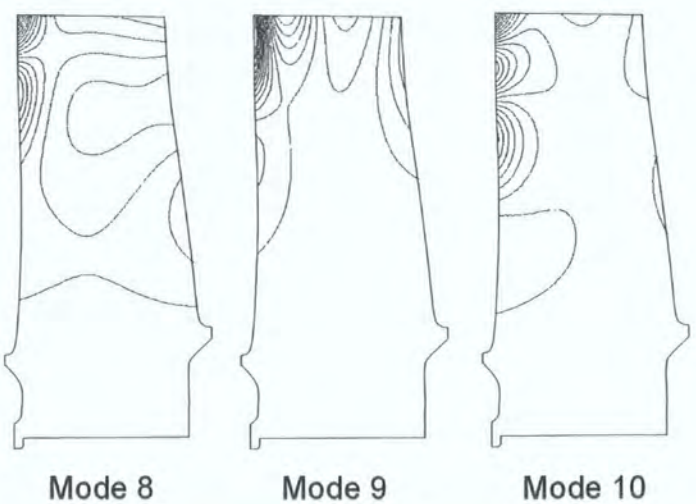

Figure 5.13: Axial modeshape components of modes 8,9 and 10

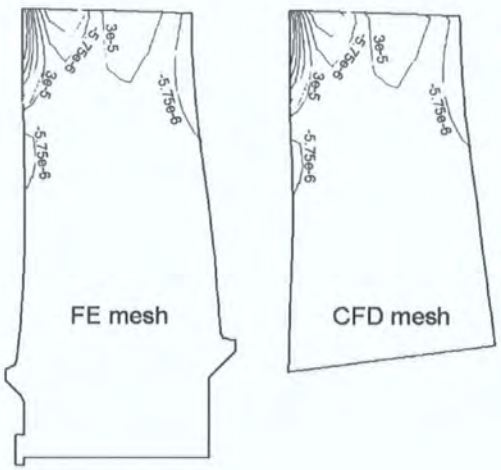

Figure 5.14: Comparison of original and interpolated modeshape for mode 9 axial component

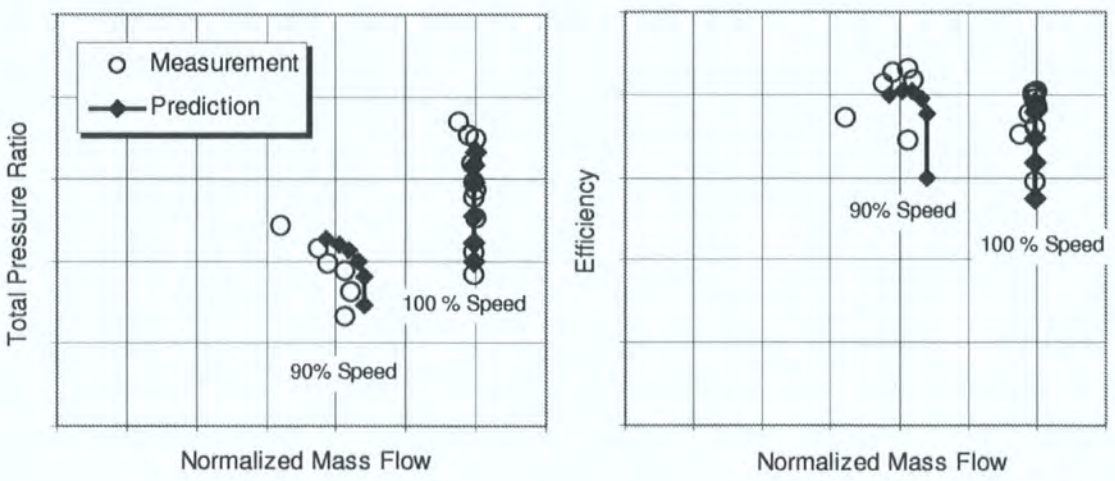

Figure 5.15: Comparison of predicted and measured performance maps

Chapter 6

Fully-Coupled Forced Response Methods

6.1 Introduction

Two fully-coupled methodologies have been developed with the original intention of halving the solution time of the decoupled method by combining the aerodynamic forcing and damping calculations into a single solution. The two fully-coupled methodologies simultaneously solve the structural and fluid equations within the CFD solver to yield the steady-state blade response at the resonant crossing of interest. The introduction of a fluid-structure coupling effect in the fully-coupled solution creates a significant frequency shift effect, allowing an evaluation on the use of both decoupled and fully-coupled methods for forced response calculations.

Conventional fully-coupled methods involve the time-accurate solution of the fluid and structural equations, with the exchange of instantaneous fluid pressures and structural displacements taking place in the time domain. Based on the non-linear harmonic unsteady aerodynamic solution in the frequency domain, two approaches for flow-structure coupling have been developed based on the solution of the modal equation in both the frequency-domain and the time-domain. Both the fluid and structural equations are solved numerically, with an exchange of pressure and displacement amplitudes passed across the fluid-structure boundary at each step in the solution.

6.2 Frequency Domain Method

The frequency domain method solves both the fluid and structural equations simultaneously by numerically integrating the equations in pseudo-time. Shown in Figure 6.1, the fluid and structural domains are combined into a tightly coupled system. An exchange of information after each solution step provides the continuous feedback of aerodynamic loads and blade vibration levels between the fluid and structure. A single aerodynamic solution includes the effects of blade vibration, inlet distortion and bladerow interaction to provide the combined aerodynamic forcing and damping loads.

Structural modelling is based on modal reduction theory, with the FE modal analysis and mode shape interpolation implemented in an identical manner to the decoupled method described in Chapter 4. However, the difference in the coupled structural solution is the numerical formulation of the modal equation to deal with the combined solution of aerodynamic excitation and damping loads. Whereas the aerodynamic damping ratio in the decoupled calculation is known before the analytical solution of the modal equation, the aerodynamic damping loads in the coupled solution only become apparent during the course of the solution and must be treated as forcing terms on the right-hand side of the modal equation, which is solved numerically. The modal equation is therefore expressed in the form

$$\ddot{q}(t) + 2\zeta_{mech}\,\omega_n \dot{q}(t) + \omega_n^2 q(t) = \left(f(t) + d(q,t)\right), \tag{6.1}$$

where $f(t) + d(q,t)$ is the combined aerodynamic modal force output from the fluid solver. Representing the modal velocity as $v = \dot{q}$ and assuming harmonic motion and forcing gives

$$\begin{aligned} q &= \tilde{q}e^{\mathbf{i}\omega\mathbf{t}}; \quad & v &= \tilde{v}e^{\mathbf{i}\omega\mathbf{t}}; \\ f &= \tilde{f}e^{\mathbf{i}\omega\mathbf{t}}; \quad & d &= \tilde{d}e^{\mathbf{i}\omega\mathbf{t}} \end{aligned} \tag{6.2}$$

The modal equation (6.1) is then represented by the two equations

$$\tilde{v} = \mathbf{i}\omega\tilde{q} \quad \text{and} \quad \left(2\zeta_{mech}\,\omega_n + \mathbf{i}\omega\right)\tilde{v} + \omega_n^2\tilde{q} = \left(\tilde{f} + \tilde{d}(q)\right), \tag{6.3}$$

where the complex damping force is a function of the modal amplitude. Letting

$$\tilde{a}_q = \mathrm{i}\omega \quad \text{and} \quad \tilde{a}_v = 2\zeta_{mech}\omega_n + \mathrm{i}\omega, \tag{6.4}$$

and introducing the pseudo-time derivatives $R_q = \frac{\partial \tilde{q}}{\partial \tau}$ and $R_v = \frac{\partial \tilde{v}}{\partial \tau}$, into Equation 6.3 gives

$$\frac{\partial \tilde{q}}{\partial \tau} + \tilde{a}_q \tilde{q} = \tilde{v} \quad \text{and} \quad \frac{\partial \tilde{v}}{\partial \tau} + \tilde{a}_v \tilde{v} + \omega_n^2 \tilde{q} = \left(\tilde{f} + \tilde{d}(q)\right) \tag{6.5}$$

The pseudo-time derivatives for each stage m of step n in the 4-stage Runge-Kutta solution are expressed as

$$\begin{aligned} \tilde{R}_q^{(n,m)} &= \tilde{v}^{(n,m)} - \tilde{a}_q \tilde{q}^{(n,m)} \\ \tilde{R}_v^{(n,m)} &= \left(\tilde{f} + \tilde{d}\right)^{(n)} - \tilde{a}_v \tilde{v}^{(n,m)} - \omega_n^2 \tilde{q}^{(n,m)} \end{aligned} \tag{6.6}$$

(n=1,2,3...; m=0,1,2,3)

The modal displacement and velocity terms at each stage of a Runge-Kutta step are given by

$$\begin{aligned} \tilde{q}^{(n,0)} &= \tilde{q}^{(n-1,4)} \\ \tilde{v}^{(n,0)} &= \tilde{v}^{(n-1,4)} \\ \\ \tilde{q}^{(n,1)} &= \tilde{q}^{(n,0)} + \frac{1}{2} d\tau \; R_q^{(n,0)} \\ \tilde{v}^{(n,1)} &= \tilde{v}^{(n,0)} + \frac{1}{2} d\tau \; R_v^{(n,0)} \\ \\ \tilde{q}^{(n,2)} &= \tilde{q}^{(n,1)} + \frac{1}{2} d\tau \; R_q^{(n,1)} \\ \tilde{v}^{(n,2)} &= \tilde{v}^{(n,1)} + \frac{1}{2} d\tau \; R_v^{(n,1)} \\ \\ \tilde{q}^{(n,3)} &= \tilde{q}^{(n,2)} + d\tau \; R_q^{(n,2)} \\ \tilde{v}^{(n,3)} &= \tilde{v}^{(n,2)} + d\tau \; R_v^{(n,2)} \end{aligned} \tag{6.7}$$

where $d\tau$ is pseudo-time step size.

The last stage of the current pseudo-time step taken as a combination of the previous four stages using

$$\begin{aligned}\tilde{q}^{(n,4)} &= \tilde{q}^{(n,0)} + d\tau\left\{\frac{1}{6}\tilde{R}_q^{(n,0)} + \frac{1}{3}\tilde{R}_q^{(n,1)} + \frac{1}{3}\tilde{R}_q^{(n,2)} + \frac{1}{6}\tilde{R}_q^{(n,3)}\right\} \\ \tilde{v}^{(n,4)} &= \tilde{v}^{(n,0)} + d\tau\left\{\frac{1}{6}\tilde{R}_v^{(n,0)} + \frac{1}{3}\tilde{R}_v^{(n,1)} + \frac{1}{3}\tilde{R}_v^{(n,2)} + \frac{1}{6}\tilde{R}_v^{(n,3)}\right\}\end{aligned} \tag{6.8}$$

After convergence of the pseudo-time marching solution, the $R_q^{(n,m)}$ and $R_v^{(n,m)}$ terms on the left-hand side of Equation 6.6 disappear, recovering the original modal equation and definition of velocity given in Equation 6.3.

6.3 Hybrid Frequency-Time Domain Method

An alternative hybrid approach is based on the continuous time-domain solution of the modal equation with periodic updating of the aerodynamic modal force. The fluid calculations are performed in an identical manner to the previous approach, with the exchange of fluid and structural boundary conditions at each step in the fluid solution. The difference from the frequency domain method is the time-marching of the modal equation. As shown in Figure 6.2, the harmonic modal force from the previous fluid step is reconstructed and the modal equation is marched in time over one forcing period. A Fourier transform of the response over the period is taken to yield the complex modal amplitude for feedback to the fluid solver in the frequency-domain. The modal equation experiences continuous time-marching over the entire coupled solution with periodic updating of the combined aerodynamic forcing and damping terms from the fluid solver. This approach is suitable for lightly damped cases, where blade transient effects take many periods to decay, thus allowing the fluid solver to react sufficiently to the blade dynamics.

The coupled modal equation (6.1) is solved by direct time integration using the 4-stage Runge-Kutta scheme. Defining the modal velocity as $v = \dot{q}$, the modal equation is represented in the time domain by the two equations

$$v = \dot{q} \quad \text{and} \quad \dot{v} + 2\zeta_{mech}\,\omega_n v + \omega_n^2 q = (f + d)\,. \tag{6.9}$$

The displacement and velocity derivatives are taken as

$$\begin{aligned} \dot{q} &= \frac{dq}{dt} = R_q \\ \dot{v} &= \frac{dv}{dt} = R_v. \end{aligned} \tag{6.10}$$

At each each stage of a Runge-Kutta time step, the time derivatives are given by

$$\begin{aligned} R_q^{(n,m)} &= v^{(n,m)} \\ R_v^{(n,m)} &= (f+d)^{(n)} - 2\zeta_{mech}\,\omega_n v^{(n,m)} - \omega_n^2 q^{(n,m)} \end{aligned} \tag{6.11}$$

leading to the modal displacement and velocity terms at each stage

$$\begin{aligned} q^{(n,0)} &= q^{(n-1,4)} \\ v^{(n,0)} &= v^{(n-1,4)} \end{aligned}$$

$$\begin{aligned} q^{(n,1)} &= q^{(n,0)} + \frac{1}{2}dt\; R_q^{(n,0)} \\ v^{(n,1)} &= v^{(n,0)} + \frac{1}{2}dt\; R_v^{(n,0)} \end{aligned}$$

$$\begin{aligned} q^{(n,2)} &= q^{(n,1)} + \frac{1}{2}dt\; R_q^{(n,1)} \\ v^{(n,2)} &= v^{(n,1)} + \frac{1}{2}dt\; R_v^{(n,1)} \end{aligned} \tag{6.12}$$

$$\begin{aligned} q^{(n,3)} &= q^{(n,2)} + dt\; R_q^{(n,2)} \\ v^{(n,3)} &= v^{(n,2)} + dt\; R_v^{(n,2)} \end{aligned}$$

The last stage of the time step is then given by

$$\begin{aligned} q^{(n,4)} &= q^{(n,0)} + dt\left\{\frac{1}{6}R_q^{(n,0)} + \frac{1}{3}R_q^{(n,1)} + \frac{1}{3}R_q^{(n,2)} + \frac{1}{6}R_q^{(n,3)}\right\} \\ v^{(n,4)} &= v^{(n,0)} + dt\left\{\frac{1}{6}R_v^{(n,0)} + \frac{1}{3}R_v^{(n,1)} + \frac{1}{3}R_v^{(n,2)} + \frac{1}{6}R_v^{(n,3)}\right\} \end{aligned} \tag{6.13}$$

6.4 Comparison with Decoupled Method

The NASA Rotor 67 transonic fan rotor described in Section 5.2 is used as a test case to provide a comparison of the coupled methods with the decoupled method.

Mode No.	Mode Type	Frequency (Hz)	No. Nodal Diameter	V_x Distortion Amplitude
1	1^{st} bend	601.0	2	1%
2	2^{nd} bend	1307.9	5	5%
3	1^{st} torsion	1913.2	7	15%
7	combined	4198.4	15	15%

Table 6.1: Resonant conditions

The coupled solutions of the forced response amplitudes are obtained for modes 1,2,3 and 7 at identical operating conditions to the decoupled calculations, allowing an accurate comparison of the methodologies.

Modes 1, 2, 3 and 7 are chosen to provide forced response studies typical of low frequency inlet distortion and high frequency bladerow interaction problems. Blade excitation is provided by hypothetical inlet distortions with the number of nodal diameters chosen to provide resonant forcing at a frequency close to design speed. Inlet flow conditions are based on the steady solution close to design load, where the inlet flow perturbation is determined by specifying the amplitude of variation in axial velocity, V_x, and applying a variation in density to ensure isentropic inlet conditions. A summary of the resonant conditions is provided in Table 6.1 and a more detailed description of the case is given in Section 5.2.

The forced response predictions given by the coupled and decoupled methods at the blade natural frequencies without mechanical damping are listed in Table 6.2. The solution amplitudes are expressed in terms of the absolute blade vibration amplitude at the tip leading edge, normalised by chord length. Whilst a very high level of agreement is seen between the two coupled methods, the responses predicted by the coupled solutions of all modes were found to be significantly lower than the decoupled solutions. By repeating the coupled calculations at frequencies around the natural frequency, it can be observed in Figure 6.3 that the resonant peak of the coupled solution is subject to a frequency shift. Conversely, the peak of the decoupled solution does not show any noticeable frequency shift.

Whilst the decoupled solution encounters resonance at the natural frequency,

Mode No.	Decoupled Tip L.E. Amp. (% Chord)	Coupled (freq. domain) Tip L.E. Amp. (% Chord)	Coupled (hybrid) Tip L.E. Amp. (% Chord)	Response Drop (%)
1	1.096	0.949	0.949	13.81
2	0.691	0.628	0.628	8.03
3	0.521	0.498	0.498	4.37
7	0.164	0.116	0.116	29.03

Table 6.2: Decoupled and coupled response predictions at blade natural frequency

the coupled solution is excited slightly off-resonance at the natural frequency and experiences a lower amplitude of vibration. The peak amplitudes given by the coupled and decoupled methods at their respective frequencies can be seen to agree very closely. It is evident that both methods are capable of predicting peak forced vibration levels with a high level of agreement, providing that the coupled calculation is performed at the correct frequency. Whereas both methods have been shown to be capable of predicting the magnitude of the blade response at the resonant peak, it has been demonstrated that the decoupled method accurately predicts the peak vibration from a single solution without consideration for frequency shift. However, in the coupled solution the resonant frequency is unknown and must be found to avoid the risk of under-predicting the response at an off-resonant condition.

6.5 Resonance Tracking

The dependency on solution frequency creates an additional DoF into the coupled calculation, which can not be obtained directly from the governing equations. As discussed later in Section 7.5, the resonant frequency can not be calculated from a coupled solution at any one frequency due to the limited information that can be obtained from the combined aerodynamic force. Instead, the coupled solution must be repeated at a number of discrete frequencies around the resonant peak to reveal the frequency response curve, which can be done with an open-loop frequency sweep or by implementing a closed-loop resonance tracking algorithm. Whilst the

fully-coupled method models the physical system in a more realistic manner, this case suggests that a higher degree of modelling is required in the coupled solution to include the effects of the additional phenomena captured in the analysis. The sources of the frequency shift and the implications on the coupled method are now discussed in detail.

An efficient resonance tracking scheme is implemented to direct the solution towards the resonant frequency, hence avoiding the excessive computation of a frequency sweep. Exploiting the fact that the frequency-domain fluid solution can be efficiently restarted at a new frequency, the scheme was developed with the intention of minimising computing time. By approximating portions of the bell-shaped frequency response curve by the parabola

$$a\omega^2 + b\omega + c = q \tag{6.14}$$

it is possible to accurately predict the resonant frequency with a small number of iterations. Starting with the coupled solution at the blade natural frequency, the solution is restarted twice to obtain a further two solutions at frequencies close to the natural frequency. Fitting a parabolic curve to the three points on the response curve enables an estimate of the resonant frequency, as shown in Figure 6.4. Depending where the three points lie on the response curve, the quadratic coefficient, a, of the parabola will be either positive or negative. Negative values result in an upturned parabola approximating the top of the bell-shaped response curve close to the resonant peak. This allows the resonant frequency to be estimated by simply calculating the stationary point of the curve, giving the frequency corresponding at the peak. If desired, the solution can be repeated at the estimated peak to verify the resonant frequency.

Positive values of the quadratic coefficient approximate the lower parts of the bell-shaped response curve at frequencies either above or below the resonant peak. Here, the stationary point will not correspond to the resonant peak and an iteration in solution frequency is required. In this situation, the solution frequency is updated by a pre-defined step size. A step increase or decrease is determined by comparing response amplitudes of the previous solutions to find whether the current frequency is above or below resonance, indicated by the sign of the slope. The coupled solution

is restarted at the new frequency and a new parabola is calculated using the latest three frequencies. The frequency updating is repeated until a negative parabola is achieved and the resonant peak can be calculated at the stationary point. In order to speed up convergence, the frequency step size is reduced if oscillation in solution frequency is detected. This allows a relatively large initial frequency step be specified, which is then automatically reduced in the eventuality that the algorithm overshoots the natural frequency.

The fully-coupled solution with resonance tracking was performed for Mode 3, giving a frequency shift of 3.5 Hz and peak amplitude at tip L.E. of 1.098% chord. The coupled resonant frequency is in agreement with the analytical calculation shown in Table 7.1 which is derived later in Section 7.3.2. Using an initial step size of 1.0 Hz and a step reduction factor of 0.4, convergence in frequency was achieved after around six solutions, as shown graphically in Figure 6.5. Whilst the fluid calculation was performed six times, the restart capability of the frequency domain CFD solver resulted in the total computing time being approximately double that of a single complete coupled calculation. This results in the total computing time of the coupled solution with resonance tracking being roughly equal to the decoupled solution.

6.6 Convergence Behaviour

In order to avoid instability and excessive solution times in the coupled solution, the convergence rate of the modal equation must be similar to that of the fluid equations. Whilst the convergence rate of the CFD calculation dominates the solution time, the rate of the modal solution must be adjusted to match that of the fluid. Instability occurs when the modal equation converges at a faster rate than the fluid, where the aerodynamic damping forces cannot respond to the blade motion. Under such conditions, the relatively unresponsive damping force will effectively cause further blade excitation and the motion will tend to incorrectly lag the combined aerodynamic force by 90° with excessive amplitude, until the flow equations react accordingly. In other words, the system will behave in an undamped fashion, wrongly forced by

the total aerodynamic loads at the current stage of the aerodynamic solution. A high degree of oscillation will occur and the overall solution will diverge. Slowing the modal convergence adds stability to the system, but a modal equation that converges much slower than the fluid equations gives a sluggish response, increasing the overall solution time.

For a situation where it is desirable to minimise the coupled solution time, it would be necessary to optimise the convergence rate of the modal equation. A rate too fast will cause oscillation and increase solution time; and a rate too slow will also prolong the converged solution. The methods of controlling the modal convergence rate are different for frequency-domain and the hybrid approaches. For the frequency-domain approach, the convergence rate is controlled by adjusting the pseudo-time step size, which is determined independently to the step size used in the flow equations. In the hybrid approach, stability is ensured by averaging the current solution modal amplitude over a number of previous values, effectively smoothing the structural response that is fed back to the fluid solver. Conversely, convergence can be accelerated by increasing the number of periods the modal equation is marched per solution step.

6.7 Summary

Two fully coupled forced response methods have been developed with the intention of increased efficiency over the decoupled method, where the calculation of aerodynamic forcing and damping loads are combined into a single calculation. Based on the frequency-domain nonlinear harmonic method, the modal equation is fully integrated into the flow solver and solved using two approaches: directly in the frequency domain; and by time-marching using a hybrid approach. The coupled and decoupled solutions were obtained for three low order modes and one high order mode of the NASA Rotor 67 transonic aero fan. Blade excitation is given by hypothetical inlet distortions in order to provide a realistic test case that is typical of inlet distortion and bladerow interaction problems.

The results show that both coupled approaches produce identical results to one

another, but are significantly lower than the decoupled solution at the natural frequency. It has been identified that this is due to the coupled solutions being subject to a shift in resonant frequency, causing the solution at the natural frequency to be moved slightly off-resonance. In contrast, the decoupled solution inherently assumes no such shift from the blade natural frequency.

The coupled calculations always under-predict resonant vibration levels unless a frequency sweep or resonance tracking scheme is implemented. The coupled and decoupled solutions agree only when the coupled analysis is performed at the resonant frequency, which is found by repeating the coupled calculation for a range of frequencies. A novel resonance tracking scheme is implemented, based on parabolic curve fitting to the frequency response curve, enabling the resonant frequency of the coupled solution to be found with very high efficiency. However, the need for resonance tracking increases the overall computational effort of the coupled solution, and the gain in efficiency of a single solution over the decoupled approach is lost. Therefore a coupled solution will be more time-consuming than a decoupled solution for resonant forced response prediction.

Whereas the coupled solution frequency shift has been clearly demonstrated, there are questions regarding the source of the frequency shift and the implications on the accuracy on decoupled and fully coupled methods that are yet to be answered. Chapter 7 provides an analytical investigation into the mechanics behind the frequency shift to provide an explanation of the cause of the coupling effects and the influence on decoupled and fully coupled predictions.

6.8 Figures

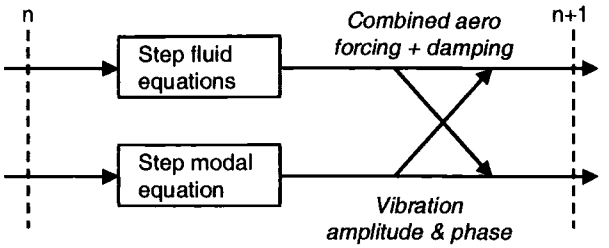

Figure 6.1: Frequency-domain fully coupled system

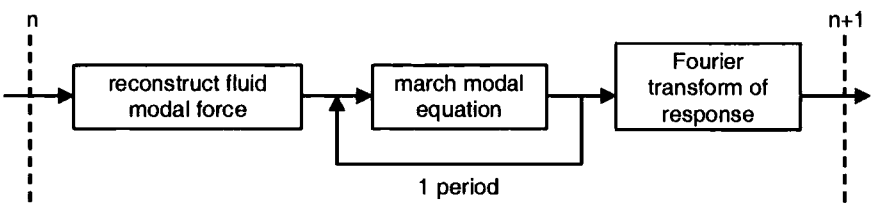

Figure 6.2: Hybrid fully coupled system

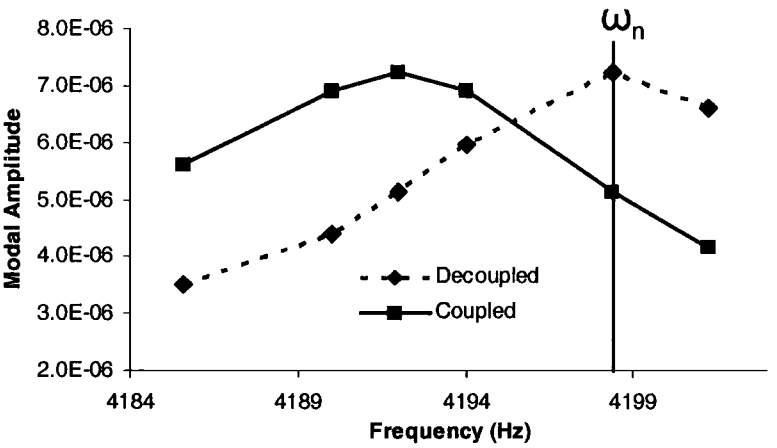

Figure 6.3: Coupled and decoupled solutions around resonant peaks for Mode 7

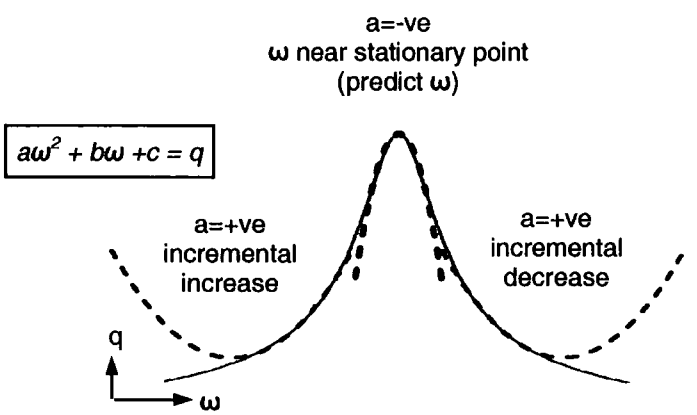

Figure 6.4: Resonance tracking using parabolic curve fitting

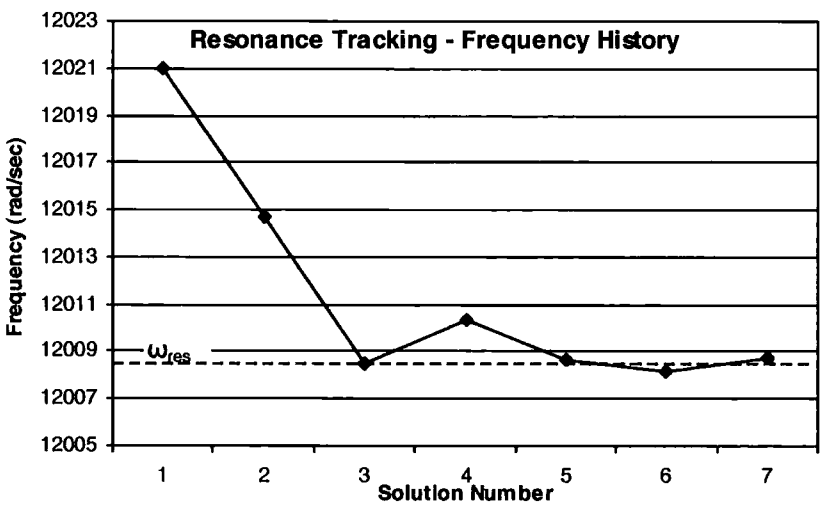

Figure 6.5: Convergence in frequency of resonance tracking scheme

Chapter 7

Fluid-Structure Coupling Effects

7.1 Introduction

It was demonstrated in Chapter 6 that decoupled systems can accurately predict resonant vibration amplitudes from a single calculation at the blade natural frequency, whilst fully-coupled forced response solutions are subject to a shift in resonant frequency and require multiple solutions. The obvious impact on the coupled solution is the additional computational cost of the resonance tracking to avoid under-predicting vibration levels if the resonant peak is not sufficiently captured. Whilst a single coupled calculation is preferable to multiple calculations, the need for resonance tracking is indicated by the level of agreement between a single coupled calculation at the natural frequency and the resonant peak.

This chapter explains the reasons behind the frequency shift with an investigation into fluid-structure coupling effects and a detailed look at the way in which fluid-structure interaction is incorporated into decoupled and fully coupled methods. The principles behind the coupling effect are discussed to identify the main source of the frequency shift and to provide a basis to evaluate the impact on decoupled and coupled methods.

The decoupled method is adapted to represent the combined aerodynamic forcing and damping loads in a similar manner to coupled methods. This allows the analytical breakdown of the mechanics behind the decoupled and coupled solutions, providing an understanding of the source of frequency shift. The basic flow-structure

coupling effects are then investigated, leading to an evaluation of the use of decoupled and fully-coupled forced response methods in practical situations.

7.2 Added Mass Effect

The difference in behaviour between the decoupled and fully-coupled methods is due to the fluid-structure coupling effect present in the coupled solution resulting from the aerodynamic damping forces. For a specific blade motion, the induced pressures acting on the blade result in a modal damping force which lags the blade motion for forced response cases (modal force will lead the motion for flutter cases), as illustrated on the Argand diagrams in Figure 7.1. Here, a complex aerodynamic modal damping force is induced by a real modal displacement amplitude. In a dynamic situation, the modal amplitude will vary in phase and magnitude and the damping force will lag by a fixed relative phase angle with the magnitude increasing in a linear manner, based on the assumption of linear aerodynamic damping. In the coupled solution, the real and imaginary damping force components have two distinct effects on the dynamic response of the system. Damping is provided solely by the imaginary (out-phase) force component due to the fact that no work can be done by the real (in-phase) component. However, the real component is aligned with the blade inertial forces, therefore, causing a variation of the blade *dynamic mass.* The result is an *added mass effect*, leading to a change in the dynamic resonant frequency. In this thesis, the real and imaginary components are referred to as inertial and viscous components respectively. The viscous component is named as such for the reason that it provides the disspiative aerodynamic damping effect to the blade, and is not to be confused with the viscous fluid forces. The viscous and inertial components of the complex modal force are determined by the interaction of pressure fluctuations with the mode shape and are not directly related to the viscous terms of the flow equations.

The decoupled method considers the damping force as an equivalent viscous damping ratio based on the damping work, as shown in Equation 4.23. The inertial component of the damping force is subsequently neglected, removing the capability

of the decoupled method to include the added mass effect. Since the dynamic mass of the system is unchanged, the decoupled solution does not experience any significant frequency shift. In contrast, the inertial and viscous components in the coupled solution can not be separated due to the fact that excitation and damping forces are combined and cannot be identified. The added mass effect is therefore an integral part of the coupled solution.

7.3 Modified Decoupled Method

7.3.1 Formulation

An investigation into the coupling effect is carried out using an adapted version of the decoupled method to model the added mass effect based on the analytical solution of the coupled equation (6.1). The decoupled method considers aerodynamic damping as an equivalent viscous damping ratio, where the analytical solution at arbitrary excitation frequency given in Equation 4.25 is expressed as

$$\tilde{q} = \frac{\tilde{f}}{(\omega_n^2 - \omega^2) + \mathbf{i}\left(2\left(\zeta_{aero} + \zeta_{mech}\right)\omega_n\omega\right)}. \tag{7.1}$$

Considering the formulation of the aerodynamic damping ratio given by Equations 4.22 and 4.23, it can be seen that the real (in-phase) component of the damping force is neglected in the decoupled solution. Taking Equations 4.22 and 4.23 into account, Equation 7.1 can be re-written in the form

$$\tilde{q} = \frac{\tilde{f}}{(\omega_n^2 - \omega^2) + \mathbf{i}\left(2\zeta_{mech}\omega_n\omega - d_N^{\Im}\right)} \tag{7.2}$$

illustrating the contribution from the aerodynamic damping force. Here, $d_N^{\Im}$ represents the imaginary component of the aerodynamic damping force normalised by the modal amplitude used in the damping calculation, where

$$\tilde{d}_N = \frac{\tilde{d}^{cfd}}{q^{cfd}}. \tag{7.3}$$

To emulate the coupled solution, both the inertial and viscous components of the decoupled damping force are applied to the right-hand side of the coupled modal

equation (6.1). The normalised damping force provided in Equation 7.3 is scaled by the modal amplitude to yield the damping load for any given response,

$$\tilde{d}(q) = \tilde{q}\left(d_N^{\Re} + \mathrm{i}d_N^{\Im}\right). \tag{7.4}$$

Taking the decoupled aerodynamic forcing and damping loads as excitation terms, the coupled modal equation is resolved to give the analytical solution,

$$\tilde{q} = \frac{\tilde{f}}{\left(\omega_n^2 - \omega^2 - d_N^{\Re}\right) + \mathrm{i}\left(2\zeta_{mech}\omega_n\omega - d_N^{\Im}\right)}. \tag{7.5}$$

This equation describes the decoupled solution with added mass, provided by the inertial damping force component, and is used in this chapter to resemble the coupled solution. This approach is equivalent to the "superposition" method discussed by Schmitt et al. [75], which has been shown to closely resemble the coupled solution for typical cases without significant non-linear damping characteristics.

Based on the decoupled aerodynamic forces calculated at the blade natural frequency, the frequency response curve is extrapolated around the resonant peak using Equation 7.5 to simulate the forced response solution of a fully-coupled system. The coupled response is compared with the decoupled frequency response curve, given by Equation 7.1.

7.3.2 Comparison of Coupling Methodologies

A comparison of the two decoupled methods is made for the Mode 7 resonant crossing point of the NASA Rotor 67 fan case described in Section 5.2. Figure 7.2 shows the two frequency response curves around resonance, where the frequency shift of the decoupled method with added mass is clearly visible. The extrapolated curves are compared with the fully-coupled solutions at a range of frequencies for each of the four modes in Figure 7.3. It can be seen that the decoupled solution with added mass agrees very well with the coupled method, verifying the ability of the decoupled method to predict vibration levels at frequencies slightly different from the solution frequency. This is due to the fact that the aerodynamic solutions do not vary significantly over such a small frequency range; therefore, variation in vibration amplitude is caused primarily by blade structural dynamic effects.

Mode No.	Decoupled Resonant Peak		Coupled Resonant Peak	
	Frequency (Hz)	Tip L.E. Amp. (% Chord)	Frequency (Hz)	Tip L.E. Amp. (% Chord)
1	601.0	1.096	602.29	1.099
2	1307.9	0.691	1307.2	0.688
3	1913.2	0.521	1909.7	0.511
7	4198.4	0.164	4192.0	0.164

Table 7.1: Comparison of decoupled and coupled resonant peaks

Table 7.1 shows the high level of agreement between the resonant peaks of the decoupled and coupled solutions at their respective frequencies. The important point to note is that the exclusion of the added mass effect in the decoupled solution makes little difference in the height of the resonant peak. This is due to the fact that the aerodynamic and structural dynamic behaviour do not vary significantly over such a narrow frequency range. Both aerodynamic excitation and damping forces were found to be insensitive to frequency within the ranges of the resonant peaks. In addition, Srivastava et al. [147] reported that aerodynamic damping varied very little within a surprisingly large frequency range for the 1^{st} bending mode of a transonic fan.

In terms of structural dynamics, the resonant response amplitude for a given excitation source is determined by the level of total viscous damping, which is equal for both approaches. Regardless of whether or not added mass is included, the denominators of the forced response solutions in Equations 7.1 and 7.5 reduce to $i2\zeta_{mech}\omega_i\omega$ at resonance. Therefore, for a given damping ratio, the resonant response amplitude is inversely proportional to the frequency, which does not significantly vary over such a narrow range.

7.3.3 Impact of Frequency Shift

For any single DoF forced oscillator, the phase angle at which the response will lag the excitation force will be very small for low frequencies and will approach 180°

for high frequencies. At resonance, the response will lag the force by 90°, when the maximum work is applied to the blade. The response phase lag is very sensitive to frequency around the resonance and will change very quickly for small deviations around the resonant frequency. In Equation 7.5 it can be seen that resonance occurs when the denominator is purely imaginary, hence $\omega_i^2 - \omega^2 - d_N^{\Re} = 0$. This condition is only seen with excitation at the resonant frequency, since ω_i and $d_N^{\Re}$ do not vary significantly around the narrow resonant peak. The decoupled method simplifies the response solution by neglecting the $d_N^{\Re}$ term, ensuring that the resonant condition of 90° phase lag always occurs at the blade natural frequency.

The flow-structure coupling effect can also have a reduced mass effect, resulting in a positive frequency shift, such as experienced by Mode 1. In fluid-structure coupling applications, added mass is usually considered as a region of fluid attached to the moving solid boundary, which requires an inertial force to accelerate the attached fluid with the structure (Liu [149]). It is evident that this interpretation does not hold for turbomachinery cases, which involve the high speed flow of low-density fluids with thin boundary layers and often include shock oscillation. The apparent inertial force results from the phase of the complex flow phenomena acting on the blade in relation to the mode shape displacements, rather than the physical oscillation of an attached region of fluid. However, it is now shown that the vibration-induced aerodynamic force component which is in phase with the blade motion can be considered as an added (or reduced) mass for blade forced response analysis.

7.4 Decoupled Prediction of Frequency Shift

In this section, it is shown how a single decoupled solution can be used to accurately predict the resonant peak with the option of either including or disabling the blade added mass effect. An evaluation of the added mass effect and the implications of the frequency shift on the coupled solution are presented, starting with a comparison of the frequency shift due to viscous damping and the added mass effect. It is well known that the damped resonant frequency due to viscous damping ω_d is given by

$$\omega_d = \omega_n \sqrt{1 - \zeta_{tot}^2}. \tag{7.6}$$

The dynamic resonant frequency due to the added mass effect alone is calculated by considering the added mass in terms of the inertial damping force component. The decoupled modal equation with added mass (Equation 7.5) is written in the form

$$\left\{-\omega^2\left(1+\frac{d_N^{\Re}}{\omega^2}\right)+\omega_n^2+\mathbf{i}\left(2\zeta_{mech}\omega_n\omega-d_N^{\Im}\right)\right\}\tilde{q}=\tilde{f} \tag{7.7}$$

it is evident that the dynamic mass, m', of the system at resonance can be given by the expression

$$m'=1+\frac{d_N^{\Re}}{\omega^2}. \tag{7.8}$$

The dynamic natural frequency, ω_{dyn}, is therefore given in terms of dynamic mass by

$$\omega_{dyn}=\sqrt{\frac{\omega_i^2}{m'}} \tag{7.9}$$

where ω_n^2 is the modal stiffness. To avoid the simultaneous solution of Equations 7.8 and 7.9 at the unknown frequency ω_{dyn}, the excitation frequency, ω, in Equation 7.8 can be substituted for the blade natural frequency, ω_i, since the frequency shift is relatively low.

Based on the decoupled damping calculation, the frequency shifts due to the viscous damping and added mass effects given by Equations 7.6 and 7.9 are compared for each of the four modes of the NASA Rotor 67 case. The calculated frequency shifts for the four modes listed in Table 7.2 show that the added mass effect dominates the viscous damping effect by 2-3 orders of magnitude. It can therefore be deduced that the frequency shift can be considered to be solely determined by the added mass effect.

7.5 Coupled Prediction of Frequency Shift

Unlike the decoupled method, a single coupled calculation can not be used to extrapolate the frequency response function, therefore the resonant peak can not be identified based on the solution at any one frequency. This is due to the fact that the aerodynamic excitation and damping forces are combined and can not be separated,

Mode No.	Frequency Shift, $\Delta\omega_d$(Hz)	
	Viscous Effect	Inertial Effect
1	-0.0041	+1.31
2	-0.0011	-0.728
3	-0.0309	-3.32
7	-0.00493	-6.383

Table 7.2: Frequency shift due to viscous and inertial damping force components

resulting in the need for multiple solutions to find the resonant frequency. The aerodynamic modal forces of the Mode 3 solution are plotted on the Argand diagrams in Figure 7.4, together with the response phase angles for a range of frequencies around resonance. For simplicity, no mechanical damping is present. To clarify the terminology, the damping force refers to the total vibration-induced aerodynamic force, consisting of the "viscous" out-phase component and the "inertial" in-phase component. The excitation force is due to incoming aerodynamic disturbances and is independent of blade motion; and the combined force is the sum of the aerodynamic damping and excitation forces. It can be seen that the excitation force remains constant over the narrow resonant frequency range and the damping force lags the blade motion with constant relative phase. An important point to note is that the resulting combined aerodynamic force is zero only when solved at the natural frequency, at which point the aerodynamic damping force exactly balances the excitation force.

Figure 7.5 shows the variation of the combined excitation and damping aerodynamic force with solution frequency for Mode 3 when mechanical damping is both included and excluded. At the natural frequency, the combined aerodynamic force is equal and opposite to any mechanical damping force. For solutions outside the natural frequency (including the resonant frequency), the resulting combined aerodynamic force is always non-zero and in phase with the blade motion, and hence this resultant force does not do any work. The only unique feature to be observed at resonance is the exactly 90° phase lag of the blade motion behind the excitation force. An important point to note is that this exact phase relation is assumed by

the decoupled method at the natural frequency. Since only the combined force is available, the phase of the excitation force can not be determined, hence, the response phase remains unknown. Outside the natural frequency, no deductions can be made from the combined force, which is non-zero in magnitude and always in phase with blade motion. Therefore, due to the lack of knowledge of the individual damping and excitation forces, a single coupled solution at a given excitation frequency can not be used to predict the response for any other frequency. Hence, multiple solutions in the form of a frequency sweep or a frequency tracking routine are needed to predict the peak response of the coupled solution due to the existance of the frequency shift.

7.6 Sensitivity to Frequency Shift

When choosing between a coupled or decoupled forced response analysis for a particular case, a consideration is the sensitivity to the added mass effect, which will determine the level of agreement between the coupled solutions at the blade natural frequency and the resonant peak. A coupled solution at the natural frequency will provide a vibration amplitude close to the resonant peak for cases that are insensitive to frequency shift, whilst the more sensitive cases require resonance tracking. Whilst it has previously been shown that the frequency shift is caused by the inertial aerodynamic damping component, the sensitivity of the coupled solution to frequency shift depends on the sharpness of the resonant peak, which is determined by the overall system damping.

A generalised approach is presented to evaluate the accuracy in which a single coupled solution at the blade natural frequency approximates the resonant peak for cases subject to aerodynamic and mechanical damping. As shown in Equation 7.5, the coupled solution can be emulated by considering both the inertial and viscous terms of the decoupled aerodynamic damping force, where the magnitude of the coupled solution is given by

$$|\tilde{q}_{cpl}| = \frac{|\tilde{f}|}{\sqrt{\left(\omega_n^2 - \omega^2 - d_N^{\Re}\right)^2 + \left(2\zeta_{tot}\omega_n\omega\right)^2}}. \tag{7.10}$$

Similarly, the magnitude of the decoupled solution from Equation 7.2 is given by

$$|\tilde{q}_{dec}| = \frac{|\tilde{f}|}{\sqrt{\left(\omega_n^2 - \omega^2\right)^2 + \left(2\zeta_{tot}\omega_n\omega\right)^2}}. \tag{7.11}$$

The validity of representing the resonant peak amplitude by the decoupled solution at the natural frequency was shown in Table 7.1. With forcing at the natural frequency, an expression for the accuracy of the coupled solution is given by the ratio of the coupled and decoupled solutions,

$$\frac{q_{cpl}}{q_{dec}} = \frac{2\zeta_{mech}\omega_n^2 - d_N^{\Re}}{\sqrt{\left(d_N^{\Re}\right)^2 + \left(2\zeta_{mech}\omega_n^2 - d_N^{\Re}\right)^2}} \tag{7.12}$$

Representing the aerodynamic damping force components in terms of phase lag behind the modal displacement as $d_N^{\Re} = d_N \cos(\theta)$ and $d_N^{\Im} = d_N \sin(\theta)$, and taking r as the ratio of mechanical to aerodynamic damping

$$r = \frac{\zeta_{mech}}{\zeta_{aero}} \tag{7.13}$$

results in an expression for the accuracy of the coupled solution at the blade natural frequency in terms of the phase lag, $-\theta$, of the aerodynamic damping force:

$$\frac{q_{cpl}}{q_{dec}} = \frac{(r+1)\sin(-\theta)}{\sqrt{[\cos(-\theta)]^2 + [(r+1)\sin(-\theta)]^2}}. \tag{7.14}$$

Shown in Figure 7.6 is an indication of the sensitivity of the fully coupled solution at the blade natural frequency to the coupling effect. Plotted on the graph is the agreement between the coupled solution and the decoupled resonant peak given by Equation 7.14, against the phase lag $-\theta$ of the aerodynamic damping force. The magnitude of the aerodynamic damping force remains fixed and the phase lag is varied. The $\frac{q_{cpl}}{q_{dec}}$ ratio is plotted for values of $r = 0, 1,$ and 2 to show the influence of mechanical damping.

Included on the graph are the coupled solutions of the four modes, repeated with varying levels of mechanical damping. The coupled solution is insensitive to the frequency shift for cases with a damping force phase lag close to 90° where the inertial damping force component is small, but such cases are not common in reality. Cases with a higher inertial component become more sensitive due to the increase

in frequency shift. Mechanical damping plays an important role in the sensitivity to frequency shift by influencing the sharpness of the resonant peak. For cases subject to very low mechanical damping, the sensitivity is high, and the inclusion of mechanical damping can dramatically reduce the sensitivity of the system.

It is shown that the coupled solution at the natural frequency can predict the resonant peak with reasonable accuracy for cases with significantly high mechanical damping or when the aerodynamic damping force phase lag is known to be close to 90°. For example, the coupled solutions for the four modes predict the resonant peak with 95% accuracy when the mechanical damping ratio is set to be twice that of the aerodynamic damping. However, it has been shown that the phase of the aerodynamic damping force can vary significantly for each individual mode and the position any particular case on the graph can not be determined without knowing the aerodynamic damping forces. Therefore, it can be dangerous to assume that a single coupled solution will accurately predict the resonant peak for cases where mechanical damping does not dominate.

Whilst mechanical damping prediction methods are immature, the work of Ning et al [51], indicates that mechanical damping of typical compressor blades without friction dampers is greatly reduced for high-order modes, where blade motion is concentrated within the aerofoil. It can therefore be deduced that the sensitivity to frequency shift is likely to be high for bladerow interaction problems, where high-order modes result in low mechanical damping. It has been shown that the aerodynamic damping forces induced by high-order modes can produce high inertial components, which further highlights the potential for high sensitivity in such cases.

It has been demonstrated that the coupled method can significantly under-predict the resonant peak when solved only at one frequency for any lightly-damped blade, with a particular emphasis on high-frequency bladerow interaction problems. The decoupled method correctly assumes a 90° phase lag of the modal response behind the modal excitation force and has been shown to be insensitive to solution frequency for a range of frequency shifts that are likely to be encountered.

7.7 Summary

In the previous chapter, it was shown that decoupled systems can accurately predict resonant vibration amplitudes from a single calculation at the blade natural frequency, whilst fully-coupled forced response solutions are subject to a shift in resonant frequency, thus requiring multiple solutions. This chapter investigates the mechanics behind the flow-structure coupling effect, providing an explanation of the cause of frequency shift and an evaluation on the implications of frequency shift for decoupled and fully coupled methods.

The decoupled method is modified in order to simulate the coupled solution, providing an analytical solution to the coupled frequency response curve from a single decoupled solution. A study into the fluid-structural coupling effect identified the source of the frequency shift in the coupled solution to be due to the inertial effect of the aerodynamic damping force causing a change in the blade dynamic mass. Conversely, the decoupled method simplifies the solution by neglecting the inertial damping force component, thus eliminating the cause of the frequency shift. Any shift in frequency caused by the effect of viscous damping is shown to be negligible.

It is not possible to predict resonance from a single coupled solution at any frequency; hence coupled methods must rely on multiple solutions to find the resonant peak. A investigation into the sensitivity of coupled solutions to frequency shift shows that the need for resonance tracking with coupled methods is especially important for high-frequency bladerow interaction problems, where low mechanical damping and strong fluid-structure coupling effects are likely to be encountered. The decoupled method is identified as the preferred approach to bladerow interaction problems due to the ability to accurately predict the resonant peak with high efficiency from a single solution.

7.8 Figures

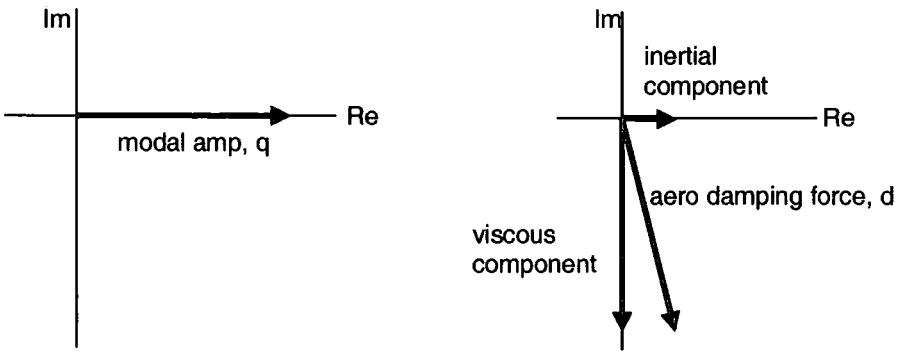

Figure 7.1: Argand diagrams of modal amplitude of vibration-induced complex modal damping force

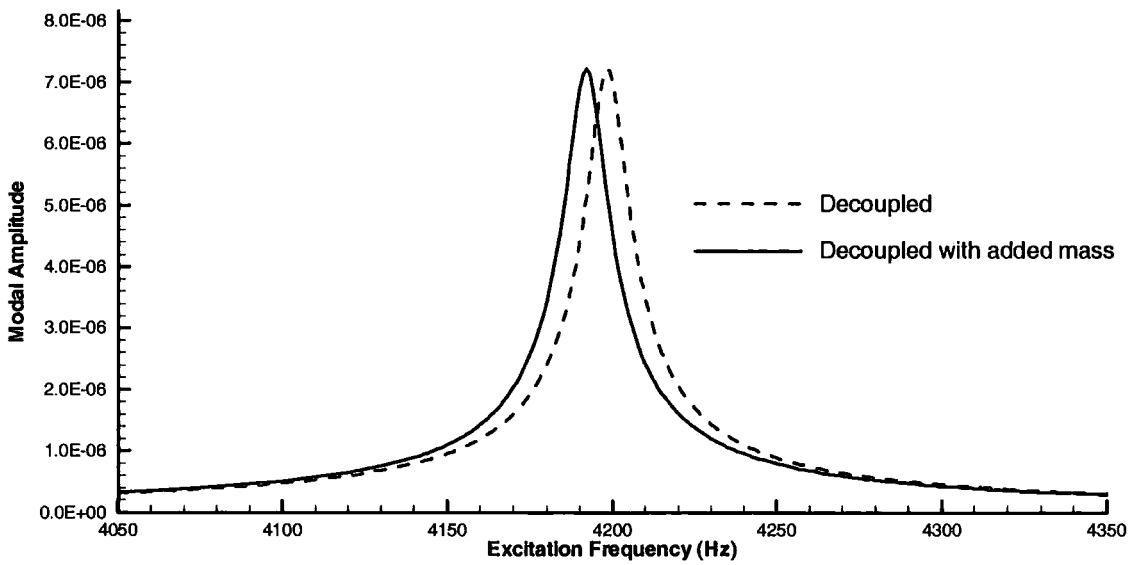

Figure 7.2: Frequency response curves for Mode 7

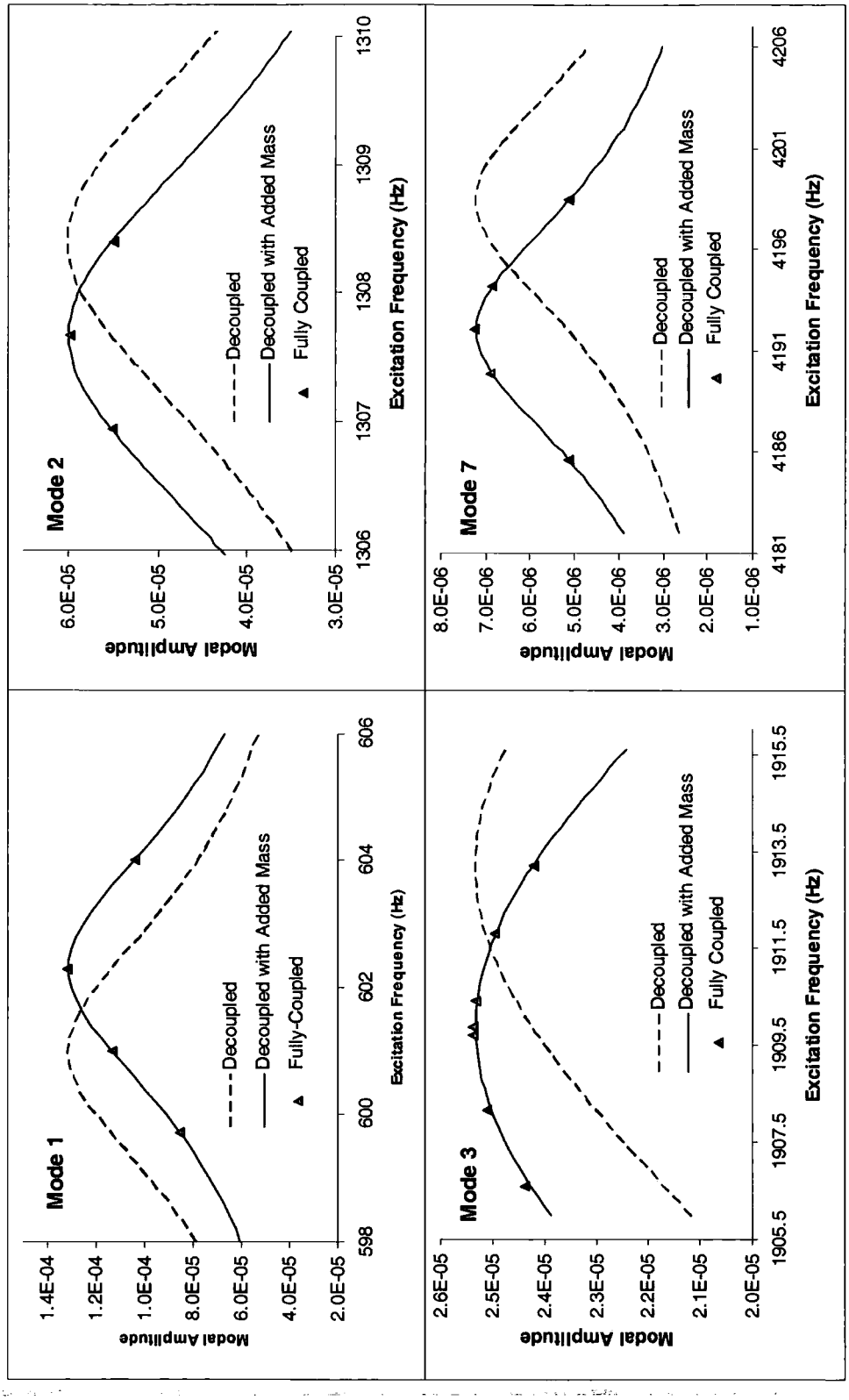

Figure 7.3: Frequency response curves for coupled and decoupled calculations

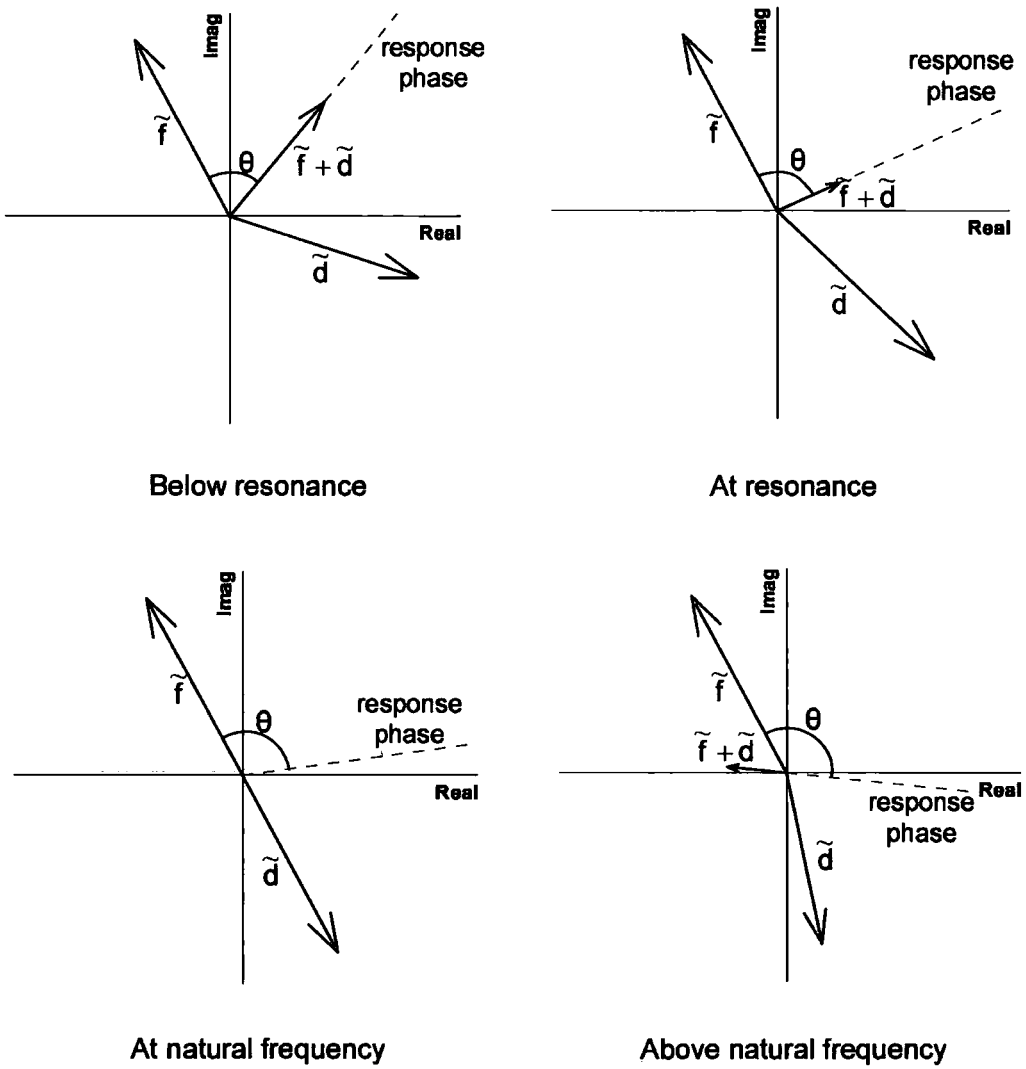

Figure 7.4: Argand diagrams of forces at solutions around resonance for Mode 3

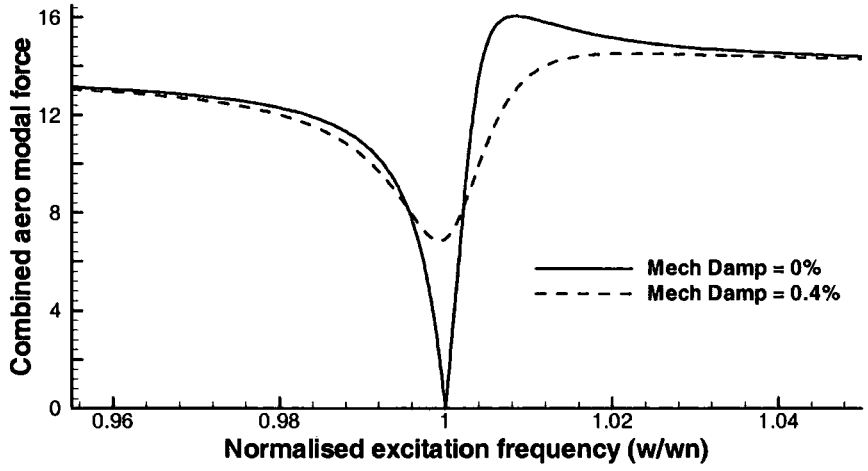

Figure 7.5: Variation of combined excitation and damping aerodynamic force with excitation frequency

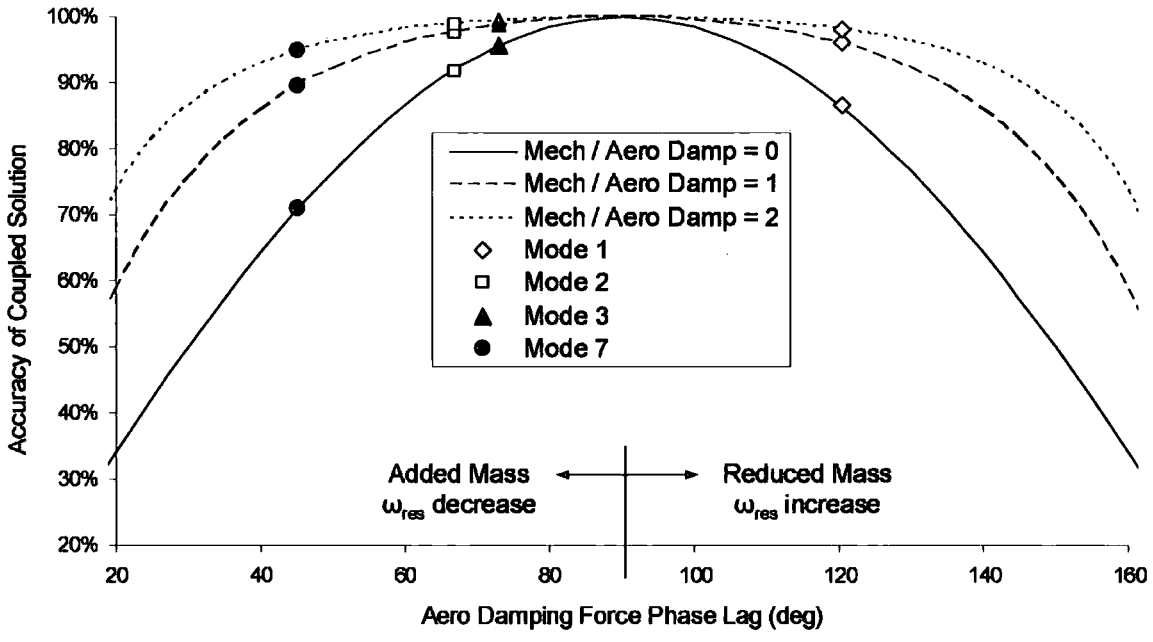

Figure 7.6: Sensitivity of coupled solutions at natural frequencies to fluid-structure coupling effect

Chapter 8

Friction Damping Analysis

8.1 Introduction

A new approach to friction modelling for use with the finite element method was introduced in Section 3.3 which was developed to provide the maximum compatibility with the existing methods and models used in the aeromechanical forced response analysis. As for the forced response system, the friction damping methodology has been developed with industrial blade designers in mind. The friction damping prediction tool was therefore subject to the following wish list:

- low solution times
- minimal modification of existing FE models
- compatibility with modal solution of the aeromechanical forced response system
- low user interaction
- decoupled friction calculation from FE solution
- ability to deal with the range of vibration amplitudes typical of turbomachinery blade forced response

The intention of the friction damping analysis is to model the friction behaviour of an FE model using a modal approach to linearise the friction damping, allowing

ease of use with the existing modal forced response system. The displacements of the contact surfaces are incorporated into the blade modes by linearising the 3D contact flexibility of the root-slot interface. An initial static analysis is performed to establish the regions of the blade root under compressive contact load due to static centrifugal and fluid loading, together with the compressive contact pressures. A modal analysis is performed to yield the modal displacements of the friction surfaces. The absolute tangential contact displacements for a single mode are then obtained at a specified modal amplitude, from which the friction forces are derived using three distinct friction models: a) a Rigid Coulomb model; b) an Elastic Coulomb model; and c) an advanced Microslip model. The friction forces are integrated over one vibratory cycle to give the damping work per cycle, which is used to calculate an equivalent viscous damping ratio for the specified modal amplitude.

8.1.1 Conventional FE approach

Conventional friction modelling approaches in FE analysis are based on non-linear time-marching to deal with the non-linear nature of the contact mechanics. The standard FE modelling approach within ANSYS is to represent the friction surfaces as two separate bodies, connected by tetrahedral contact elements. Contact is established by a non-structural contact element, where the base is connected to one body and the tip is connected to the second body. Contact occurs when the surfaces of the bodies penetrate, causing the tip of the tetrahedron to penetrate its base, effectively turning the element inside-out. When this condition is reached, the contact forces are applied by the element to the connecting nodes on the bodies. This procedure is repeated for each time step in the solution. A friction damping analysis in the time-domain can possibly be done in one of two ways. The first possible approach is to set an initial deformation of the blade in the mode shape of interest, then start the transient analysis from the point when the blade is released. The rate of decay of the blade motion over the relevant vibration amplitude can be used to derive the modal damping ratio. The second possibility is to introduce friction contact loads into a full time-accurate aeroelastic forced response solution. Based on the existing frequency domain CFD solver, the harmonic fluid excitation and damping forces are

reconstructed on a FE model at each time step of the solution to be considered with the friction forces to forcing terms in the structural equations. The aerodynamic damping forces are continually updated and the solution is run to a steady state, yielding the forced response solution.

The conventional approach to FE friction modelling, however, does not meet up very well to the requirements listed in the bullets above. The need for time-marching significantly increases the computational time of the solution. This is not only due to the need to solve the model at a large number of discrete time steps, but the time-accurate results gained for one particular condition are not easily transferred to a different condition. This suggests that a separate time accurate solution will be required for each mode, which is likely to be computationally expensive. Conventional contact approaches involve the complexities of including a second body connected by an interface mesh of contact nodes, which is not desirable to a designer whose primary interest is blade aeromechanics rather than root friction. Such an approach may be time-consuming, and automated mesh generation may be difficult to program. The solution of the FE model in the time-domain does not fit in with the existing strategy of solving the aeromechanical analysis in the frequency domain. It is desirable to keep to one frequency-domain approach in order to maintain continuity in the analytical models and to avoid possible complexities when passing information between the friction and aeroelastic calculations. A full transient forced response analysis with aerodynamics seems pointless when an analytical solution can be achieved in the frequency-domain. The current capability of ANSYS is to model Coulomb friction only and the inclusion of a microslip model may not be easily achievable using standard ANSYS capabilities. The new method introduced in Chapter 3 overcomes the problems outlined above for a standard friction analysis by providing a CPU-efficient alternative, based in the frequency domain that is implemented with a high level of automation.

8.1.2 Overview of Adaptive Constraint Method

A new method of friction damping prediction, the *Adaptive Constraint Method*, is therefore proposed that uses the existing linear static and modal solvers of ANSYS

to model the non-linear behaviour of the friction surfaces. The Adaptive Constraint Method is named as such since it models the non-linear contact mechanics using the linear solvers in an iterative manner by adapting the model constraints to match the non-linear characteristics of the contact regions for the relevant displacement levels. Contact is modelled using a series of linear springs attached to ground, the stiffnesses of which are adjusted to account for contact/non-contact, normal contact stiffness, tangential contact stiffness and tangential friction forces. The analysis is based on an initial static analysis to determine the regions of the root in compressive contact resulting from blade centrifugal and steady fluid loads. A subsequent modal analysis provides the mode shape at the friction surfaces, taking the non-linear tangential properties into account. The contact modeshape and modal amplitude define the contact displacements, allowing the modal damping ratio to be calculated. The method allows either the Coulomb or microslip friction models to be implemented within ANSYS for a given blade vibration amplitude to provide a friction damping ratio independently to the forced response calculation.

8.2 Methodology

8.2.1 Integration with decoupled forced response system

The Adaptive Constraint Method calculates the normal contact pressures and modal contact displacements on a linearised FE model, which are used in the friction damping calculation to provide the damping at the specified level of blade vibration. Friction damping is calculated based on a detailed modal analysis of the blade root, in a separate analysis to the modal analysis used for the blade aeroelastic forced response calculation. It is assumed that the root friction forces at the root do not significantly affect the mode shapes and frequencies of the aerofoil due to the high relative stiffness of the blade structure.

Due to the non-linear variation of friction damping with vibration amplitude as discussed in Section 3.3, the damping ratio must be calculated simultaneously with the forced response solution. In other words, a degree of coupling is always required between the calculation of the forced response amplitude and the friction damping

ratio. Figure 8.1 illustrates how the friction calculation is intended to be incorporated into the existing decoupled forced response method. The forced response solution is firstly calculated using the decoupled aerodynamic forcing and damping terms without mechanical damping or using an assumed value. The resulting modal amplitude is subsequently passed to the Adaptive Constraint Method, which returns the friction damping ratio.

8.2.2 Finite Element representation of friction contact

Friction contact is modelled on the ANSYS FE mesh by a series of linear springs connecting the blade root to ground to represent the 3-D contact stiffness of the root-slot interface. The friction contact is modelled at each node on the interface, as shown in Figure 8.2. Three perpendicular springs are attached to each node on the root flank surfaces to represent the contact with the slot in the manner shown in Figure 8.3. The spring endpoint nodes are fully restrained, effectively neglecting the flexibility of the disk material. The two springs aligned on the surface plane represent the tangential stiffness acting on the node in the friction plane, whilst the spring normal to the surface represents the normal contact stiffness under a compressive normal load. The spring elements are applied to all nodes on the root surface that are likely to be in contact with the slot. The actual root surface nodes in contact due to the applied static load are identified as part of the static solution.

The normal and tangential contact stiffness of the springs are derived from the semi-analytical microslip model given by Olofsson [130]. The stiffness values are varied in the solution to account for the effect of static loading on the friction interface. Contact stiffness is dependent on the compressive load transmitted through the contact interfaces. Consequently, the static load distribution over the contact surfaces is affected by the normal stiffness of the contact regions.

An important property of the contact interface is the inability to transmit tensile loads. Any contact nodes on the root surface that result in tensile contact loads are identified to be out of contact and subsequently have the contact spring elements disabled. An iterative approach is therefore adopted to identify the contact nodes and resolve the contact parameters.

8.2.3 Adaptive Constraint Method

The solution of the FE model is performed using ANSYS in two stages: an iterative static analysis and a single modal analysis, as shown in Figure 8.4.

Static analysis

The static analysis identifies the areas of the blade root transmitting the compressive reactions to the centrifugal and steady fluid loading, and determines the contact stiffness values based on the normal contact pressures. When setting up the FE model, it is not valid to simply assume that the entire upper surfaces of the root flanks remain in contact and transmit a compressive contact load, whilst the lower and side surfaces of the flanks remain out of contact. Due to the fluid shear and moment loading of the blade and the deformation of the flanks from centrifugal loading, complex reaction load distributions result over the upper, side and lower surfaces of the root flanks. Based on the current linear representation of the contact mechanics, it is not possible to determine which regions transmit reaction loads using a single static analysis. The static analysis is therefore performed iteratively to identify the nodes under compressive normal loading and to determine the pressure-dependant normal pressures and tangential contact stiffness values used in the modal analysis and friction models.

The static analysis assumes a dither effect, where all reaction loads are transmitted in the normal direction to the contact surfaces with no tangential contribution. This assumption is based on the relatively high normal stiffness, which is typically 2 orders of magnitude greater than the tangential stiffness. The dither condition is ensured by reducing the stiffness of all tangential springs to a very small value for the static analysis.

The first iteration is done using estimated values of normal spring stiffness values based on an estimated average contact pressure. The details for determining the spring stiffness values are dependant on the particular friction approach chosen and are discussed later in Section 8.3.2. The rotational velocity and steady fluid loads on the blade are applied and the ANSYS static structural solver is executed. The static contact loads are given by the reactions at the endpoint nodes of the normal

spring elements. The normal contact pressures are then given by the product of each reaction force and the effective nodal area of the surface node, which is intrinsically calculated by ANSYS.

The resulting sign of the normal pressure determines whether the node is in contact with the disk. Nodes with negative normal pressure correspond to contact loads in tension, and can not be sustained. Such nodes are flagged to be out of contact and subsequently have the adjoining spring elements set to a very small value, thus eliminating the tensile contact. The reason a small value is used, rather than zero is to maintain the ability to detect contact pressures in the subsequent iterations, and to avoid numerical problems with the FE matrices.

Nodes associated with positive normal pressures are in compressive contact and have the normal spring stiffness maintained. Such contact nodes are flagged as active. Normal contact stiffness is calculated as a function of the normal load, and the normal stiffness values of the active normal springs are updated accordingly.

The static solution is redone using the updated spring properties and the process of activating and deactivating the contact nodes is repeated until convergence is achieved. The result of the static analysis is the compressive normal pressures of all active contact nodes.

Modal analysis

The modal analysis is done after the converged static solution. The rotational velocity and steady fluid loads are removed and the prestressing terms from the static solution are enabled. Tangential spring stiffness is now applied to the active contact nodes in addition to the existing normal stiffness. The values of tangential stiffness are calculated based on the normal pressures. Surface nodes identified as inactive, non-contact nodes have the normal and tangential spring stiffness values set very small. A single execution of the modal solver yields the modeshapes of the blade at the active contact nodes.

8.2.4 Friction damping calculation

Whereas the FE modelling of the contact mechanics is based on a linearisation of the contact flexibility, the friction damping calculation considers the non-linear displacement-force behaviour. The friction damping coefficient is therefore calculated for a given modal amplitude of a particular mode, based on the normal pressures and friction modeshape from the FE analysis. For each node, the local friction work is calculated over one vibratory cycle using either of the Coulomb or microslip friction models outlined in Section 3.3, which give the friction work in Equations 3.19, 3.27 and 3.39. The work contribution of each node is then summed to give the total friction work done on the blade. The modal friction damping ratio is given by Equation 3.20 based on the principle of equivalent viscous damping.

8.3 Implementation

8.3.1 Case description

The friction calculation is performed on the Siemens transonic compressor blade described in Section 5.3. A detailed view of the FE mesh blade root is given in Figure 8.2, which shows the four flanks providing the radial location in the disk slot. The normal and tangential constraint of the flank surfaces is done by spring elements connecting the root to ground using the Adaptive Constraint Method. Axial location is provided by the lip on the front edge of the fir tree section, which is fully constrained on the FE model. The FE mesh, originally constructed from Solid95 quadratic elements, is converted to Solid45 linear elements to eliminate the mid-side nodes of the Solid95 elements, which are not suitable for contact analysis. The shape functions of the quadratic Solid95 elements result in negative stiffness values being associated with the mid-side nodes, giving incorrect contact pressures.

The friction damping ratios are evaluated for Modes 8, 9 and 10 at the measured forced vibration amplitudes. This allows the predicted friction damping ratios to be compared with the values implied by the forced response results, thus providing an initial verification of the friction model.

8.3.2 Calculation of contact stiffness

The values of normal and tangential contact stiffness are derived from the microslip friction model reported by Olofsson [130]. Two approaches to implementing the Adaptive Constraint Method are presented, which represent the friction behaviour in terms of the Coulomb and microslip models.

Coulomb friction analysis

The Coulomb friction model adopts constant values of normal and tangential spring stiffness to represent the average contact properties over the whole contact area. This approach demonstrates how the contact stiffness parameters can be be derived either from experimental data or from a simple empirical or semi-analytical model.

The average contact pressure of the Siemens blade is calculated from the blade centrifugal reaction load and the estimated contact area to give an estimated normal contact pressure of $P_n = 160MPa$. The tangential stiffness has been derived from experimental data by Olofsson [130] and is obtained from the displacement-friction load graph in Figure 9 of Olofsson [130]. This graph is based on the model described in Section 3.3.2 and refers to stainless steel on stainless steel at a normal pressure of $125MPa$ with contact parameters of $C = 1.0 \times 10^{10}$ contacts$/m^2/m$, $R = 10.0\mu m$ and $\mu = 0.122$. These values represent contact properties typical of unlubricated engineering surfaces, and the case corresponds well with the conditions of the blade root interface in terms of pressure and materials. Figure 8.5 shows how the tangential stiffness is calculated from the graph of Olofsson. The stiffness is taken as the gradient of the graph for the initial linear part of the microslip curve, giving a tangential stiffness of $2.09 \times 10^{12} N/m^3$.

Normal stiffness is taken as a factor of the tangential stiffness. It is discussed in the friction literature that the ratio of normal to tangential stiffness is commonly around 100 for machined metal surfaces. A value of $\frac{P'_n}{P'_t} = 100$ is therefore used to define the normal stiffness.

The influence of the contact parameters on the Elastic Coulomb damping predictions is investigated by repeating the calculations using a range of values in a parametric study. The calculations are repeated with the following variations:

Contact stiffness (constant $\frac{P_n'}{P_t'}$) $P_t' = 2.09 \times 10^{11} N/m^3,\ 2.09 \times 10^{13} N/m^3$

Normal contact stiffness $\frac{P_n'}{P_t'} = 10,\ 1000$

Friction coefficient $\mu = 0.2$

The influence of the vibration amplitude on the predicted damping is also investigated by repeating the Elastic Coulomb calculation at a range of modal amplitudes.

Microslip friction analysis

The microslip analysis uses the semi-analytical solution of Olofsson [130], to determine the normal and tangential contact stiffness as functions of normal pressure, thus removing the assumption of constant stiffness properties made in the Coulomb analysis. The microslip model uses the same parameters used to produce the graph used in the above Coulomb friction approach, corresponding to Figure 9 of Olofsson. A summary of the microslip parameters is given as

Surface contact parameter $C = 1.0 \times 10^{10}$

Spherical asperity radius $R = 10\mu m$

Friction coefficient $\mu = 0.122$

Young's modulus of elasticity $E = 210GPa$

Shear modulus $G = 81GPa$

Poisson's ratio $\nu = 0.3$

The initial static analysis is performed using an average normal contact stiffness in an identical manner to the Coulomb approach discussed previously. The stiffness of each normal contact spring element in compression is then calculated at each subsequent step, given by

$$k_n = \frac{P_n A_0}{z} \tag{8.1}$$

Here, z is the normal deflection of the surface node, given by Equation 3.32, under the resulting normal pressure, P_n; and A_0 is the effective nodal area of the surface node calculated by ANSYS. The stiffness values of the compressive springs are updated and the tensile springs are deactivated before the static solution is repeated.

Once the static analysis has reached convergence, the tangential stiffness properties are calculated for use in the modal analysis. The tangential stiffness is calculated for each point in contact using the static normal pressure. Due to the non-linear variation of friction force with tangential displacement, an equivalent linear stiffness is derived for each active contact node. As shown in Figure 3.16, the equivalent tangential stiffness is calculated at a defined position along the microslip curve. The equivalent tangential stiffness is therefore given by the expression

$$k_t = \frac{F_f}{x} \tag{8.2}$$

where F_f is the microslip friction force given by Equation 3.34 at the specified tangential displacement, x. The tangential displacement is specified as a fraction of the of the slip displacement, x^{lim}, which is given by Equation 3.35. A value of $\frac{x}{x^{lim}} = 0.5$ is used as the datum value in the following friction calculations. In a second analysis, the values of $\frac{x}{x^{lim}}$ are varied for the Mode 8 calculation to assess the influence on the predicted friction.

8.4 Results

8.4.1 Implied friction damping from forced response analysis

In Section 5.3.2, the expected friction damping ratios of the three modes were calculated by subtracting the predicted aerodynamic damping from the measured system damping. The expected friction damping ratios are listed in Table 5.7, showing a value of 0.24% for Mode 8, whilst Modes 9 and 10 provide little or no friction damping. This expected behaviour is characterised by the mode shape plots in Figure 5.13, where a significant level of root motion can be seen for Mode 8, whereas the root motion of Modes 9 and 10 is much lower.

8.4.2 Coulomb friction results

Static results

The convergence of the static contact analysis was reached in four steps, yielding the compressive contact pressures for the contact nodes identified as active. Figure 8.6 plots the nodal reaction loads of each ANSYS static solution at each of the four steps in the solution. The x-axis on each graph represents the node number of each contact node, the ordering of which is arbitrary. The y-axis represents the contact pressures, with negative values being compressive. It can be seen that the normal stiffness for nodes in tensile contact are deactivated at the end of each step, thus changing the distribution of the contact loads, and causing a small amount of oscillation in the overall solution. Starting with normal stiffness applied to all 430 nodes around the root flanks, the number of active nodes at the end of the static analysis is reduced to 204. The static contact analysis was repeated from a different starting point, with only the nodes on the upper surfaces of the root flanks being activated. The second analysis produced an identical end result, demonstrating that the convergence is independent of starting point.

Modal result

Tangential spring stiffness is then applied to the springs of the active contact nodes for the modal analysis. The resulting first 15 natural frequencies of the modal analysis are plotted in Figure 8.7, together with the frequencies of the fully-constrained root model used to provide the aerofoil modes in the forced response calculation. The results of an additional analysis are included, where the modal analysis is done without tangential stiffness to demonstrate the behaviour of freely-sliding contact. Figure 8.8 compares the mode shape contours of three models. The comparison of the elastic contact model with the original fixed root model shows that the natural frequencies of the high-order modes vary a small amount with the change in root constraints. However, the frequencies of the freely-sliding root model show significant differences. The largest difference is the apparent addition of a new 10^{th} mode, characterised by the longitudinal vibration of the root along the slot due to the lack

Mode	Modal Amplitude	Expected ζ_{fric}	Rigid Coulomb ζ_{fric}	Elastic Coulomb ζ_{fric}
8	5.519×10^{-7}	0.24%	22%	0.0027%
9	5.70×10^{-7}	0.03%	5.9%	0.0000%
10	1.713×10^{-7}	nil	40%	0.0001%

Table 8.1: Rigid and Elastic Coulomb friction damping predictions

of tangential constraint at the flank surfaces. This high level of mode shape sensitivity demonstrates the importance of modelling the root contact mechanics with the greatest possible accuracy.

The tangential displacement amplitudes at the contact surfaces for the three modes at the forced response solution modal amplitudes are shown in Figure 8.9. Here, it can be seen that the contact motion of Mode 8 is an order of magnitude higher than Modes 9 and 10, agreeing well with the expected behaviour.

Friction calculation

The friction damping ratio of each mode is calculated using the Rigid Coulomb and Elastic Coulomb models, based on $\mu = 0.122$, $\frac{P'_n}{P'_t} = 100$ and $P'_t = 2.09 \times 10^{12}$. The actual tangential displacements of each mode are gained from the product of the contact surface mode shape and the modal amplitude of the forced response solution. A summary of the friction results is given in Table 8.1, where the Rigid and Elastic calculations can be seen to give remarkably different predictions. The Rigid coulomb model predicts unrealistically high damping – especially for Mode 10, where a 40% damping ratio is predicted instead of the expected 0%. Conversely, the Elastic Coulomb model predicts virtually no damping for all three modes.

Figure 8.10 shows the tangential displacement of each active friction contact node, normalised to the elastic limit of the Elastic Coulomb model. Here, it can be seen that only two nodes of a possible 204 active nodes achieve slip in the elastic calculation. The Elastic Coulomb damping equation (Equation 3.28) states that damping work can only be done by nodes in slip, therefore neglecting the contributions from the 99% of active contact nodes that remain within the elastic limit.

However, it is observed in practical applications that contact regions that do not achieve gross sliding still contribute to friction damping due to microslip. It is therefore apparent that the root contact displacements are generally too small to be effectively modelled using the Elastic Coulomb approach.

The rigid model takes the opposite extreme by assuming that the all the tangential motion from every active node provides the maximum contribution to damping for a given friction damping ratio. This approach vastly overestimates the contributions from the regions with small-scale displacements, which make up the bulk of the contact surfaces.

The behaviour of the Coulomb models for small displacements was illustrated previously in Figures 3.5 and 3.9 for a simple 1 DoF case. Figure 3.5 shows that very high damping ratios are predicted by the Rigid Coulomb model for very small displacements. Whilst the Rigid Coulomb work increases linearly with displacement amplitude, Equation 3.20 dictates that the damping ratio increases inversely proportionally with the square of displacement amplitude. For very small displacements, the squared term in the denominator dominates and the damping ratio becomes very large, as seen in the case above. For the Elastic calculation, Figure 3.9 shows that the damping work, and hence damping ratio is zero for displacements within the elastic limit. Since 99% of the nodes in the above elastic calculation remain within the elastic limit, the resulting damping ratio is very small.

Sensitivity to contact parameters

A parametric study was performed in order to investigate the sensitivity of the friction predictions to the input friction contact parameters. The variation in the predicted modal damping ratios with the contact stiffness is given in Table 8.2, where the ratio of normal-tangential contact stiffness is held constant. Whilst the friction is underpredicted, it can be seen that the stiffer contact stiffness gives higher damping values. The higher tangential stiffness results in a reduced elastic limit, allowing more nodes to achieve slip and contribute to damping.

Table 8.3 shows the variation of predicted damping with normal stiffness, which is specified by varying the normal-tangential stiffness ratio, $\frac{P'_n}{P'_t}$, for a constant P'_t.

Mode No.	Expected ζ_{mech}	Predicted ζ_{mech}		
		$P'_t = 2.09 \times 10^{11}$	$P'_t = 2.09 \times 10^{12}$	$P'_t = 2.09 \times 10^{13}$
8	0.24%	0%	0.0027%	0.0082%
9	0.03%	0%	0%	0%
10	0%	0%	0.0001%	0.050%

Table 8.2: Variation of predicted Elastic Coulomb friction damping with contact stiffness

Mode No.	Expected ζ_{mech}	Predicted ζ_{mech}		
		$\frac{P'_n}{P'_t} = 10$	$\frac{P'_n}{P'_t} = 100$	$\frac{P'_n}{P'_t} = 1000$
8	0.24%	0.037%	0.0027%	0%
9	0.03%	0%	0%	0%
10	0%	0.02%	0.0001%	0%

Table 8.3: Variation of predicted Elastic Coulomb friction damping with normal contact stiffness

This shows that the damping is slightly increased with reduced normal stiffness. This is caused by a more uniform distribution of normal pressure over the contact surfaces due to the higher contact flexibility. The increased pressure acting on the lightly loaded nodes brings more nodes into slip by reducing the elastic limits.

The dependence on friction coefficient is shown in Table 8.4, where the calculation is repeated using a value of $\mu = 0.2$. The increase in μ allows a higher tangential force to be sustained elastically, causing the elastic limit to be increased above the displacements of all nodes. The elimination of all nodes in slip results in zero damping.

The graph in Figure 8.11 shows the variation in damping ratio with modal amplitude for Mode 8 as the response amplitude is increased from zero to an order of magnitude above the forced response amplitude. Marked on the graph are a series of vertical lines, which represent the transition point when an individual contact node changes from stick to slip. These slip transition markers can be compared with the normalised node displacements shown in Figure 8.10. At the forced response am-

Mode No.	Expected ζ_{mech}	Predicted ζ_{mech}	
		$\mu = 0.122$	$\mu = 0.2$
8	0.24%	0.0027%	0%
9	0.03%	0%	0%
10	0%	0.0001%	0%

Table 8.4: Variation of predicted Elastic Coulomb friction damping with friction coefficient

plitude, denoted by the dashed vertical line, it can be seen that the only two nodes are in slip. An increase in displacement of around 20% brings a third node into slip, whilst a small cluster of nodes start to slip when the amplitude is doubled. It is also apparent that approximately only 10% of the nodes reach slip when the displacements are magnified by a factor of 10, with the result that the damping values are still very low. The sensitivity study of the elastic Coulomb model therefore shows that the model will significantly under-predict friction damping for a wide range of input parameters and vibration amplitudes.

Discussion

The Rigid and Elastic Coulomb calculations in the above case provide little assistance in the prediction of friction damping – either quantitatively or qualitatively due to the limitations of the Coulomb model for dealing with small-scale displacements. The Rigid Coulomb model vastly over-predicts the friction damping, whilst the Elastic Coulomb model greatly under-predicts damping. The case does, however, demonstrate the need to investigate the microslip behaviour for the majority of nodes that remain within the elastic limit.

An investigation into the influence of contact stiffness, friction damping ratio and modal amplitude on the predicted damping ratio has shown that the under-prediction by the Elastic Coulomb model is not caused by the choice of input parameters. The limitation of the Elastic Coulomb method is due to the large proportion of contact nodes remaining in stick and the inability of the approach to include the effects of such non-sliding nodes.

Mode	Modal Amplitude	Expected ζ_{fric}	Microslip ($\mu = 0.122$) ζ_{fric}	Microslip ($\mu = 0.2$) ζ_{fric}
8	5.519×10^{-7}	0.24%	0.11%	0.066%
9	5.70×10^{-7}	0.03%	0%	0%
10	1.713×10^{-7}	0%	0.01%	0.007%

Table 8.5: Rigid and Elastic Coulomb friction damping predictions

8.4.3 Microslip friction analysis

Results

The microslip model is verified by reproducing the force-displacement curve given in Figure 9 of Olofsson [130], using the microslip parameters outlined above. Figure 8.12 shows a superposition of the original graph of Olofsson with the solution reproduced using a spreadsheet. The excellent agreement between the analytical solution of the microslip model with the original verifies that the calculation is done correctly.

The resulting microslip damping predictions for the three modes using the datum values outlined above in Section 8.3.2 are given in Table 8.5. It can be seen that the microslip calculation agrees fairly well with the expected friction damping, where only Mode 8 provides a significant amount of damping. Whilst the Mode 8 damping ratio is under-predicted by 50%, this result captures the dependance of friction on modeshape very well.

Sensitivity to input parameters

Included in Table 8.5 is the predicted damping ratios calculated using a different friction coefficient of $\mu = 0.2$. Here, it can be seen that an increase in friction coefficient reduces the damping ratio, whilst the trend of mode shape dependence is maintained. Equation 3.35 states that the slip limit is proportional to friction coefficient, giving an increased slip limit with an increase in friction coefficient. For a given displacement, the contact motion will be reduced in relation to the microslip curve, giving less damping. Conversely, the increased slip limit gives a

reduced effective tangential contact stiffness, resulting in an increased amount of contact motion in the modes. The overall effect is highly non-linear, as shown by the damping ratio-displacement curve in Figure 3.15. The result in this case is reduced damping with increased friction coefficient.

A major simplification in the microslip approach is the assumption that the effective tangential stiffness does not vary with the tangential displacement. The approximation of the tangential stiffness of each node in the above calculations is done using the microslip friction force at half the slip displacement. The sensitivity of damping predictions to the choice of position along the microslip curve is assessed by repeating the Mode 8 calculation using a range of positions. The resulting damping ratios plotted in Figure 8.13 shows a reasonable variation in damping due to the change in effective tangential stiffness. Calculating the tangential stiffness at very small displacements gives the highest stiffness and lowest damping ratios, whereas calculating the stiffness at the slip limit results in lower stiffness and higher damping.

The variation of predicted microslip damping with blade vibration levels is assessed by repeating the Mode 8 calculation at a range of modal amplitudes above and below the forced response solution. Figure 8.14 shows an almost linear increase of damping ratio with an increase in response, where all nodes contribute to damping before they reach gross slip, preventing the sudden changes seen in the Elastic Coulomb results presented earlier. The damping behaviour of this multi-DoF problem can be compared to the graph of the single-DoF system provided in Figure 3.15. Both microslip systems are seen to provide an almost linear increase of damping ratio with response amplitude for the very low contact displacements seen at the blade root.

Discussion

The microslip damping predictions agree very well with the expected values for all three modes. The dependence on mode shape is well-captured, with Mode 8 providing a significant amount of damping and Modes 9 and 10 providing almost no damping. The Mode 8 damping was predicted within around 50% of the expected value using published input parameters that have been verified for the same materials

under similar contact conditions.

The friction behaviour does not show a high sensitivity to the input parameters, displaying a smooth variation in damping as the parameters are varied. Similarly, the method of calculating the effective tangential stiffness does not cause a large variation in results.

The microslip calculation predicts an almost linear increase of damping ratio with modal amplitude around the range of the forced response solution. This is due to the fact that the large majority of nodes in compressive contact are subject to very small tangential displacements that are much lower than the elastic limits. The near-linear behaviour for small displacements is also seen in the solution of a simple single-DoF microslip system, shown in Figure 3.15. However, experimental measurements of mechanical damping of fixed root blades can often suggest that damping remains fairly constant over typical ranges of blade vibration. Whereas the predicted blade microslip damping shows a similar linear characteristic to a simple 1-D brick-type object undergoing pure microslip, the comparison with experimental behaviour suggests that either a) more complex physical mechanisms are present; or b) the linearisation process is not capturing some important non-linear effects.

8.5 Conclusions

A new Adaptive Constraint Method for modelling blade root friction has been developed and successfully implemented for an industrial compressor blade. Based on an advanced microslip model, the friction predictions agree with the damping values derived from test data.

The new method meets many of the requirements for use in industry. The frequency-domain solution allows the modal friction damping ratios to be calculated based on a single FE analysis with high computing efficiency. User interaction is very low, with a high level of automation provided by a series of ANSYS macros to modify the existing FE model and perform the analysis. The only area of significant user effort is in the identification of nodes on the root surface, resulting in an overall effort that is much less demanding than a standard time-accurate ANSYS contact

analysis.

It has been demonstrated that the Rigid and Elastic Coulomb friction models are not suitable for the prediction of friction damping at the blade root due to their inability to deal with the very low displacements. The Elastic Coulomb analysis of Mode 8, shows that only 2 nodes out of the 204 nodes in contact actually reach slip, with the result that the damping contributions of the remaining 99% of the contact nodes are neglected and the friction damping is vastly under-predicted. Conversely, the Rigid model greatly over-predicts damping by assuming that the entire friction surface achieves gross sliding.

Whilst the friction behaviour predicted by the Coulomb approaches has been shown to be sensitive to the model parameters, the microslip model is much more robust and does not show any sudden changes with contact parameters or response amplitude. An additional observation is the linear increase of damping ratio with response amplitude predicted by the microslip model. An area of question is the method of calculating the effective tangential stiffness using the microslip model, where stiffness is calculated using a fixed point on the microslip curve. A variation in the assumed displacement produces a change in damping, hence an area for improvement could be to calculate the effective tangential stiffness as a function of actual displacement.

8.6 Figures

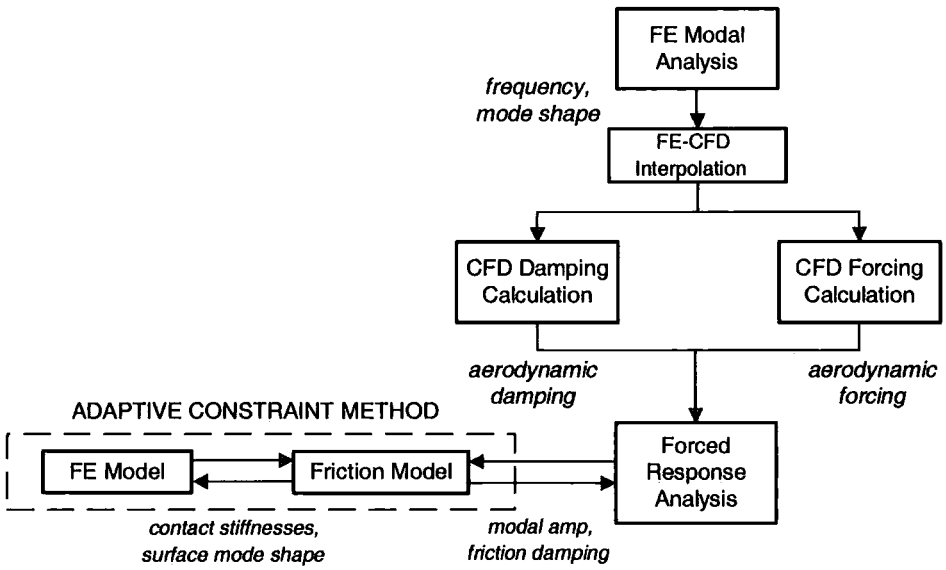

Figure 8.1: Application of friction calculation into decoupled forced response system

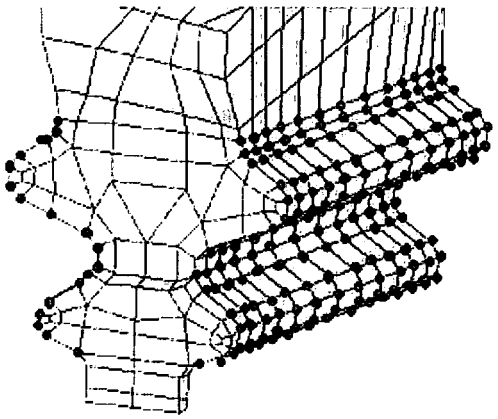

Figure 8.2: Friction contact nodes on surfaces of root flanks

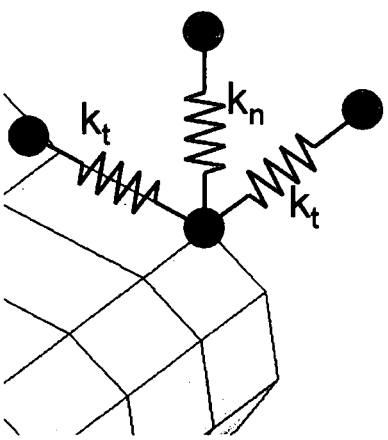

Figure 8.3: Spring representation of 3-D contact stiffness at each contact node

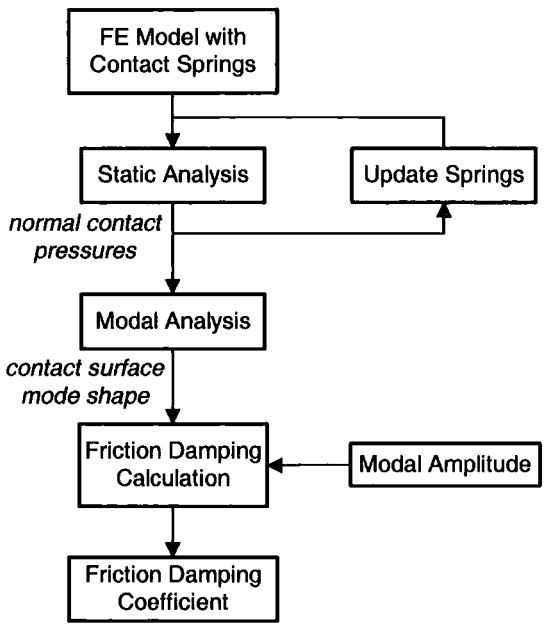

Figure 8.4: Adaptive Constraint Method of FE friction modelling

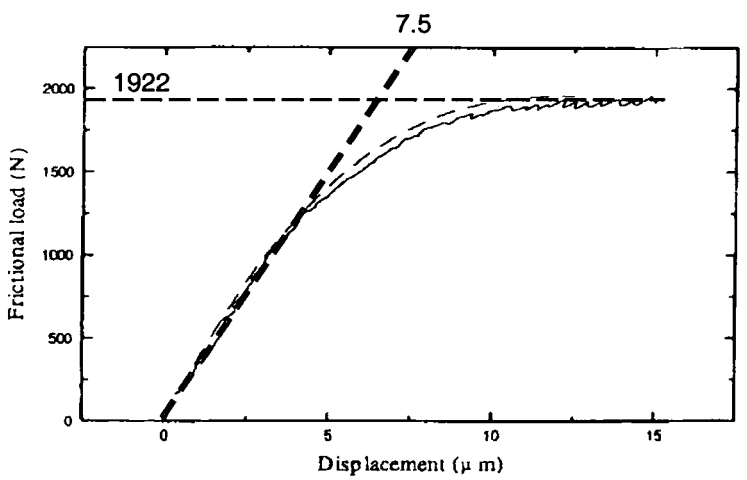

Figure 8.5: Derivation of tangential stiffness from microslip curve

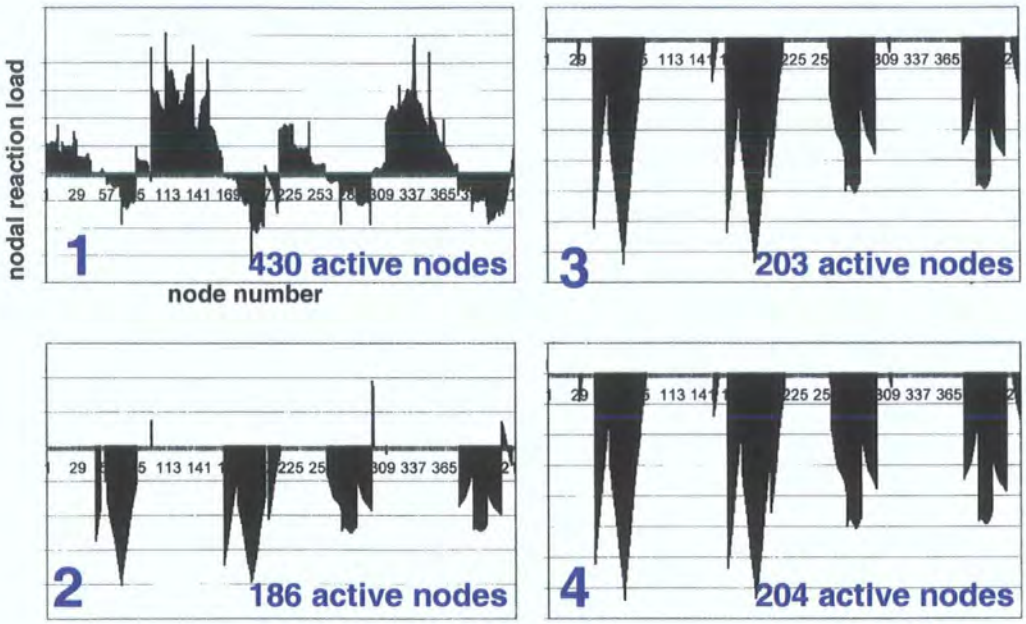

Figure 8.6: Nodal pressures after each static solution, showing convergence of static contact analysis

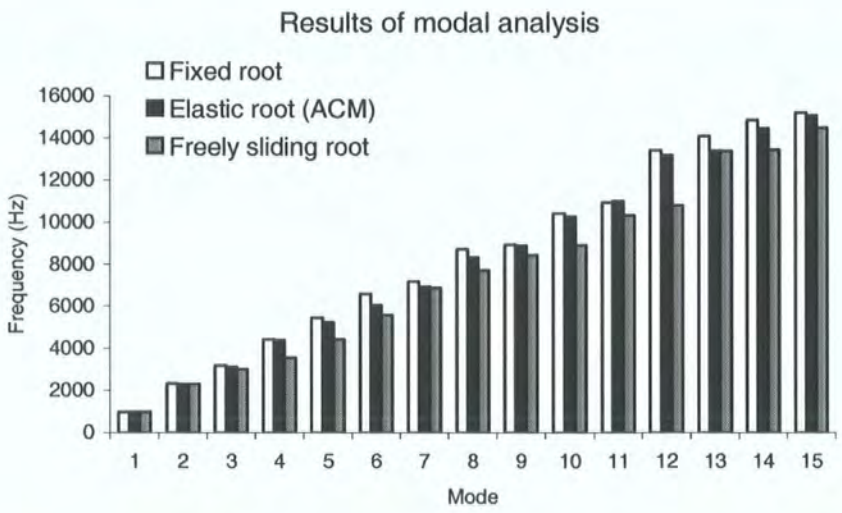

Figure 8.7: Blade modal frequencies using Coulomb approach

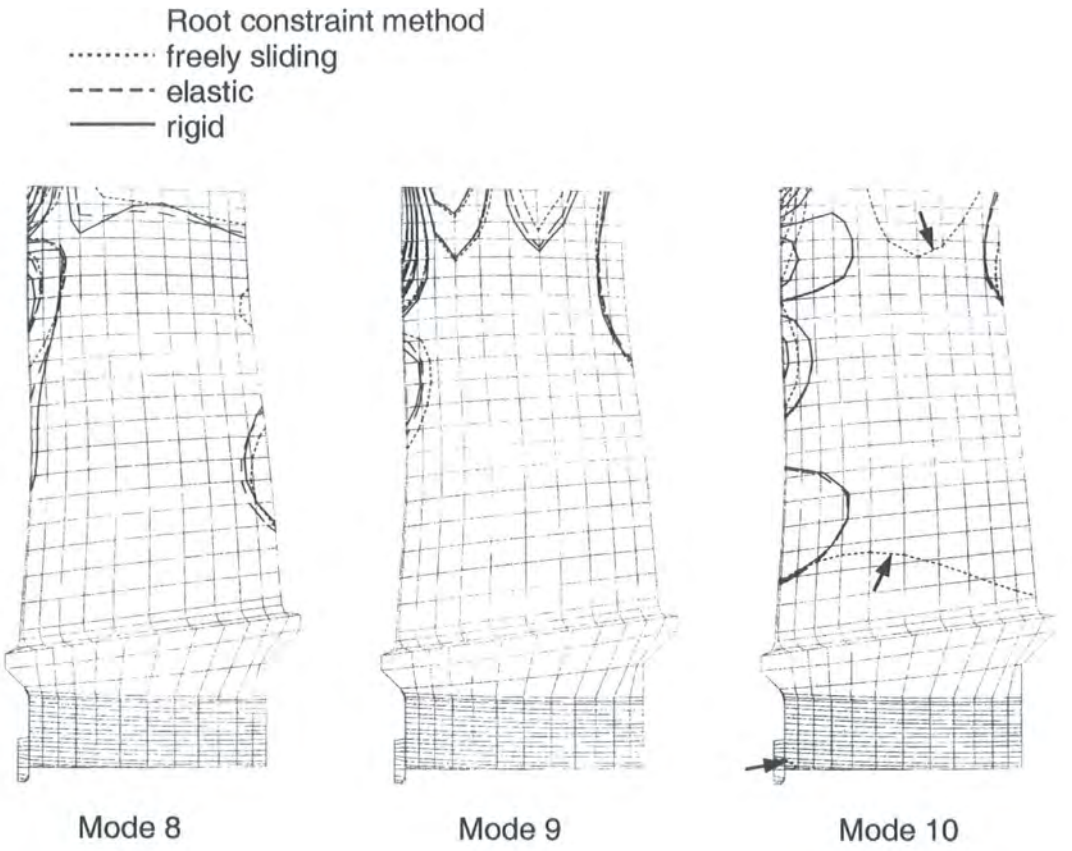

Figure 8.8: Comparison of mode shapes for various methods of root constraint

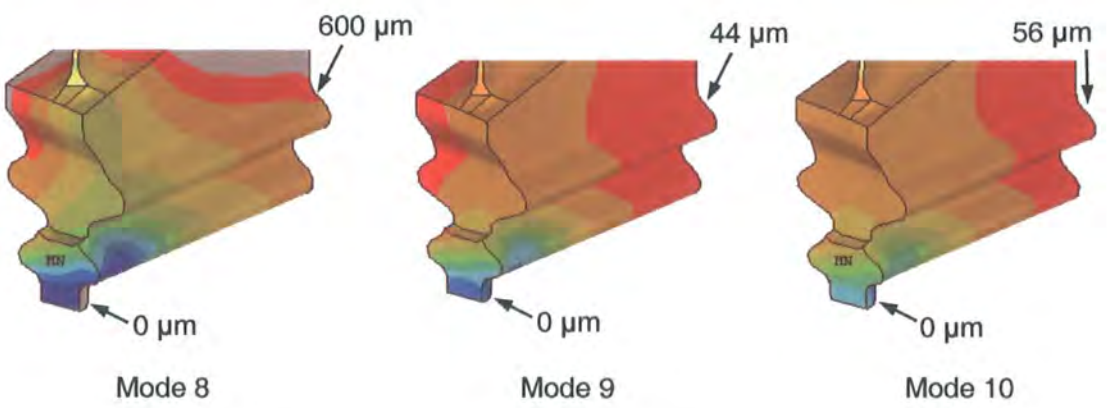

Figure 8.9: Tangential contact displacements at modal forced response solutions

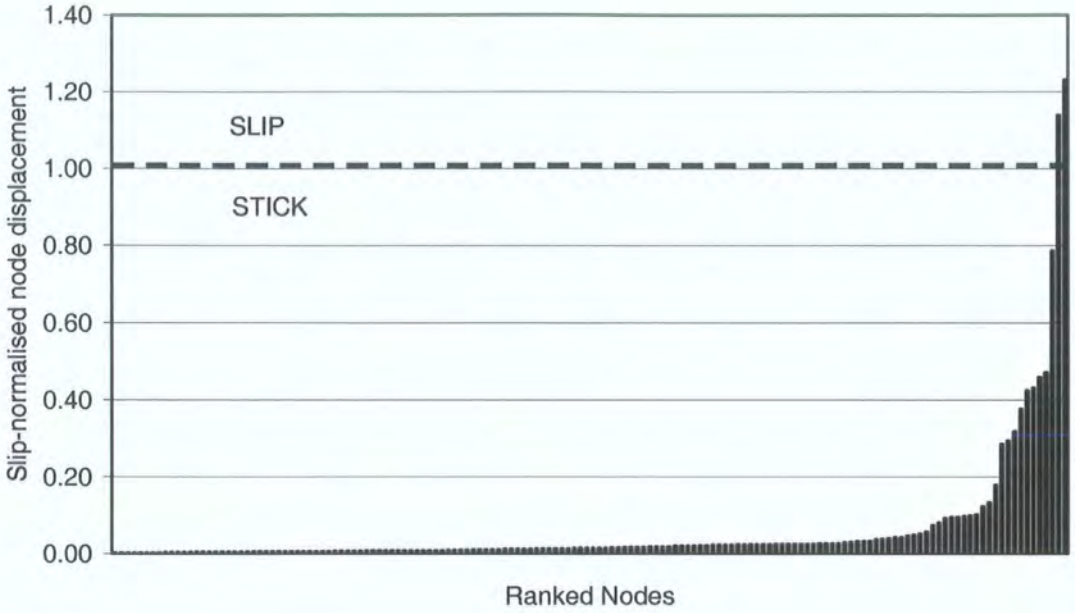

Figure 8.10: Mode 8 tangential contact displacements normalised to elastic limit

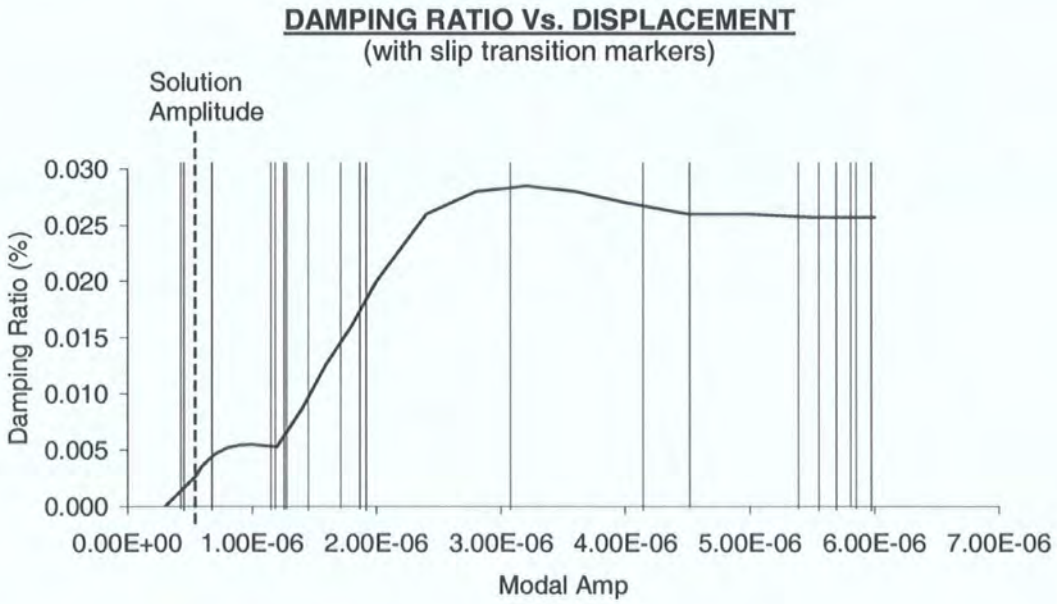

Figure 8.11: Variation of damping ratio with response amplitude for mode 8, showing individual node stick-slip transition points

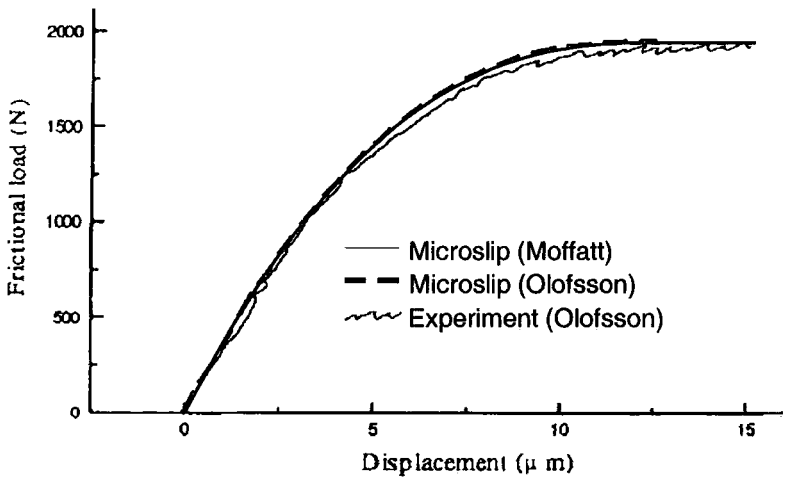

Figure 8.12: Comparison of microslip calculation with original calculation of Olofsson, 1995

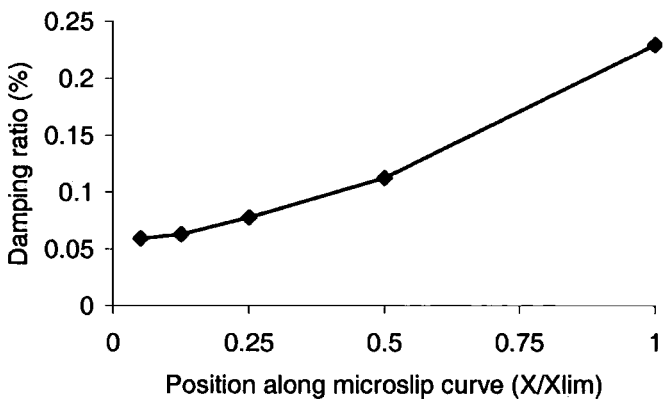

Figure 8.13: Variation of predicted microslip friction damping with position of effective stiffness calculation for Mode 8

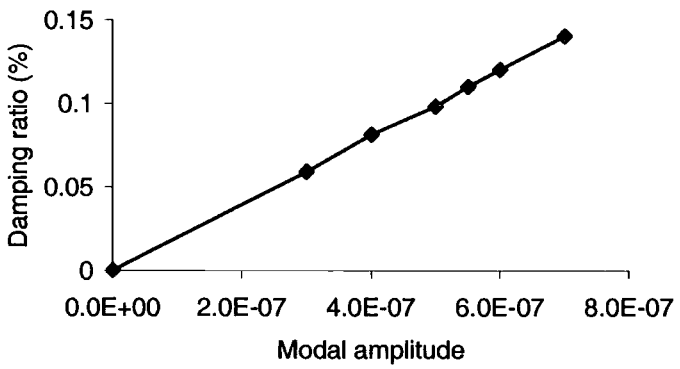

Figure 8.14: Variation of predicted damping with response amplitude for Mode 8

Chapter 9

Conclusions and Recommendations

9.1 Conclusions

The objective of this project was to develop an efficient and accurate aeromechanical analysis tool capable of providing reliable resonant forced response predictions for turbomachinery blade designers under the commercial restraints of solution times and computing resources. Both decoupled and fully-coupled approaches for the modelling of flow-structure interaction have been developed and the capabilities of such methods to capture important coupling effects have been evaluated. In addition, a method of predicting the friction damping of fir-tree type blade root attachments has been developed, leading to an evaluation of the mode shape dependence and the importance of microslip behaviour.

9.1.1 Decoupled forced response system

The decoupled method represents an open loop system, requiring only a single execution of the flow and structural equations. Blade mode shapes and natural frequencies are assumed to remain unchanged by aerodynamic loads due to the high relative density and stiffness of turbomachinery blades. The FE modal analysis is evaluated independently to the fluid calculations, where blade mode shapes are accurately

translated onto the CFD mesh to enable a forced response solution in modal space based on the CFD mesh.

A method for interpolating the modeshapes from the FE to CFD mesh has been produced, based on 2D linear interpolation over the blade surface. The capabilities of the method are demonstrated with an industrial case, where difficulties of mesh alignment, non-coincident mesh surfaces, low mesh resolution and high mode shape gradients are overcome and excellent accuracy of mode shape interpolation is seen.

Flow is modelled by the nonlinear harmonic method, solving the unsteady Navier-Stokes equations in the frequency-domain using a single-passage approach, whilst maintaining the ability to include important non-linear effects. With single degree-of-freedom structural modelling based on modal reduction, the system can predict resonant vibration levels 30-100 times faster than direct time-domain schemes.

Fluid-structure interaction is modelled on a linear basis, assuming that aerodynamic damping loads increase linearly with vibration amplitude. This allows the calculation of aerodynamic forcing and damping to be done separately from one-another, and independently to the forced response solution.

The decoupled forced response solution is calculated using conventional modal reduction theory, reducing the structural FE model to a single degree-of-freedom modal equation. In addition, a new energy method provides an alternative to the solution of the modal equation, which solves the response directly on the CFD mesh without the knowledge of original modeshape scaling. Both methods are shown to give identical results.

9.1.2 Verification Cases

A detailed demonstration of the forced response system and an initial verification of the individual system components has been done using a case study of the NASA Rotor 67 transonic aero engine fan. The resonant excitation of three low order modes and one high order mode is given by hypothetical inlet distortions, to provide a realistic test case that is typical of inlet distortion and bladerow interaction problems.

Validation of the forced response system has been done against the Siemens 3-

stage transonic industrial compressor, where predicted resonant strains and damping levels are compared with measured strain gauge data from a full-scale rotating test. The vibration of three high-order modes of the last rotor stage is predicted, with excitation caused by interference from the upstream stator wakes. The damping calculations have shown that aerodynamic damping is strongly influenced by modeshape and a comparison with strain gauge data also indicates a strong correlation between mechanical damping and modeshape. Predicted resonant strains for the three crossing points compare reasonably well with strain gauge measurements, demonstrating the ability of the method to predict resonant vibration levels. The high efficiency of the unsteady multi-stage calculation also demonstrates the system can be used routinely in the blade design process to tackle aeromechanical issues, where the 3D unsteady viscous CFD analysis of the 3-stage compressor was achieved in under a week on a single CPU.

9.1.3 Fully-coupled forced response systems

Two fluid-structure fully-coupled forced response methods have been developed with the intention of increasing computational efficiency over the decoupled method by combining the calculation of aerodynamic excitation and damping forces into a single calculation. The modal equation is fully integrated into the flow solver and solved either directly in the frequency domain or by time-marching using a hybrid approach.

The frequency-domain method simultaneously solves the fluid and modal equations by pseudo-time integration using the 4-stage Runge-Kutta scheme, where aerodynamic forcing and blade displacement amplitudes are exchanged at each step.

The hybrid approach solves the fluid equations in the frequency domain, but marches the modal equation in time with periodic updating of the reconstructed aerodynamic modal force. A Fourier transform of the continuous time trace of the modal displacement is taken after each forcing period to give the response modal amplitude. The resulting blade displacement amplitudes are then fed back into the fluid equations to close the feedback loop. Both fully-coupled systems are shown produce identical results, serving a cross-checking purpose.

9.1.4 Fluid-structure coupling effects

An investigation into the characteristics of decoupled and fully-coupled methods was undertaken using the four modes of the NASA Rotor 67 transonic fan case. It was shown that decoupled systems can accurately predict resonant vibration amplitudes from a single calculation at the blade natural frequency, whilst fully-coupled forced response solutions are subject to a shift in resonant frequency, thus requiring multiple solutions. A novel closed-loop resonance tracking algorithm was incorporated into the coupled solution to adjust the solution frequency and obtain the peak vibration amplitude at the new resonant condition. Due to the need for multiple solutions, the computational efficiency of the coupled solution showed no gain over the decoupled method. In contrast, the decoupled method is shown to be insensitive to frequency shift, maintaining resonance at the blade natural frequency and capturing the resonant peak with one solution.

A study into the fluid-structural coupling effect identified the source of the frequency shift in the coupled solution to be due to the added mass effect of the vibration-induced aerodynamic damping forces. A single coupled solution at any frequency can not be used to predict resonance; hence coupled methods must rely on multiple solutions to find the resonant peak. The need for resonance tracking with coupled methods is especially important for high-order modes, which are often associated with low mechanical damping and strong fluid-structure coupling effects.

The decoupled method is identified as the preferred approach to bladerow interaction problems due to the ability to accurately predict the resonant peak with high efficiency from a single solution.

9.1.5 Friction Modelling

A new Adaptive Constraint Method for predicting blade root friction has been developed and implemented for the Siemens industrial compressor blade. The model is based entirely in the frequency domain using a FE modal approach to maximise computing efficiency and maintain high compatibility with the existing forced response system.

Contact mechanics are represented using traditional Coulomb friction models and an advanced semi-analytical microslip model. Normal and tangential contact loads are linearised on an FE blade model by a series of spring elements. Non-linearity in the contact mechanics is incorporated by performing the FE static analysis in an iterative manner, where the stiffness values are updated at each step. A modal analysis is performed to provide the mode shape over the contact surfaces, allowing the friction damping calculation to be done separately.

The Coulomb and microslip contact behaviour is derived from a published microslip model, where input parameters were fitted to test data for similar contact conditions. The predicted damping ratios are compared with the mechanical damping values derived from test data.

It was found that the damping predictions of the Rigid and Elastic Coulomb friction models were very inaccurate due to their inability to deal with the very low displacements involved. Neither Coulomb approach predicted the trend with mode shape, with the Rigid model vastly over-predicting damping and the Elastic model predicting almost no damping. The under-prediction of the Elastic approach is due to the very small proportion of contact nodes reaching slip, where the contributions from 99% of all contact nodes are neglected. The very high prediction by the Rigid model is due to the assumption that the entire contact surface achieves gross slip. The Coulomb predictions are very sensitive to variations in contact parameters due to the small proportion of nodes reaching slip, where the contribution from a single node reaching slip causes a sudden change in the overall behaviour.

The microslip damping predictions showed good agreement with the expected behaviour, where the dependence on mode shape was captured well and the damping levels were predicted within 50%. The microslip model is well suited to small displacement applications where very little gross slip is achieved. The method includes the contribution of each individual contact node, based on the knowledge that a degree of damping is always encountered before gross slip takes place. The microslip model is much more robust than the Coulomb models and does not produce sudden changes in damping with variations in contact parameters or vibration amplitude.

The Adaptive Constraint Method has achieved the original objective of providing

a qualitative prediction of friction damping for the three modes of the Siemens compressor case, together with a quantitative indication of the damping levels. The scheme meets many of the requirements for routine use in an industrial environment, allowing the efficient prediction of all modes with a single analysis. User interaction is low due to the high level of automation using ANSYS macros, greatly reducing the manual processing time needed for conventional time-domain solutions.

9.2 Recommendations for Future Research

9.2.1 Forced response system

Further Evaluation

It is recognised that further evaluation of the forced response system using realistic test cases is necessary for full validation of the methodology. Whilst the aerodynamic solver has been validated for a number of academic and industrial cases, further assessment of the complete forced response system against detailed strain gauge measurements in full-scale rotating engine tests would be beneficial.

Modal Interaction

Further research could look at the effects of increasing the number modes used in the forced vibration analysis. The current system uses only a single flow harmonic applied to a single mode for the crossing point in question, based on the assumption that all frequencies outside resonance have a negligible effect on vibration amplitudes. This assumption is generally adequate for cases where the modal frequencies are placed sufficiently far from one another, such that the effects of modal coupling can be ignored. It is possible that a forced response approach that accounts for modal coupling could provide greater accuracy in predictions for modes 8 and 9 of the Siemens compressor case study given in Section 5.3.

For cases where two modes are placed close to a resonant frequency, modal coupling may have a significant effect on both the dynamics and forced response of the system. The close proximity of two modes introduces a coupling effect, where

the modal properties of the two individual modes begin to share characteristics as they come closer in frequency. Consider a blade where the 2^{nd} flap mode (F_2) lies close to the 1^{st} torsion mode (T_1). The flap mode will display a degree of twist in the tip and the torsion mode will contain an amount of F_2 mode shape. A result of this modal coupling is that the presence of the T_1 mode shape in the F_2 mode causes the F_2 mode to be influenced by any forcing distribution similar to the T_1 modal force. Similarly, the T_1 mode will be influenced by the F_2 forcing. Therefore, any blade motion caused by the the forced response in one mode will contribute to the motion from the other mode, with the subsequent increase in modal strains.

It may be possible to provide a simple two-mode evaluation using the decoupled method with a frequency sweep. For each of the two modes, the decoupled responses are calculated individually at a single frequency, with a linear superposition of the resulting modal displacements and strains. The process is repeated around the two natural frequencies to find the peak responses. Using the coupled approach, the two modal equations are solved simultaneously by the frequency-domain CFD solver, subject to unsteady pressures calculated at the solution frequency.

9.2.2 Root Friction Modelling

Whilst the friction prediction method shows very promising results, the development of the Adaptive Constraint Method is relatively immature and further work is required to improve the methodology and provide further validation.

Full FE transient analysis

At this stage, it is important to have a benchmark friction prediction method capable of producing reliable results, thus providing a comparison for the results of new methodologies. A suggestion for the benchmark method would be an ANSYS transient analysis, where the friction forces are resolved in the time-domain and the linearisation of contact loads is avoided. Such an approach would be useful for evaluating the general behaviour of the Adaptive Constraint Method in both Coulomb and microslip applications for varying levels of displacement amplitudes. The procedure for Coulomb friction calculations is standardised and is well documented.

The microslip model given by Olofsson [130] implemented in this work has previously been incorporated into ANSYS by the developers of the model, as discussed by Sellgren and Olofsson [150]. This time-accurate microslip model integrated into the FE solver would provide a good ground for further evaluation of the Adaptive Constraint Method.

Simple test case

Preliminary test cases do not need to include the complexities of a blade fir-tree root and simplified models may provide a useful insight into the underlying characteristics of the methods. A good starting point may be the analysis of a flexible brick-type structure of low mesh density on a rigid, flat friction surface. Subject to a simple static loading condition, the friction damping can be calculated for a range of conditions to isolate individual characteristics of the solution methods. For example a variation in the tangential displacement amplitude or normal pressure distribution will provide an evaluation of the limiting boundaries of the Coulomb and microslip models. A simplified model will also allow the assessment of input parameters against any published test data.

Linearisation of tangential stiffness

A possible area for future investigation is in the calculation of effective tangential stiffness in the microslip analysis. The tangential stiffness remains fairly constant from zero to around 50% of the gross slip limit. After this, the effective stiffness is reduced as the surface starts to slip. In order to model the tangential stiffness with the greatest possible fidelity within the linear framework could be to incorporate an iterative modal analysis, to linearise the effective stiffness for a given modal amplitude. The inclusion of the response modal amplitude in modal analysis would therefore allow each tangential stiffness to be calculated as a function of absolute displacement. The modification of the tangential stiffness will be incorporated in the analysis by performing the modal analysis in an iterative manner in a similar way to the static analysis. An area of concern with this method is the convergence stability of the modal analysis due to the updating of the effective tangential stiffness. Whilst

the normal stiffness is increased with increasing pressure (and normal deflection), the effective tangential stiffness is reduced with displacement, as the force curve levels off. The implications of this softening effect are currently unknown.

Bibliography

[1] Kielb, R.E. (1999), *Forced Response Analysis - 1*, Aeroelasticity in Axial Flow Turbomachines, Lecture Series 1999-05, von Karmen Institute for Fluid Dynamics, May 3-7, 1999.

[2] Fransson, T. (1999), *Basic Introduction to Aeroelasticity*, Aeroelasticity in Axial Flow Turbomachines, Lecture Series 1999-05, von Karmen Institute for Fluid Dynamics, May 3-7, 1999.

[3] Wisler, D. C. (2003), *Engineering What You Dont Necessarily Learn in School*, ASME paper GT2003-38761.

[4] Kielb, R.E. (1999), *Aeroelastic Models*, Aeroelasticity in Axial Flow Turbomachines, Lecture Series 1999-05, von Karmen Institute for Fluid Dynamics, May 3-7, 1999.

[5] Marshall, J.G. (1996), *Prediction of Turbomachinery Aeroelasticity Effects Using A 3D Non-Linear Integrated Method*, PhD Thesis, Imperial College of Science Technology and Medicine, University of London, 1996.

[6] Fransson, T. (1999), *Important Parameters*, Aeroelasticity in Axial Flow Turbomachines, Lecture Series 1999-05, von Karmen Institute for Fluid Dynamics, May 3-7, 1999.

[7] Ewins, D.J. (1991), *The Effect of Blade Mistuning on Vibration Response - A Survey*, IFToMM 4th International Conference on Rotordynamics, Prague, Czechoslovakia, 1999.

[8] Bowden, F.P. and Tabor, D., 1974, *An Introduction to Tribology*, Heinemann Educational.

[9] Kielb, R.E. and Imregun, M., (1999), *Damping Characteristics*, Aeroelasticity in Axial Flow Turbomachines, Lecture Series 1999-05, von Karmen Institute for Fluid Dynamics, May 3-7, 1999.

[10] MacCormack, R. W. (1969), *The Effect Of Viscosity In Hypervelocity Impact Cratering*, AIAA Paper No. 69-0354, 1969.

[11] Jameson, A Et Al (1983), *Numerical Solutions Of The Euler Equation By Finite Volume Method Using Runge-Kutta Time-Stepping Scheme*, AIAA Journal, Vol 32, No. 1, pp46-53, 1983.

[12] Fransson, T. and Pandolfi, M. (1986), *Numerical Investigation of Unsteady Subsonic Compressible Flows Through an Oscillating Cascade*, ASME Paper 86-GT-304, 1986.

[13] Gerolymos, G. A. (1988), *Numerical Integration of the Blade-Blade Surface Euler Equations in Vibrating Cascades* AIAA Journal, Vol. 26, No.12, pp1483, 1988.

[14] He, L. (1990), *An Euler Solution fo Unsteady Flows Around Oscillating Blades*, Journal of Turbomachinery, Vol. 112, pp. 714, 1990.

[15] Giles, M.B. (1988), *Calculation of Unsteady Wake/Rotor Interaction*, AIAA Journal of Propulsion, Vol. 4, No.4, pp.356, 1988.

[16] Namba, M. (1977), *Three-Dimensional Analysis of Blade Force and Sound Generation for an Annular Cascade in Distorted Flows*, Journal of sound and Vibration, Vol. 50, pp. 479-508, 1977.

[17] Chi, R.M. (1991), *An Unsteady Lifting Surface Theory for Ducted Fan Blades*, ASME Paper 91-GT-131, 1991.

[18] Hall, K.C. and Lorence, C.B. (1992), *Calculation of Three-Dimensional Unsteady Flows in Turbomachinery Using the Lineazed Harmonic Euler Equations*, ASME Paper, 92-GT-136, 1992.

[19] Gerolymos, G.A. (1992), *Advances in the Numerical Integration of of the 3-D Euler Equations in Vibrating Cascades*, ASME Paper 92-GT-170, 1992.

[20] Marshall, J.G and Giles, M.B. (1997), *Some Applications of a Time-Linearised Euler Method to Flutter and Forced Response in Turbomachinery*, Proceedings of the 8th International Symposium on Unsteady Aerodynamics and Aeroelasticity of Turbomachines, Stockholm, Sweden, 1997.

[21] He, L., Denton, J.D. (1994), *Three-Dimensional Time-Marching Inviscid And Viscous Solutions For Unsteady Flows Around Vibrating Blades*, ASME Journal Of Turbomachinery, July 1994, Vol 116, pp469-475, 1994.

[22] Rai, M.M. (1987), *Unsteady Three-Dimensional Navier-Stokes Simulations of Turbine Rotor-Stator Interaction*, AIAA-87-2058, 1987.

[23] Chen, J.P., Celestina, M.L. and Adamczyk, J.J. (1994), *A New Procedure for Simulating Unsteady Flows Through Turbomachinery Blade Pasasges*, ASME Paper 94-GT-151, 1994.

[24] Erdos, J. I. And Alzner, E. (1978), *Computation Of Unsteady Transonic Flows Through Rotating And Stationary Cascade*, NASA Cr-2900, 1978.

[25] Rai, M.M. (1985, *Navier-Stokes Simulations of Rotor-Stator Interaction Using Patched and Overlaid Grids*, AIAA Paper 85-1519, 1985.

[26] He, L. (1989), *An Euler Solution For Unsteady Flows Around Oscillating Blades*, ASME Journal, Vol. 112, 1989.

[27] He, L. (1992), *A Method of Simulating Unsteady Turbomachinery Flows with Multiple Perturbations*, AIAA Journal, Vol. 30, No. 12, 1992.

[28] Whitehead, D.S. (1960), *Force and Moment Coefficients for Vibrating Aerofoils in Cascades*, Reports and Memoranda No. 3254, Aeronautical Research Council, London, 1960.

[29] Whitehead, D.S. (1970), *Vibration and Sound Generation in a Cascade of Flat Plates in Subsonic Flow*, A.R.C. R&M, No. 3876, 1970

[30] Namba, M. (1972), *Lifting Surface Theory for a Rotating Subsonic or Transonic Bladerow*, A.R.C. R&M, No. 3740, 1972.

[31] Verdon, J.M. and McCune, J.E. (1975), *Unsteady Supersonic Cascade in Subsonic Axial Flow*, AIAA Journal, Vol. 13, No. 2, pp. 193-201, 1975.

[32] Whitehead, D.S. (1987), *Classical Two-Dimensional Methods*, AGARD Manual on Aeroelasticity in Axial-Flow Turbomachines, Unsteady Turbomachinery Aerodynamics, Vol. 1, AGARD-AG-298, 1987.

[33] Whitehead, D.S. (1982), *The Calculation of Steady and Unsteady Transonic Flow in Cascades*, University of Cambridge, Department of Engineering Report CUED/A-Turbo/TR118, 1982.

[34] Verdon, J.M. and Caspar, J.R. (1984), *A Linearised Unsteady Aerodynamic Analysis For Transonic Cascades*, J. Fluid Mechanics, 149 pp 403-429, 1984.

[35] Hall, K.C. and Verdon, J.M. (1991), *Gust Response Analysis for Cascades in Non-Uniform Mean Flow*, AIAA Journal, Vol. 29, No. 9, pp. 1463-1471, 1991.

[36] Ni, R.H. (1974), *Nonstationary Aerodynamics of Arbitrary Cascades in Compressible Flow*, PhD Thesis, Stevens Institute of Technology, June, 1974.

[37] Hall, K.C. and Crawley, E.F. (1989), *Calculation of Unsteady flows in Turbomachinery Using the Linearised Euler Equations*, AIAA Journal, Vol. 27, pp. 777-787, 1989.

[38] Lindquist, D.R. and Giles, M.B. (1991), *On the Validity of Linearised Euler Equations With Shock Capturing*, AIAA 91-1598-CP, 1991.

[39] Hall, K.C., Clark, W.S. and Lorence, C.B. (1994), *A Linearised Euler Analysis of Unsteady Transonic Flows in Turbomachinery*, Journal of Turbomachinery, Vol. 116, No. 3, July, pp477-488, 1994.

[40] Cizmas, P.G.A. and Hall, K.C. (1995), *A Viscous-Inviscid Model of Unsteady Small-Disturbance Flows in Cascades*, AIAA Paper No. 95, pp. 2655, 1995.

[41] Holmes, D.G. Mitchell, B.E. and Lorence, C.B. (1997), *Three-Dimensional Linearised Navier-Stokes Equations for Flutter and Forced Response*, Proceedings of the 8th International Symposium on Unsteady Aerodynamics and Aeroelasticity of Turbomachines, Stockholm, Sweden, 1997.

[42] Clark, W.S. and Hall, K.C. 2000, *A Time-Linearized Navier-Stokes Analysis of Stall Flutter*, ASME Journal of Turbomachinery, Vol. 122, pp. 467-476, 2000.

[43] Sbardella, L. and Imregun, M. (2001), *Linearised Unsteady Viscous Turbomachinery Flows Using Hybrid Grids*, ASME Journal of Turbomachinery, Vol. 123, July, pp. 568-582, 2001.

[44] Giles, M.B. (1992), *An Approach for Multi-stage Calculations Incorporating Unsteadiness*, ASME 92-GT-282, 1992.

[45] He, L. (1996), *Modelling Issues for Computation of Unsteady Turbomachinery Flows*, Unsteady Flows in Turbomachines VKI Lecture Series, March 1996.

[46] Hall, K.C., Thomas, J.P. and Clark, W.S. (2002), *Computation of Unsteady Nonlinear Flows in Cascades using a Harmonic Balance Technique*, AIAA Journal, Vol. 40, No, 5, pp. 477-886, 2002.

[47] Vasanthakumar, P. (2003), *Three dimensional Frequency-domain Solution Method for Unsteady Turbomachinery Flows*, PhD Thesis, University of Durham, 2003.

[48] Vasanthakumar, P., Chen, T. and He, L. (2000), *Three-Dimensional Viscous Computation of Blade Flutter and Forced Response using Nonlinear Harmonic*

Approach, The 9th International Symposium on Unsteady Aerodynamics and Aeroelasticity of Turbomachines, September 4-8 2000, Editors Ferrand, P. and Aubert, S., Published by Presses Universitaires de Grenoble, 2000.

[49] Chen, T., Vasanthakumar, P. and He, L. (2001), *Analysis of Unsteady Bladerow Interaction Using Non-Linear Harmonic Approach*, AIAA Journal of Power and Propulsion, Vol. 17, No. 3, May 2001; also ASME Paper 2000-GT-431, 2000.

[50] Ning, W., Li, Y.S. and Wells, R.G. (2003), *Predicting Bladerow Interactions Using a Multistage Time-Linearised Navier-Stokes Solver*, Journal of Turbomachinery, Jan 2003, Vol. 125, Issue 1, pp. 25-32, 2003; ASME Paper 2002-GT-30309, 2002.

[51] Ning, W., Moffatt, S., Li, Y., Wells, R.G. (2003), *Blade Forced Response Prediction for Industrial Gas Turbines, Part 2: Verification and Application*, ASME GT2003-38642, 2003.

[52] Campbell, W. (1924), *The Protection of Steam Turbine Wheels from Axial Vibration*, Proceedings of the Cleveland Spring Meeting, ASME, May 1924.

[53] Bishop, R.E.D. and Johnson, D.C. (1960), *Mechanics of Vibration*, Cambridge University Press, 1960.

[54] Ballhouse, W.F. and Goorjan, P.M. (1978), *Computation of Unsteady Transonic Flows by the Indical Method*, AIAA Journal Vol. 16, No. 2, pp. 117, 1978.

[55] Guyan, R.J. (1965), *Reduction of Stiffness and Mass Matrices*, AIAA Journal, Vol. 3, No. 2, pp. 380, 1965.

[56] Chiang, H-W.D. and Kielb, R.E. (1992), *An Analysis System for Blade Forced Response*, ASME Paper, 92-GT-172, 1992.

[57] Manwaring, S.R. and Kirkeng, K.L. (1997), *Forced Response Vibrations of a Low Pressure Turbine Due to Circumferential Temperature Distirtions*, 8th ISUAAAT Symposium, Stockholm, 1997.

[58] Schmitt, S., Nurnberger, D. and Carstens, V. (2003), *Evaluation of the Principle of Aerodynamic Superposition in Forced Response Calculations*, 10th International Symposium on Unsteady Aerodynamics and Aeroelasticity of Turbomachines Symposium, Duke University, Durham, NC, USA, Sept 7-11 2003.

[59] Green, J.S. and Marshall, J.G. (1999), {it Forced Response Prediction Within The Design Process, 3rd European Conference on Turbomachinery, London, March 1999.

[60] Filsinger, D., Szwedowicz, J., and Schafer, O. (2001), *Approach to Unidirectional Coupled CFD-FEM Analysis of Axial Turbocharger Turbine Blades*, ASME Paper 2001-GT-288, 2001.

[61] Tran, D.-M., Liauzun, C. and Labaste, C. (2003), *Methods of Fluid-Structure Coupling in Frequency and Time Domains using Linearised Aerodynamics for Turbomachinery*, Journal of Fluids and Structures, Vol. 17, pp.1161-1180, 2003.

[62] Gerolymos, G.A. (1993), *Coupled Three-Dimensional Aeroelastic Stability of Bladed Disks*, Journal of Turbomachinery, Vol. 115, pp.791-799, Oct. 1993.

[63] Ewins, D. J. (1969), *The Effects of Detuning Upon the Forced Vibrations of Bladed Disks*, Journal of Sound and Vibration, Vol. 9, No. 1, pp. 65-79, 1969.

[64] Griffin, J. H. and Hoosac, T. M. (1984), *Model Development and Statistical Investigation of Turbine Blade Mistuning*, ASME Journal of Vibration, Acoustics, Stress, and Reliability in Design, Vol. 106, pp. 204-210, 1984.

[65] Wei, S.T. and Pierre, C. (1988), *Localization Phenomena in Mistuned Assemblies with Cyclic Symmetry, Part II: Forced Vibrations*, ASME Journal of Vibration, Acoustics, Stress and Reliability in Design, Vol. 110, No.4, pp. 439-449, 1988.

[66] Craig, R.R., and Bampton, M.C.C. (1968), *Coupling of Substructures for Dynamics Analysis*, AIAA Journal, Vol. 6, pp. 1313-1319, 1968.

[67] Irretier, H. (1983), *Spectral Analysis of Mistuned Bladed Disk Assemblies by Component Mode Synthesis in Vibrations of Bladed Disk Assemblies*, Proceedings of the ASME 9th Biennial Conference on Mechanical Vibration and Noise, Dearborn, Michigan, pp. 115-125, 1983.

[68] Zheng, Z.-c. and Wang, F.-R. (1985), *Dynamic Analysis of Blade Groups Using Component Mode Synthesis in Vibrations of Blades and Bladed Disk Assemblies*, Proceedings of the ASME 10th Biennial Conference on Mechanical Vibration and Noise, Cincinnati, Ohio, pp. 97-103, 1985.

[69] Castanier, M. P., Ottarsson, G., and Pierre, C. (1997), *A Reduced-Order Modeling Technique for Mistuned Bladed Disks*, ASME Journal of Vibration and Acoustics, Vol. 119, No. 3, pp. 439-447, 1997.

[70] Yang, M.-T. and Griffin, J. H. (1997), *A Reduced Order Approach for the Vibration of Mistuned Bladed Disk Assemblies*, ASME Journal of Engineering for Gas Turbines and Power, Vol. 119, pp. 161-167, 1997.

[71] Bladh, R., Castanier, M.P. and Pierre, C. (2001), *Reduced Order Modelling Techniques for Dynamic Analsis of Mistuned Multi-Stage Turbomachinery Rotors*, ASME Paper, 2001-GT-0276, 2001.

[72] Moyroud, F., Fransson, T.H. and Jacquet-Richardet, G. (2002), *A Comparison of Two Finite Element Reduction Techniques for Mistuned Bladed Disks*, Journal of Engineering for Gas Turbines and Power, Vol. 124, No. 4, pp. 942-952, 2002; also ASME Paper 2000-GT-0362, 2000.

[73] Myhre, M., Moyroud, F. and Fransson, T.H. (2003), *Numerical Investigation of the Sensitivity of Forced Response Characteristics of Bladed Disks to Mistuning*, ASME Paper GT-2003-38007, 2003.

[74] Li, H-D. and He, L. (2002), *Single Passage Analysis of Unsteady Flows Around Vibrating Blades of a Transonic Fan Under Inlet Distortion*, ASME Journal of Turbomachinery, Vol. 124, pp. 285-292, 2002; also ASME Paper 2001-GT-272, 2001.

[75] Schmitt, S., Nrnberger, D. and Carstens, V. (2003), *Evaluation of the Principle of Aerodynamic Superposition in Forced Response Calculations*, 10th International Symposium on Unsteady Aerodynamics and Aeroelasticity of Turbomachines Symposium, Duke University, Durham, NC, USA, Sept 7-11, 2003.

[76] Theodorsen, T. and Garrick, I.E. (1940), *Mechanism of Flutter: A Theoretical and Experimental Investigation of the Flutter Problem*, NACA Report 685, 1940.

[77] Goland, M. (1945), *The Flutter of a Uniform Cantelever Wing*, Journal of Applied Mechanics, Vol. 12, No. 4, December 1945.

[78] Lane, F. (1957), *Supersonic Flow Past an Oscillating Cascade with Supersonic Leading Edge Locus*, Journal of the Aeronautical Sciences, Vol. 24, No. 1, pp. 54-66, 1957.

[79] Carta, F. O. (1967), *Coupled Blade-Disc-Shroud Flutter Instabilities in Turbojet Engine Rotors*, Journal of Engineering for Power, Vol. 89, No. 3, 1967, pp. 419-426.

[80] Theodorsen, T. (1935), *General Theory of Aerodynamic Instability and the Mechanism of Flutter*, NACA Report 496, 1935.

[81] Mikolajczak, A.A., Arnoldi, R.A., Snyder, L.E. and Stargardter, H. (1975), *Advances in Fan and Compressor blade Flutter Analysis and Predictions*, Journal of Aircraft, Vol. 12, No. 4, pp. 325-332, April, 1975.

[82] Bendiksen, O. and Friedmann, P. (1982), *The Effect of Bending and Torsion Coupling on Fan and Compressor Blade Flutter*, ASME Journal of Engineering for Gas Turbines and Power, Vol. 104, pp. 617-623.

[83] Kaza, K.R.V. and Kielb, R.,E. (1982), *Flutter and Response of a Mistuned Cascade in Incompressible Flow*, AIAA Journal, Vol. 20, pp. 1120-1127, 1982.

[84] Kielb, R.E. and Ramsey, J.K. (1989), *Flutter of a Fan Blade in Supersonic Axial Flow*, ASME Journal of Turbomachinery, Vol. 111, pp. 462-467, 1989.

[85] Verdon, J.M. and Caspar, J.R. (1982), *Development of a linear Unsteady Aerodynamic Analysis for Finite-Deflection Subsonic Cascades*, AIAA Journal, Vol. 20, No. 9, pp. 1259-1267, 1982.

[86] Whitehead, D.S. (1990), *A Finite Element Solution of Unsteady Two-Dimensional Flow in Cascades*, International Journal for Numerical Methods in Fluids, Vol. 10, No. 1, pp.13-34, 1990.

[87] Hall, K.C. (1993), *Deforming Grid Variational Principle for Unsteady Small Disturbance Flows in Cascades*, AIAA Journal, Vol. 31, No. 5, pp. 540-550, 1993.

[88] Takahara, S., Adachi, T. and Kadiya, Y. (1980), *On the Numerical Analysis of Stall Flutter in Turbine Cascades*, Proceedings of the 2nd International Symposium on Aeroelasticity in Turbomachines, 1980.

[89] Giles, M. and Haimes, R. (1991), *Validation of a Numerical Method for Unsteady Flow Calculations*, ASME Paper 91-GT-271, 1991.

[90] Siden, L.D.G. (1991), *Numerical Simulation of Unsteady Viscous Compressible Flows Applied to a Blade Flutter Analysis*, ASME Paper 91-GT-203, 1991.

[91] He, L. and Ning, W. (1998), *Efficient Approach for Analysis of Unsteady Viscous Flows in Turbomachines*, AIAA Journal, Vol. 36, pp. 2005-2012, 1998.

[92] Clark, W.S. and Hall, K.C. (1999), *A Time-Linearized Navier-Stokes Analysis of Stall Flutter*, Presented at the International Gas Turbine and Aeroengine Congress and Exhibition, Indianapolis, Indiana, June 7-10, 1999.

[93] Chassaing, J.-C. and Gerolymos, G.A. (2000), Compressor Flutter Analysis using Time-nonlinear and Time-linearized 3-D Navier-Stokes Methods, The 9th International Symposium on Unsteady Aerodynamics and Aeroelasticity of Turbomachines, September 4-8 2000, Editors Ferrand, P. and Aubert, S., Published by Presses Universitaires de Grenoble, 2000.

[94] Goldstein, M.E. and Atassi, H. (1976), *A Complete Second-Order Theory for the Unsteady Flow About an Airfoil Due to a Periodic Gust*, Journal of Fluid Mechanics, Vol. 74, No. 4, pp. 741-765, 1976.

[95] Manwaring, S.R. and Fleeter, S., (1990), *Inlet distortion generated periodic aerodynamic rotor response*, ASME Journal of Turbomachinery, Vol.112, 298-307.

[96] Mugridge, B.D. and Morfey, C.L. (1972), *Sources of Noise in Axial Flow Fans*, Journal of the Acoustical Society of America, Vol. 51, No. 5, Part 1, pp. 1411-1426, 1972.

[97] Raj, R. and Lakshminarayana, B. (1973), *Characteristics of the Wake Behind a Cascade of Airfoils*, Journal of Fluid Mechanics, Vol. 61, Pt. 4, pp. 707-730, 1973.

[98] Kielb, R.E. (1999), *Forced Response Analysis - 2*, Aeroelasticity in Axial Flow Turbomachines, Lecture Series 1999-05, von Karmen Institute for Fluid Dynamics, May 3-7, 1999.

[99] Campobasso, M.S. and Giles, M.B. (2000), *Flutter and Forced Response of Mistuned Turbomachinery*, Report NA-00/20, Oxford University Computing Laboratory, 2000.

[100] Moyroud, N., Cosme, N., Jker, M., Fransson, T.H., Lornage, D. and Jacquet-Richardet, G., 2000, *A Fluid-Structure Interfacing Technique for Computational Aeroelastic Simulations*, The 9th International Symposium, September 4-8, 2000, Editors Ferrand, P. and Aubert, S., Published by Presses Universitaires de Grenoble.

[101] Bréard, C., Green, J.S., Vahdati, M. and Imregun, M., (2000), *A Resonance Tracking Algoritm for the Prediction of Turbine Forced Response with Friction Dampers*, ASME Paper 2000-GT-0372, 2000.

[102] Adamczyk, J.J., Stevans, W. and Jutras, R. (1982), *Supersonic Stall Flutter of High Speed Fans*, ASME Journal of Engineering for Power, Vol. 104, 1982, pp. 675-682. Equations, ASME Paper 92-GT-136, 1992.

[103] Bendiksen, O. and Friedmann, P. (1979), *Coupled Bending-Torsion Flutter in Cascades*, AIAA Journal, Vol. 18, No. 2, pp. 194-201, 1979.

[104] Steger, J. and Benek, J. (1987), *On the Use of Composite Grid Schemes in Computational Aerodynamics*, Computational Methods in Applied Mechanics and Engineering, Vol.64, No. 1-3, 1987.

[105] Rai, M. (1987), *Unsteady 3D Navier-Stokes Simulations of Turbine Rotor-Stator Interaction*, AIAA Paper 87-2038, 1987.

[106] Sisto, F., Thangam, S. and Abdel-Rahim, A., (1991), *Computational Prediction of Stall Flutter in Cascaded Airfoils*, AIAA Journal, Vol. 29, pp. 1161-1167.

[107] Abdel-Rahim, A., Sisto, F. and thangam, F., (1993), *Computational Study of Stall Flutter in Cascaed Airfoils*, Journal of Turbomachinery, Vol. 115, pp. 157-166.

[108] Bakhle, M.A., Reddy, T.S.R. and Keith, T.G., (1992), *Time Domain Flutter Analyis of Cascades Using a Full-potential Solver*, AIAA Journal, Vol. 30, npp.163-170.

[109] He, L., (1992), *Integration of 2-D Fluid/Structure Coupled System for Calculations of Turbomachinery Aerodynamic/Aerlelastic Instabilities*, Computational Fluid Dynamics, 1994, Vol. 3., pp. 217-231.

[110] Vahdati, M. and Imregun, M., (1994), *Non-linear Aeroelastic Analyses Using Unstructured Dynamic Meshes*, Proceedings of the 7th International Symposium on Unsteady Aerodynamics and Aeroelasticity of Turbomachines, Fukuoka.

[111] Chew, J.W., Marshall, J.G., Vahdati, M. and Imregun, M., (1997), *Part-speed Flutter Analysis of Wide-chord Fan Blade*, Proceedings of the 8th International

Symposium on Unsteady Aerodynamics and Aeroelasticity of Turbomachines, Stockholm, Sweden, 1997.

[112] Hwang, C.J. and Fang, J.M., (1999), Flutter Analysis of Cascades Using an Euler/Navier-Stokes Solution-Adaptive Approach, Journal of Propulsion and Power, Vol. 15, pp. 54-63.

[113] Bendiksen, O.O., (1991), *A New Approach to Computational Aeroelasticity*, AIAA Paper 91-0939, 31st Structural Dynamics and Materials Conference, Baltimore, USA, 1991, pp. 1712-1727.

[114] Sayama, A.I., Vahdati, M. and Imregun, M., (2000), *An Integrated Nonlinear Approach for Turbomachinery Forced Response Prediction. Part I: Formulation*, Journal of Fluids and Structures (2000), Vol. 14, pp. 87-101.

[115] Vahdati, M., Sayama, A.I. and Imregun, M., (2000), *An Integrated Nonlinear Approach for Turbomachinery Forced Response Prediction. Part II: Case Studies*, Journal of Fluids and Structures (2000), Vol. 14, pp. 103-125.

[116] den Hartog, J.P., (1931), *Forced Vibrations with Combined Coulomb and Viscous Damping*, Transactions of the ASME, Vol 53, pp. 107-115, 1931.

[117] Caughey, T.K. and Griffin, J.H., (1960), *Sinusoidal Excitation of a System with Bilinear Hysteresis*, Transactions of the ASME, Journal of Applie Mechanics, Vol 27, pp.640-643, 1960.

[118] Menq, C.-H. and Griffin, J.H., (1985), *A Comparison of Transient and Steady-State Finite Element Analyses of the Forced Response of a Frictionally Damped Beam*, Journal of Vibration, Acoustics, Stress and Reliability in Design, Vol. 107, pp.19-25, 1985.

[119] Muszynska, A. and Jones, D.I.G, (1983), *On Tuned Bladed Disc Dynamics: Some Aspects of Friction Related Mistuning*, Journal of Sound and Vibration, Vol 86(1), pp. 107-128, 1983.

[120] Menq, C.-H. and Bielak, J., (1986), *The Influence of a Variable Normal Load on the Forced Vibration of a Frictionally Damped Structure*, ASME Journal of Engineering for Gas Turbines and Power, Vol. 108, April 1986, pp. 300305.

[121] Griffin, J.H., (1980), *Friction Damping of Resonant Streses in Gas Turbine Engine Aerofoils*, ASME Journal of Engineering for Power, Vol. 102, pp. 329-333, 1980.

[122] Mindilin, R. D., (1949) *Compliance of Elastic Bodies in Contact*, Journal of Applied Mechanics, Vol. 16, pp. 259-268, 1949.

[123] Courtney-Pratt, J.S. and Eisner, E., (1957), *The Effect of a Tangential Force on the Contact of Metallic Bodies*, Proceedings of the Royal Society: Series A, Vol 238, pp. 529-550, 1957.

[124] Greenwood, J.A. and Williamson, J.B.P., (1966), *Contact of Nominally Flat Surfaces*, Proceedings of the Royal Society: Series A, Vol 295, pp. 300-319, 1966.

[125] Greenwood, J.A. and Tripp, J.H., (1971), *The Contact of Two Nominally Flat Rough Surfaces*, Proceedings of the Institution of Mechanical Engineers, Vol. 185, pp. 625-633, 1971.

[126] Burdekin, M., Cowley and Back, N., (1978), *An Elastic Mechanism for the Micro-Sliding Characteristics Between Contacting Machined Surfaces*, IMechE Journal of Mechanical Engineering Science, Vol. 20, No. 3, pp. 121-127, 1978.

[127] Chang, R.W., Etsion, I. and Bogy, D.B., (1987), *An Elastic-Plastic Model for the Contact of Rough Surfaces*, ASME Journal of Tribology, Vol. 109, pp. 257-263, 1987.

[128] Chang, R.W., Etsion, I. and Bogy, D.B., (1988), *Static Friction Coefficient Model for Metallic Rough Surfaces*, ASME Journal of Tribology, Vol. 110, pp. 57-63, 1988/

[129] Björklund, S., (1997), *A Random Model for Micro-Slip Between Nominally Flat Surfaces*, Transactions of the ASME, Vol. 119, pp. 726-732, October 1997.

[130] Olofsson, U,. (1995), *Cyclic Microslip Under Unlubricated Conditions*, Tribology International, Vol. 28, No. 4, pp. 207-217, 1995.

[131] Hagman, L., (1993), *Micro-slip and Surface Deformation*, Licentiate Thesis, Royal Institute of Technology, Stockholm, Sweden, 1993, TRITA-MAE 1993:5.

[132] Hagman, L. and Olofsson, U., (1998), *A Model for Mocro-slip Between Flat Surfaces Based on Deformation of Ellipsoidal Elastic Asperities–Parametric Study and Experimental Investigation*, Tribology International, Vol. 31, No. 4, pp. 209-217, 1988.

[133] Sanliturk, K.Y. and Ewins, D.J., (1996), *Modelling Two-Dimensional Friction Contact and its Application using Harmonic Balance Method*, Journal of Sound and Vibration, Vol. 193, No. 2, pp. 511-523, 1996.

[134] Menq, C.-H., Chidamparam, P. and Griffin, J.H., (1991), *Friction Damping of Two-Dimensional Motion and its Application in Vibration Control*, Journal of Sound and Vibration, Vol. 144, pp. 427-447, 1991.

[135] Petrov, E.P. and Ewins, D.J., (2003), *Generic Friction Models for the Time-Domain Analysis of Bladed Disks*, ASME Paper GT-2003-38475, 2003.

[136] Csaba, G., (1998), Modelling Microslip Friction Damping and its Influence on Turbine Blade Vibrations,Dissertation No. 519, Division of Machine Design, Dept. of Mechanical Engineering, Linköping University, Sweden, 1998.

[137] Griffin, J.H, 1990), *A Review of Friction Damping of Turbine Blade Vibration*, International Journal of Turbo and Jet Engines, Vol. 7, pp. 297-307, 1990.

[138] Csaba, G., (1998), *Forced Response Analysis in Time and Frequency Domains of a Tuned Bladed Disk with Friction Dampers*, Journal of Sound and Vibration, Vol. 214, No. 3, pp. 395-412, 1998.

[139] Sanliturk, K.Y., Ewins, D.J. and Stanbridge, A.B., (1999), *Underplatform dampers for turbine blades: Theoretical Modelling, Analysis and Comparison with Experimental Data*, ASME Paper 99-GT-335.

[140] Panning, L., Sextro, W. and Popp, K., (2002), *Optimisation of the Contact Geometry Between Turbine Blades and Underplatform Dampers with Respect to Friction Damping*, ASME Paper GT-2002-30429.

[141] Baldwin, B.S. and Lomax, H., (1978), *Thin Layer Approximation and Algebraig Model for Seperated Turbulent Flows*, AIAA Paper 78-257.

[142] Giles, M.B., (1990), *Nonreflecting Boundary Conditions for the Euler Equations*, AIAA Journal, Vol. 28, No. 12, pp. 2050-2058.

[143] Saxer, A.P. and Giles, M.B., (1993), *Quasi-Three-Dimensional Nonreflecting Boundry Conditions for Euler Equation Calculations*, AIAA Journal of Propulsion and Power, Vol. 9, No. 2, pp. 263-271.

[144] Denton, J.D., (1992), *The Calculation of Three-Dimensional Viscous Flow Through Multistage Turbomachines*, ASME Journal of Turbomachinery, Vol. 114, No. 1, pp. 18-26.

[145] Namba, M., and Ishikawa, A., (1983), *Three-dimensional Aerodynamic Characteristics of Oscillating Supersonic and Transonic Annular Cascades*, ASME Journal of Engineering for Power, Vol. 105, pp. 138-146.

[146] He, L., Chen, T., Wells, R.G., Li,Y.S., and Ning, W., (2002), *Analysis of Rotor-Rotor and Stator-Stator Interferences in Multi-Stage Turbomachines*, ASME Paper GT-2002-30355.

[147] Srivastava, R., Bakhle, T.G., Keith, T.G., Jr., (2002), *Flutter Analysis of a Transonic Fan*, ASME Paper GT-2002-30319.

[148] Li, Y. S. and Wells, R. G.,(1999), *The Three-Dimensional Aerodynamic Design and Test of a Three-Stage Transonic Compressor*, ASME 99-GT-068.

[149] Liu, B.-L., (1994) *High Frequency Flow / Structure Interaction in Dense Subsonic Fluids*, Nasa Contractor Report, SuDoc NAS 1.26:194007 / NAS8-38187, Rockwell

[150] Sellgren, U. and Olofsson, U., (1999), *Application of Constitutive Model for Micro Slip in Finite Element Analysis*, Computer Methods in Applied Mechanics and Engineering, Vol. 70, pp. 65-77.